

---

# The Role of Neutrinos in Explosive Nucleosynthesis in Core Collapse Supernova Models with Neutrino Transport

---

**Inauguraldissertation**

zur

Erlangung der Würde eines Doktors der Philosophie  
vorgelegt der  
Philosophisch-Naturwissenschaftlichen Fakultät  
der Universität Basel

von

**Carla Fröhlich**

von Raperswilen TG, Schweiz



Basel, 2009

Genehmigt von der Philosophisch-Naturwissenschaftlichen Fakultät auf Antrag von:

Prof. Dr. F.-K. Thielemann  
Prof. Dr. K. Langanke  
(Mitglieder des Dissertationskomitees)

Basel, den 24 April 2007

Prof. Dr. H.-P. Hauri  
(Dekan)

---

## Abstract

The problem of core collapse supernova explosions is long standing and attempts to understand the mechanism have been ongoing. On one hand, a full understanding of the underlying mechanism is still pending. On the other hand, there is a need to provide correct nucleosynthesis abundances for the progressing fields of galactic evolution and observations of low-metallicity stars. Traditionally, nucleosynthesis predictions rely on artificially induced explosions which is justifiable for the outer stellar layers but does not account for the effects in the innermost ejecta directly related to the explosion mechanism. The composition of the innermost ejecta is directly linked to the electron fraction  $Y_e = \langle Z/A \rangle$ .

This dissertation contains the first investigation of explosive core collapse nucleosynthesis which consistently includes all weak interactions responsible for changes in  $Y_e$  (neutrino/antineutrino captures on free nucleons and on nuclei, electron/positron captures, and  $\beta^-/\beta^+$ -decays). A second novelty of the nucleosynthesis calculations in this thesis is that they are based on core collapse models where the mass cut emerges consistently from the simulation. This is of importance for predicting the amount of Fe-group elements ejected (this is a free parameter in explosions induced by means of a thermal bomb or piston and has to be constrained from observations).

Two different approaches are used to achieve explosions (in otherwise non-explosive models): We apply parametrized variations to the neutrino absorption cross sections in order to mimic in one dimension the possible increase of neutrino luminosities caused by uncertainties in proto-neutron star convection in a multi-D scenario. Alternatively, we apply parametrized variations to the neutrino absorption cross section on nucleons in the gain region to mimic the increased neutrino energy deposition which convective turnover of matter in the gain region is expected to provide. We find that both measures lead to explosions and that  $Y_e > 0.5$  in the innermost ejected layers (i.e. a proton-rich environment).

The nucleosynthesis calculations show that

- The proton-rich environment results in enhanced abundances of  $^{45}\text{Sc}$ ,  $^{49}\text{Ti}$ , and  $^{64}\text{Zn}$  as required by chemical evolution studies and observations of low-metallicity stars.
- Antineutrino absorption reactions in the proton-rich environment produce neutrons which are immediately captured by neutron-deficient nuclei.
- A new nucleosynthesis process ( $\nu p$ -process) takes places in supernovae (and possibly gamma-ray bursts) allowing for appreciable synthesis of elements with mass numbers  $A > 64$ .
- The  $\nu p$ -process is a candidate for explaining the large Sr abundance seen in a hyper-metal poor star, for the suggested *lighter element primary process*, and possibly for the origin of the solar abundances of the light  $p$ -nuclei.



---

# Table of Contents

<b>Abstract</b>	<b>iii</b>
<b>List of Figures</b>	<b>iii</b>
<b>List of Tables</b>	<b>v</b>
<b>Chapter 1: Introduction</b>	<b>1</b>
1.1 Core Collapse Supernovae . . . . .	1
1.1.1 Observations . . . . .	1
1.1.2 The Mechanism . . . . .	2
1.1.3 Modeling: Status and Challenges . . . . .	3
1.2 Nucleosynthesis . . . . .	4
1.2.1 Nucleosynthesis in Core Collapse Supernovae . . . . .	4
1.2.2 The Relevance of Nucleosynthesis Yields from Supernovae . . . . .	5
1.3 This Work . . . . .	5
<b>Chapter 2: Thermonuclear Reactions and Nuclear Reaction Networks</b>	<b>7</b>
2.1 Thermonuclear Reaction Rates . . . . .	7
2.2 Reactions with Leptons . . . . .	9
2.2.1 Electron and Positron Captures . . . . .	9
2.2.2 Neutrino and Antineutrino Capture Reactions . . . . .	10
2.3 Nuclear Reaction Networks . . . . .	10
2.3.1 Derivation . . . . .	10
2.3.2 Energy Generation . . . . .	11
2.3.3 Solving the Thermonuclear Reaction Network . . . . .	11
2.4 Nuclear Statistical Equilibrium . . . . .	12
<b>Chapter 3: Inputs and Explosion Models</b>	<b>15</b>
3.1 Inputs . . . . .	15
3.1.1 Reaction Rates . . . . .	15
3.1.2 Neutrino-Induced Reactions . . . . .	16
3.1.3 Progenitors . . . . .	20
3.1.4 The Equation of State . . . . .	20
3.2 Core Collapse Supernova Models with Neutrino Transport . . . . .	22
3.2.1 Hydrodynamics . . . . .	22
3.2.2 Matter in a Neutrino Field . . . . .	23
3.2.3 The Electron Fraction . . . . .	26

<b>Chapter 4:</b>	<b>Nucleosynthesis</b>	<b>29</b>
4.1	Introduction . . . . .	29
4.2	The Innermost Ejecta . . . . .	29
4.2.1	The Effect of Neutrinos . . . . .	30
4.2.2	Comparison of Model A40 and B07 . . . . .	32
4.3	Iron Group Nucleosynthesis . . . . .	32
4.4	The $\nu p$ -Process . . . . .	37
4.4.1	Open Questions . . . . .	37
4.4.2	Intermezzo: Neutrino-Induced Nucleosynthesis . . . . .	38
4.4.3	The Mechanism . . . . .	38
4.4.4	Sensitivity . . . . .	39
4.4.5	Conclusions . . . . .	40
4.5	The Reaction Flow . . . . .	42
4.6	A 20 $M_{\odot}$ Model at Solar Metallicity . . . . .	42
<b>Chapter 5:</b>	<b>The Bigger Picture: Supernovae and Galactic Chemical Evolution</b>	<b>55</b>
5.1	Stellar Evolution and Explosive End Stages . . . . .	55
5.2	Predicted Yields and Observations . . . . .	56
5.3	Concluding Outlook . . . . .	60
<b>Chapter 6:</b>	<b>Summary and Outlook</b>	<b>61</b>
	<b>Bibliography</b>	<b>63</b>
	<b>Acknowledgments</b>	<b>71</b>
	<b>Curriculum Vitae</b>	<b>73</b>
	<b>List of Publications</b>	<b>75</b>

---

## List of Figures

3.1	Trajectories, energy scales, electron fraction, and abundances for models of series A and B.	24
4.1	Time evolution of the neutrino luminosities and average temperatures, of the electron fraction, and of its time derivative including individual contributions . . . . .	31
4.2	Evolution after core bounce for a representative ejected layer of model A40 . . . . .	33
4.3	Comparison of abundances with and without neutrino-induced reactions for model A40 at $Y_e > 0.5$ . . . . .	34
4.4	Comparison of abundances with and without neutrino-induced reactions for model B07 at $Y_e > 0.5$ . . . . .	34
4.5	Combined abundances of this work and TNH96 . . . . .	36
4.6	Elemental abundances for Ca to Zn compared to observational data of metal poor stars	36
4.7	Evolution of the abundances of n, p, $\alpha$ , and $^{56}\text{Ni}$ in a trajectory from model B07 . . . .	39
4.8	Reaction rates for different reaction on $^{64}\text{Ge}$ . . . . .	40
4.9	Abundances of the light $p$ -nuclei as function of $Y_e$ . . . . .	41
4.10	Time slices of abundances during the $\nu p$ -process (part I) . . . . .	43
4.11	Time slices of abundances during the $\nu p$ -process (part II) . . . . .	44
4.12	Maximum temperatures and densities in the ejecta . . . . .	45
4.13	Regimes of Si burning in the peak temperature and density plane . . . . .	46
4.14	Mass fractions for the major nuclei from explosive nucleosynthesis . . . . .	46
4.15	Mass fractions for the major nuclei <i>before</i> shock passage . . . . .	47
4.16	Electron abundances $Y_e$ as function of radial mass . . . . .	48
4.17	Final electron fraction $Y_e$ as function of radial mass . . . . .	48
4.18	Initial abundance distribution in the $N$ - $Z$ -plane for the most proton-rich mass zone . . .	49
4.19	Abundance distribution in the $N$ - $Z$ -plane for the most proton-rich mass zone . . . . .	50
4.20	Abundance distribution in the $N$ - $Z$ -plane for the most proton-rich mass zone . . . . .	51
4.21	Abundance distribution in the $N$ - $Z$ -plane for the most proton-rich mass zone . . . . .	52
4.22	Isotopic abundances from the explosive processing of the He-core of a $20M_\odot$ star . . . .	53
4.23	Elemental overabundances for the He-core of a $20M_\odot$ star. . . . .	54
5.1	C-O core masses and explosion energies as function of the initial stellar mass . . . . .	56
5.2	Abundance ratios for various elements as a function of metallicity . . . . .	58





---

## List of Tables

3.1	Nuclei for which electron and positron captures by FFN and LMP are included. . . . .	16
3.2	Nuclei on which neutrino/antineutrino captures by ZL are included. . . . .	18
3.3	Values for $T_\nu$ and $\alpha$ in the Fermi-Dirac spectrum for neutrinos. . . . .	19
3.4	Fe-core masses for progenitor models by Umeda <i>et al.</i> [144] . . . . .	20
3.5	Name and properties of the discussed runs of series A and B. . . . .	23
4.1	List of nuclei in the reaction network . . . . .	30



# 1

---

## Introduction

Supernovae are one of nature’s most spectacular and energetic events. During such an event a single star can briefly outshine its entire host galaxy. It may even be visible in neighboring galaxies by the naked eye or with simple telescopes. The energy output of a core collapse supernova is enormous: During the collapse and explosion about  $10^{53}$  erg ( $1 \text{ erg} = 10^{-7} \text{ J}$ ) of gravitational energy are released and mainly carried away by neutrinos. The kinetic energy of a supernova is  $\sim 10^{51}$  erg. The supernova light curve is powered by radioactive decays, predominantly by the decays  $^{56}\text{Ni} \rightarrow ^{56}\text{Co}$  and subsequently  $^{56}\text{Co} \rightarrow ^{56}\text{Fe}$ . These powerful explosions synthesize most of the elements in nature and they are at the origin of dense astrophysical objects like neutron stars or black holes.

From observations, in particular from supernova spectra, two types of supernovae (with possible subclasses are distinguished. If the star explodes while the H-envelope is still present (i.e. the spectrum shows H-lines) the supernova is classified as type II supernova. Type I supernovae do not exhibit hydrogen lines in their spectra (these are explosions of stars that have lost their H-envelope prior to explosion). Prominent Si-features in the supernova spectrum (combined with a lack of H-lines) define the subclass of type Ia supernovae. The absence of both H- and Si-lines is characteristic for type Ib supernovae (He-lines must be present in the spectrum) or type Ic supernovae (no He-lines in the spectrum) (for a recent summary see e.g. [61]). This classification is purely spectroscopic and does not reveal the underlying physics of the explosion mechanism. Type Ia SNe are the only type of supernovae observed in elliptical galaxies (with no or negligible star formation) and therefore have to originate from an older (revived) stellar population. Their origin is explained via exploding carbon-oxygen white dwarfs in binary stellar systems after accreting sufficient matter from the companion star to undergo a thermonuclear runaway (for details see e.g. [67]). All other types of supernovae (type Ib, Ic, and II) only occur in star forming regions, i.e. regions with young massive stars, and are believed to proceed via core collapse of massive stars (possibly in binary systems).

The light curves of type Ia supernovae are very similar from event to event and can be standardized according to the Phillips relation [114]. This makes SN Ia supernovae candidates for “standard candles” to determine absolute magnitudes and therefore distances. The light curves of type II supernovae show broad variation. The two main subclasses for early-time core collapse light curves are SNe II-L (“linear”) and SNe II-P (“plateau”). The SNe II-P light curve remains close to maximum brightness for an extended period of time, whereas light curves of SNe II-L are similar to those of type I supernovae.

In this thesis we will only be concerned with type II core collapse supernovae. The term supernova will be used equivalently to core collapse supernova and type II supernova.

### 1.1. Core Collapse Supernovae

---

#### 1.1.1 Observations

The earliest recorded observations of supernovae or so called “guest stars” date back to as early as AD 185. Records by Chinese astronomers report several long duration guest stars before AD 1000. Due to the scarcity of the records it is not possible to unambiguously identify the remnants of all of these supernovae. The brightest supernovae ever was discovered on 30 April 1006 in the Arab Dominions

and one day later in China and Japan. It is described as being bright enough to cast shadows on the ground at night, brighter than the quarter moon. It remained visible for three years. More supernovae were observed in AD 1054, AD 1572, and AD 1604. The most famous supernova being the one of AD 1054. Its remnant is the Crab Nebula. The supernova in AD 1572 (Tycho's supernova), located in Cassiopeia, was observed in China and in Europe. The most detailed observations on position and brightness originate from Tycho Brahe, hence the name Tycho's supernova. Another famous supernova was discovered in AD 1604 by Kepler. Though less bright than Tycho's supernova it was still visible for a whole year. For more details on the historic supernovae see [58]. A systematic survey of supernovae was conducted by Baade and Zwicky in the 1930s. Since then innumerable supernovae have been discovered.

The primary object of observation is the light curve. The observed spectrum and its temporal evolution combined with other observations can give hints about the chemical composition of the ejecta, the progenitor, the explosion mechanism, and even the distance of the supernova. In the case of supernova SN1987A in the Large Magellanic Cloud (LMC) – the best observed supernova to date – some neutrinos were detected by two detectors (Kamiokande II in Japan and IMB in Ohio). From the observed neutrino signal several pieces of information could be extracted: for example, an exact time for the start of the explosion (important for normalizing the light curve) and/or the energy released in the collapse. However, the small number of neutrinos recorded (12 for Kamiokande and 8 for IMB) did not allow for much constraint on the explosion mechanism. Secondary objects of observation are the expanding supernova remnant and pulsars (spinning neutron stars with millisecond periods left behind after the explosion). These objects can still be observed many centuries after the original explosion.

### 1.1.2 The Mechanism

Core collapse supernovae stand at the end of the life of stars with main sequence mass above  $\sim 8-10M_{\odot}$ . Such massive stars spend most of their lifetime (timescale of  $10^7$  years) in hydrostatic equilibrium. During this time nuclear fusion reactions (nuclear burning) synthesize elements with increasing charge number, from hydrogen through helium, carbon, oxygen, and silicon, finally reaching iron. The energy release (thermal energy) from these fusion reactions counteracts the gravitational force and allows for a hydrostatic equilibrium in the star. When the nuclear burning fuel at the center is exhausted the thermal pressure decreases and the star experiences gravitational contraction. Due to this gravitational compression the central temperature rises until the temperature reaches a critical value to ignite the next nuclear burning phase. This sequence of nuclear burning until central fuel exhaustion, contraction, and ignition of a next burning phase repeats a number of times depending on the initial mass of the star. At the end of its hydrostatic life the star has an onion like structure where each layer consists of the ashes of a previous burning phases, and of an iron core at the center. This iron core is inert to nuclear burning. This is due to the maximum binding energy per nucleon in iron ( $\sim 8\text{MeV}$  per nucleon) which prevents further energy generation by fusion reactions of iron nuclei. The core grows in mass by silicon shell burning until it exceeds the Chandrasekhar limit and is supported by degenerate electron pressure. The Chandrasekhar mass limit is the maximum mass of a self-gravitating sphere which can be supported by the pressure of a degenerate electron gas;

$$M_{\text{Ch}} \simeq 5.83Y_e^2 M_{\odot}, \quad (1.1)$$

where  $Y_e$  is the electron fraction, i.e. the number of electrons per baryon.

From now on the evolution is dominated by weak interactions. The core starts to contract, increasing the matter density and with it increasing the electron chemical potential,

$$\mu_e \approx 11.1(\rho_{10}Y_e)^{1/3}\text{MeV}, \quad (1.2)$$

where  $\rho_{10}$  is the density in units of  $10^{10} \text{ g/cm}^3$  and  $Y_e$  as above. For typical conditions during silicon shell burning the electron chemical potential is  $\mu_e \approx 2 \text{ MeV}$ . This allows for copious electron capture reactions on Fe-group nuclei, decreasing the electron pressure. At the same time matter becomes more neutron-rich, and therefore  $\beta$ -unstable, and a large number of neutrinos carrying away energy (and entropy) are produced. All of this accelerates the collapse. At densities of  $\rho \approx 10^{12} \text{ g/cm}^3$  the diffusion timescale for neutrinos becomes larger than the collapse time and neutrinos are trapped in the core [12]. The collapse of the inner core proceeds homologous (i.e. the local speed of sound is larger than the

infall velocity which is proportional to the radius) until nuclear matter densities,  $\rho_0 \approx 10^{14}$  g/cm<sup>3</sup>, are reached. Now the homologous core bounces due to the lower compressibility of nuclear matter, driving a shock wave outwards. The outer core — the region of the iron core outside of the homologous core — continues to fall in at supersonic speed.

It is generally accepted that the prompt shock does not lead to an explosion. The shock loses energy by photodisintegrating the heavy nuclei into free nucleons as it passes through. This accelerates the energy loss even further as electron capture cross sections on free nucleons are larger than on heavy nuclei. When the density is low enough for neutrinos to escape (neutrino burst at shock breakout), the neutrinos produced in the electron capture reactions leave the star, carrying away even more energy. All of this weakens the shock so much that it stalls and turns into a standing accretion shock.

In the *delayed neutrino heating mechanism* the shock can be revived by neutrinos from the nascent neutron star at the center. The essential ingredient for a successful explosion is the transfer of gravitational binding energy from the core to the mantle. Neutrinos streaming from the proto neutron star carry most of the energy released during gravitational collapse ( $\sim 10^{53}$  erg). If some of this energy is deposited in the neutrino heating region (region between shock and gain radius) via charged current neutrino and antineutrino reactions on free nucleons,

$$\nu_e + n \rightarrow e^- + p \quad (1.3)$$

$$\bar{\nu}_e + p \rightarrow e^+ + n, \quad (1.4)$$

the shock could be revived. This was first proposed in [13].

### 1.1.3 Modeling: Status and Challenges

Since the 1960s the explosion mechanism has been related to neutrino emission from the hot collapsed core [12, 13, 35]. The pioneering calculations by Colgate & White [34, 35] and by Arnett [5] led to a successful explosions. However, the introduction of previously neglected neutrino scattering processes (e.g. neutrino-electron scattering), which permitted the replacement of lost low energy neutrinos, led to a continuous energy leakage and to the death of the prompt shock within 10 ms after bounce [19, 105]. Ever since, obtaining explosions in spherical symmetry has become less likely despite improvements in the implementation of the neutrino physics [91].

Since then and with the first neutrino detection from a core collapse supernova [SN1987A, see e.g. 24, 82], the hope has been that further improvements would lead to successful explosions via energy deposition through neutrino and antineutrino captures on neutrons and protons (Eqs. (1.3) and (1.4)). Two different paths were explored.

1. Convective instabilities, but with still simplified neutrino transport, causing either (a) convective transport in the core and leading to higher neutrino luminosities [e.g. 79] or (b) higher energy deposition efficiencies in convective regions [51, 62, 77, 95].
2. Improved neutrino transport schemes, leading to higher neutrino luminosities via the full solution of the Boltzmann transport equation for neutrino scattering and neutrino reactions [96, 100, 101].

However, in recent years 1D spherically and 2D rotationally symmetric radiation-hydrodynamic calculations have not yet shown successful supernova explosions with the present knowledge of physical processes [21, 64, 75, 86, 89, 93, 103, 121, 139]. A recent simulation of a 11.2  $M_\odot$  core collapse shows the possibility of successful weak explosions in a multi-D treatment with spectral neutrino transport [74]. This leaves us with two dilemmas. First, the fundamental problem that the supernova mechanism is still not understood. Second, there seems no way to predict the correct supernova nucleosynthesis yields. This is a problem in itself, but is also a limitation for the rapidly expanding field of galactic chemical evolution, which is being energized by the large amount of recent abundance observations from low metallicity stars [e.g. 3, 4, 29, 47, 68, 128].

## 1.2. Nucleosynthesis

The synthesis of elements heavier than helium has been linked to nuclear burning in stars since the independent bench mark papers by Burbidge *et al.* [23] and Cameron [27]. In general, nuclear burning can be classified into two categories according to the timescale involved: (i) hydrostatic burning stages in pre-supernova evolution (slow burning at relatively low densities and temperatures) and (ii) explosive burning (hydrodynamics determines timescale and thermodynamic conditions).

The hydrostatic burning stages are characterized by temperatures allowing (charged) particle with thermal Maxwell-Boltzmann distributions to penetrate increasingly larger Coulomb barriers. H-burning converts protons into  ${}^4\text{He}$  either via the pp-chains or via the CNO cycle. Further burning stages and their major reactions are: He-burning ( ${}^4\text{He}(2\alpha, \gamma) {}^{12}\text{C}$ ), C-burning ( ${}^{12}\text{C}({}^{12}\text{C}, \alpha) {}^{20}\text{Ne}$ ), O-burning ( ${}^{16}\text{O}({}^{16}\text{O}, \alpha) {}^{28}\text{Si}$ ), Ne-burning ( ${}^{20}\text{Ne}(\gamma, \alpha) {}^{16}\text{O}$ ,  ${}^{20}\text{Ne}(\alpha, \gamma) {}^{24}\text{Mg}$ ), and Si-burning (leading to nuclear statistical equilibrium, NSE).

Most of the hydrostatic burning process can occur as well in explosive burning stages at higher temperatures and shorter timescales. The major reactions remain the same, however the beta-decay half-lives are often longer than the timescale for explosive burning. For Si-burning there exist strong differences between the explosive and the hydrostatic version. Explosive Si-burning can be divided into three regimes: (i) incomplete Si-burning, (ii) complete Si-burning with normal freeze-out (high density, low entropy), and (iii) complete Si-burning with alpha-rich freeze-out (low density, high entropy). During a normal freeze-out (i.e at high temperatures) the abundances remain in NSE. The NSE can also break up into smaller clusters where abundances within a cluster are in equilibrium but the clusters are not in equilibrium with each other (quasi equilibrium). This happens for example during an alpha-rich freeze-out, resulting in an enhanced abundance of  ${}^4\text{He}$ . The fuel for explosive nucleosynthesis consists of the ashes of previous burning stages (mainly  $N \approx Z$  nuclei like  ${}^{12}\text{C}$ ,  ${}^{16}\text{O}$ ,  ${}^{20}\text{Ne}$ ,  ${}^{24}\text{Mg}$ ,  ${}^{28}\text{Si}$ ). This results in heavier nuclei, again with  $N \approx Z$ .

### 1.2.1 Nucleosynthesis in Core Collapse Supernovae

Supernova nucleosynthesis predictions have a long tradition [30, 31, 107, 110, 122, 133, 134, 143, 155, 157]. Since the explosion mechanism is still not fully understood self-consistent calculations from first principle are not possible. Instead, a more pragmatic approach is commonly used when the interest is on the nucleosynthesis yields of the event. Core collapse supernova explosions are artificially introduced into the progenitor star model, either via a piston or a thermal bomb [7]. In such an approach, the mass cut between the ejecta and the remnant does not emerge from the simulations, but has to be determined from additional conditions. Lacking self-consistency, the  ${}^{56}\text{Ni}$ -masses ejected from the innermost explosive Si-burning layers cannot be predicted. Nucleosynthesis predictions for the Fe-group from artificially induced explosions has inherent uncertainties: the total amount of iron ejected which is connected to the location of the mass cut, the total energy which influences the synthesis of  ${}^{44}\text{Ti}$  and  ${}^{48}\text{Cr}$ , and finally the electron fraction  $Y_e$  of the ejecta which has an impact on the isotopic ratio of 57/56 in Ni (and also Co and Fe) and also on the overall (elemental) ratio of nickel to iron. While the usage of artificially introduced explosions is justifiable for the outer stellar layers, provided we know the correct explosion energy to be dumped into the shock front (on the order of  $10^{51}$  erg seen in observations), it is incorrect for the innermost ejected layers which should be directly related to the physical processes causing the explosion. This affects the Fe-group composition, discussed in detail in [134], hereinafter TNH96, and [108], which was also recognized as a clear problem in [30] and [142]. The problem is also linked to the so-called neutrino wind, emitted seconds after the supernova explosion, and considered as a possible source of the  $r$ -process to produce the heaviest elements via neutron captures [119, 130, 132, 138, 139, 147, 158].

In this thesis nucleosynthesis calculations are performed which (i) consistently include all weak interactions contributing to changes in the electron fraction and (ii) are based on explosion models where the mass cut emerges from the simulation. This allows to ameliorate two of the above uncertainties for the predicted Fe-group ejecta.

## 1.2.2 The Relevance of Nucleosynthesis Yields from Supernovae

Understanding the mechanism of core collapse supernovae and the resulting nucleosynthesis is an interesting problem in itself. However, the absence of a full and consistent understanding and the lack of correct nucleosynthesis predictions are also a limitation to the field of galactic chemical evolution. Galactic chemical evolution witnesses the enrichment of the interstellar medium with elements heavier than H, He, and Li that originate from the Big Bang. These heavier elements can be traced via the surface composition of low mass stars of different ages which are unaltered since their formation and therefore measure the composition in the interstellar medium at the time of their birth. Thus, the metallicity  $[\text{Fe}/\text{H}]$ <sup>1</sup> is a measure of the enrichment with nucleosynthesis products and indirectly of the ongoing duration of galactic evolution. At very early times, when the interstellar medium is essentially pristine, this interpretation might be wrong and we see the ejecta of individual supernovae where the amount of H with which these ejecta mix is dependent on the explosion energy and the stellar progenitor mass. Recently, a large number of observations of low-metallicity stars has become available [e.g. 3, 4, 29, 47, 68, 128]. These observations have energized the quest to understand the abundances evolution in the interstellar medium. Supernovae are the main contributors to nucleosynthesis in galaxies and therefore play a key role in the process of chemical enrichment of the interstellar medium.

The connection of supernova yields and galactic chemical evolution will be discussed in more detail in Chapter 5. Also, the question will be addressed whether the metallicity affects the way of explosive processing (e.g. by changing the neutron-richness of matter measured by  $Y_e$ ) or influences the stellar evolution and consequently the final nucleosynthesis products.

## 1.3. This Work

The aim of this thesis was to first develop an extension to the Basel nuclear reaction network code by including neutrino-induced reactions, thus creating a unique tool for nucleosynthesis calculations. This reaction network code was then applied to study the explosive nucleosynthesis in core collapse supernovae with the main focus on the role of neutrinos. The motivation to investigate the effects of neutrinos is obvious and manifold. On one hand, the information on the neutrino properties from core collapse simulations is becoming more and more detailed. On the other hand, the correct prediction of Fe-group ejecta has always been a problem since these layers are directly related to the not (yet) fully understood explosion mechanism. The nucleosynthesis for Fe-group elements is directly related to the electron fraction  $Y_e$ . Neutrino-induced reactions contribute to the change in  $Y_e$  and are therefore expected to play an important role in the explosive nucleosynthesis of core collapse supernovae.

The organization of the thesis is as follows. In Chapter 2, thermonuclear reactions are derived and the nuclear reaction networks are described. The appropriate methods to solve such systems is also briefly discussed. This gives the necessary background for the extensions made to the code. In Chapter 3, the new treatment in the network code to accommodate for neutrino-induced reactions (consistent with the hydrodynamical simulation) is explained. Also, the various inputs used for the nucleosynthesis calculations are described. The second part of Chapter 3 is devoted to the hydrodynamical simulations are collapse and bounce. The important features of the codes used are given. Based on this, the conditions of matter around the mass cut is discussed for these models. Chapter 4 contains the nucleosynthesis results of this thesis. First, the high values of  $Y_e$  obtained are discussed. Then the role of neutrinos on the innermost ejecta is examined. The Fe-group ejecta is presented and compared for two different models (different ways to induced the explosion. Also in Chapter 4, a new nucleosynthesis process is presented, the  $\nu p$ -process. The Chapter concludes with a discussion of the explosive nucleosynthesis in a new 20  $M_\odot$  model. In Chapter 5, supernova yields are put into a broader perspective and discussed in the context of galactic chemical evolution. Conclusions and perspectives are given in Chapter 6.

---

<sup>1</sup>  $[\text{Fe}/\text{H}] \equiv \log_{10}(Y_{\text{Fe}}/Y_{\text{H}}) - \log_{10}(Y_{\text{Fe}}/Y_{\text{H}})_\odot$





# 2

## Thermonuclear Reactions and Nuclear Reaction Networks

This Chapter introduces the basic concepts and features of thermonuclear reactions rates and nuclear reaction networks. In terms of notation it follows the (yet) unpublished book by Cowan, Truran & Thielemann [38]. A nuclear reaction network is a system of (a few hundred to a few thousand) coupled 1st-order differential equations with terms for each individual nuclear reaction. It is used to follow the evolution of nuclear abundances in a given astrophysical scenario. The reactions changing the nuclear abundances involve three of the fundamental forces: the strong force (emission and absorption of nucleons and nuclei), the electromagnetic force (emission and absorption of photons), and the weak force (emission and absorption of leptons such as electrons, positrons, neutrinos, and antineutrinos). The general idea is to start with the basic information for a reaction, the nuclear cross section. This information is then used to determine the reaction rate according to the type of reaction under inquiry. Finally, the various reaction rates are gathered into the differential equations for the nuclear reaction network. In this Chapter we will summarize the types of reactions involved and the basic information needed. We will also show how the different nuclear reactions are assembled into the differential equations.

### 2.1. Thermonuclear Reaction Rates

Consider a nuclear reaction between a target  $i$  and a projectile  $j$  with number densities  $n_i$  and  $n_j$ , respectively. The nuclear cross section  $\sigma$  for this reaction is defined as

$$\sigma = \frac{\text{number of reactions per target per second}}{\text{flux of incoming projectiles}}. \quad (2.1)$$

For a constant relative velocity  $v$  between target  $i$  and projectile  $j$  the cross section can be expressed as  $\sigma = (r/n_j)/(n_i v)$  where  $r$  is the number of reactions per  $\text{cm}^3$  per second. In general, when the target and projectile follow a velocity distribution, the number of reactions per  $\text{cm}^3$  per second is given by

$$r_{j;i} = \int \sigma |\vec{v}_j - \vec{v}_i| dn_j dn_i. \quad (2.2)$$

In an astrophysical plasma, the nuclei follow a Maxwell-Boltzmann distribution. The number density for the nuclei  $j$  and  $i$  is then

$$d^3n_j = n_j \left( \frac{m_j}{2\pi kT} \right)^{3/2} \exp \left( -\frac{m_j v_j^2}{2kT} \right) d^3v_j. \quad (2.3)$$

Eq. (2.2) for the thermonuclear reaction rate [33, 45] now simplifies to

$$r_{j,i} = \langle \sigma v \rangle_{j,i} n_j n_i. \quad (2.4)$$

We define

$$\begin{aligned} \langle j, i \rangle &:= \langle \sigma v \rangle_{j,i} \\ &= \left( \frac{8}{\mu\pi} \right)^{1/2} (kT)^{-3/2} \int_0^\infty E \sigma(E) \exp(-E/kT) dE. \end{aligned} \quad (2.5)$$

Equivalently, a mean lifetime of nucleus  $i$  against destruction through particle  $j$  can be defined as:

$$\tau_k(i) \equiv 1/(\langle\sigma v\rangle_{i,j}n_j). \quad (2.6)$$

For reactions in astrophysical plasmas of high temperatures and/or low densities the reacting nuclei are surrounded by a background of electrons and nuclei, and therefore they feel a different Coulomb repulsion than bare nuclei. This effect is referred to as electron screening. The reaction rate integral can be separated into a traditional part, Eq. (2.2), and a factor for screening [71]:

$$\langle j, i \rangle^* = f_{\text{scr}}(Z_j, Z_i, \rho, T, Y_i) \langle j, i \rangle. \quad (2.7)$$

The screening factor  $f_{\text{scr}}(Z_j, Z_i, \rho, T, Y_i)$  depends on the charge of the involved nuclei, the density, temperature, and composition of the plasma.

Knowing the cross section  $\sigma(E)$  allows us to determine the quantity  $\langle\sigma v\rangle$ , provided the assumption that the nuclei follow a Maxwell-Boltzmann distribution is correct. Thermonuclear rates can be obtained from experiments. For example, neutron-induced reactions have large cross sections which even increase with decreasing energy. This allows direct experimental measurements of the nuclear cross section  $\sigma(E)$  at stellar energies. On the other hand, cross sections for charged-particle induced reactions drop rapidly with decreasing energy due to the Coulomb barrier, making it difficult to perform measurements directly at relevant stellar energies. Cross sections for these reactions have to be extrapolated to stellar energies. Whenever experimentally feasible the cross section is determined experimentally. There exist different compilations of experimental rates which are used in astrophysics, see e.g. [28]. For compilations of neutron capture reactions see e.g. [9, 10].

However, not all thermonuclear reaction rates have to be determined experimentally. The cross section of a given reaction is related to the cross section of its inverse reaction. Using the Hauser-Feshbach formalism, Blatt & Weisskopf [14] have derived an expression for the ratio of the two cross sections:

$$\frac{\sigma_i(j, n)_J}{\sigma_o(n, j)_J} = \frac{1 + \delta_{ij} g_n g_o k_n^2}{1 + \delta_{no} g_i g_j k_j^2}, \quad (2.8)$$

where the  $k$  are the wave numbers, the  $g$  are the degeneracy factors of the ground state, and  $\delta_{ij}$  is the Kronecker delta. The quantity  $J$  indicates the state populated in the compound nucleus. The relation in Eq. (2.8) is called *detailed balance*. When summing over all states  $J$  in the compound nucleus a similar relation holds for the total cross section at energy  $E_{i,j}$  and  $E_{n,o}$ , respectively:

$$\frac{\sigma_i(j, n; E_{i,j})}{\sigma_o(n, j; E_{n,o})} = \frac{1 + \delta_{ij} g_n g_o k_n^2}{1 + \delta_{no} g_i g_j k_j^2}. \quad (2.9)$$

For an astrophysical plasma the excited states of a nucleus are thermally populated, i.e.  $g$  has to be replaced by  $G = \sum_l (2J_l + 1) \exp(-E_l/kT)$ . Using the above expression and assuming thermal population of the states in the nuclei, the thermonuclear reaction rate  $\langle\sigma v\rangle_{i,j,n}$  of the reaction  $i(j, n)o$  is related to the thermonuclear rate  $\langle\sigma v\rangle_{o;n,j}$  of the inverse reaction  $o(n, j)i$  through:

$$\langle\sigma v\rangle_{i;j,n} = \frac{1 + \delta_{ij} G_o G_n}{1 + \delta_{no} G_i g_j} \left( \frac{\mu_{no}}{\mu_{ij}} \right)^{3/2} \exp(-Q_{n,j}/kT) \langle\sigma v\rangle_{o;n,j}. \quad (2.10)$$

The symbol  $\mu$  is here used to denote the reduced mass and  $Q_{n,j}$  is the Q-value of the reaction.

### Reactions with Photons

For reactions  $i(\gamma, n)o$  where the projectile is a photon, the relative velocity between target and projectile is the speed of light  $c$ . The distribution  $dn_i$  of the target nucleus  $i$  is a Maxwell-Boltzmann distribution. The photons follow a Planck distribution with temperature  $T$ :

$$d^3n_\gamma = \frac{1}{\pi^2(c\hbar)^3} \frac{E_\gamma^2}{\exp(E_\gamma/kT) - 1} dE_\gamma. \quad (2.11)$$

In this case the quantities in the integral in Eq. (2.2) are thus independent of  $dn_i$  (the photodisintegration cross section depends only on the energy  $E_\gamma$  of the photon). Evaluating the integral in Eq. (2.2) results in

$$r_{i\gamma} = \frac{\int d^3n_i}{\pi^2 c^2 \hbar^3} \int_0^\infty \frac{\sigma_i(\gamma, o; E_\gamma) E_\gamma^2}{\exp(E_\gamma/kT) - 1} dE_\gamma. \quad (2.12)$$

This can be rewritten as

$$r_{i\gamma} = n_i \lambda_{i,\gamma,o}(T) \quad (2.13)$$

where

$$\lambda_{i,\gamma,o}(T) = \frac{1}{\pi^2 c^2 \hbar^3} \int_0^\infty \frac{\sigma_i(\gamma, o; E_\gamma) E_\gamma^2}{\exp(E_\gamma/kT) - 1} dE_\gamma \quad (2.14)$$

acts like a temperature dependent decay constant. If we know the photodisintegration cross section the integral in Eq. (2.14) can be evaluated. However, we do not need to measure the photodisintegration cross sections. They are related to the inverse capture cross sections via detailed balance [45]:

$$\lambda_{i,\gamma}(T) = \left( \frac{G_n G_o}{G_i} \right) \frac{1}{1 + \delta_{no}} \left( \frac{\mu_{no} kT}{2\pi \hbar^2} \right)^{3/2} \langle n, o \rangle \exp(-Q_{no}/kT). \quad (2.15)$$

To derive this relation we have made use of  $k_\gamma = E_\gamma/(\hbar c)$ ,  $g_\gamma = 2$ , and  $E_\gamma = E_{n,o} + Q_{n,o}$  for photons and  $k_n = p/\hbar = \sqrt{2\mu_{no} E_{no}}$ .

### Decays

For decays (like  $\alpha$ - or  $\beta$ -decays) with a half-life  $\tau_{1/2}$  the number of reactions per  $\text{cm}^3$  per second is:

$$r_i = \lambda_i n_i, \quad (2.16)$$

where the quantity  $\lambda = \ln 2/\tau_{1/2}$  is the decay constant. The half-life of the ground state is constant. At higher temperatures the excited states are thermally populated and have individual decay constants  $\lambda_{i,n}$ . The total (temperature dependent) decay constant for nucleus  $i$  then becomes

$$\lambda_i = \frac{\sum_n \lambda_{i,n} (2J_n + 1) \exp(-E_n/kT)}{G_i(T)}, \quad (2.17)$$

where  $G_i = \sum_n (2J_n + 1) \exp(-E_n/kT)$ .

## 2.2. Reactions with Leptons

### 2.2.1 Electron and Positron Captures

For nuclear electron capture reactions,



a similar procedure is applied as for photodisintegrations. Due to the significant mass difference between electron ( $m_e = 0.511 \text{ MeV}/c^2$ ) and nuclei ( $m_A \approx 931 \text{ MeV}/c^2$ ) the nucleus  $i$  is at rest in the center of mass system and the relative velocity between nucleus  $i$  and the electron is due to the velocity of the electron. Again, similar to the case of photodisintegrations, the integral in Eq. (2.2) is independent of the distribution  $dh_i$  of the nuclei  $i$ . This leads to

$$r_{i,e} = n_i \int \sigma_e(v_e) v_e dh_e. \quad (2.19)$$

Using the concept of a temperature (and in this case also density) dependent ‘‘decay constant’’, we can write

$$r_{i,e} = \lambda_{i,e}(\rho Y_e, T) n_i. \quad (2.20)$$

Depending on the density and temperature conditions the electron distribution  $n_{e^-}$  has to be treated as Boltzmann distribution, a partially degenerate, or a fully degenerate Fermi distribution. The same treatment has been extended ([53, 54]) to positron capture reactions,



## 2.2.2 Neutrino and Antineutrino Capture Reactions

Due to the small size of neutrino scattering cross sections neutrino and antineutrino capture reactions occur rarely at low densities. However, at high densities ( $\rho \approx 10^{13}$  g/cm<sup>3</sup>) neutrino scattering reactions off nuclei are able to thermalize a neutrino distribution. Under these condition, the inverse reactions of electron and positron captures become possible:



and



The rate for these reactions can be expressed — in the same way as for electron/positron captures — using a temperature and density dependent “decay constant”  $\lambda_\nu$ :

$$\begin{aligned} r_{i,\nu} &= n_i \int \sigma_\nu(E_\nu) E_\nu dE_\nu \\ &= n_i \lambda_\nu(\rho Y_e, T) \end{aligned} \quad (2.24)$$

The neutrino distribution is a thermal distribution which may, however, be established at a different location than where the reaction is occurring. In this case, it is common practice to describe the neutrino distribution by a chemical potential and a temperature (not necessarily the local temperature!).

The Chapter 3.1.2 contains a detailed discussion on how the neutrino induced reactions are treated in this thesis work. The neutrino temperatures are taken from a core collapse simulation with full Boltzmann neutrino transport allowing for the first time a treatment of the neutrino-induced reactions in the nucleosynthesis consistent with the underlying dynamics of the event.

## 2.3. Nuclear Reaction Networks

### 2.3.1 Derivation

The number of reactions per cm<sup>3</sup> and second governs the change in number density of each species in an astrophysical plasma at constant density:

$$\left( \frac{\partial n_i}{\partial t} \right)_{\rho=\text{const}} = \sum_j N_j^i r_j + \sum_{j,k} N_{j,k}^i r_{j,k} + \sum_{j,k,l} N_{j,k,l}^i r_{j,k,l}. \quad (2.25)$$

The  $N_i$ 's specify how many particles are created or destroyed in a given reaction (and are thus positive or negative integers). They also contain a correction for identical particles in the initial or final channel.

Since we are only interested in changes in abundances due to reactions we want to exclude changes purely due to changes in volume of the gas. In order to achieve this a new quantity, the nuclear abundance  $Y_i$ , is introduced. The nuclear abundance is defined as

$$Y_i = \frac{n_i}{\rho N_A}. \quad (2.26)$$

The mass fraction of a nucleus with atomic weight  $A_i$  is related to the abundance through  $X_i = A_i Y_i$ . The mass fractions fulfill the relation  $\sum_i X_i = 1$ . The nuclear reaction network in terms of nuclear

abundances  $Y_i$  is given by the following set of differential equations (for each nucleus  $i$  to be followed there is one such differential equation):

$$\dot{Y}_i = \sum_j N_j^i \lambda_j Y_j + \sum_{j,k} N_{j,k}^i \rho N_A \langle j, k \rangle Y_j Y_k + \sum_{j,k,l} N_{j,k,l}^i \rho^2 N_A^2 \langle j, k, l \rangle Y_j Y_k Y_l \quad (2.27)$$

In astrophysical applications a variety of reactions contribute to the production and destruction of a given nucleus. Formally, these reactions can be group into three (functional) groups, depending on the number of nuclei in the initial channel of the reaction: (i) 1-body reactions (decays, photodisintegrations, electron captures, positron captures, neutrino/antineutrino captures), (ii) 2-body reactions (two-particle nuclear reactions), (iii) 3-body reactions (three-particle nuclear reactions such as the triple-alpha reaction).

### 2.3.2 Energy Generation

The main effect of nuclear reactions are abundance changes. Secondary effects are energy release/absorption and (local) changes in hydrodynamic quantities like pressure or temperature. Since the thermonuclear reaction rates depend exponentially on the temperature, (even small) changes in the temperature due to release/absorption of energy are important. This provides the strongest coupling between changes in thermonuclear processes and hydrodynamic processes.

The energy generation is due to changes in the total mass,  $\dot{E} = \dot{M}c^2$ , where  $M = \sum_i n_i m_i V$  is the total mass per volume  $V$ . The energy generation is therefore related to changes in the number densities of the species involved,

$$\dot{E} = -V \sum_i \left( \frac{\partial n_i}{\partial t} \right)_{\rho=\text{const}} m_i c^2, \quad (2.28)$$

or equivalently to the nuclear abundance  $Y_i$  via

$$\dot{E} = -\rho N_A V \sum_i \dot{Y}_i m_i c^2. \quad (2.29)$$

The rate of energy release per gram of matter is

$$\dot{\epsilon}_{\text{nuc}} = -N_A \sum_i \dot{Y}_i m_i c^2 \quad (\text{MeV g}^{-1} \text{ s}^{-1}). \quad (2.30)$$

Decreasing mass means stronger binding and therefore energy release. In Eq. (2.30) the actual nuclear mass can be used as well as the nuclear mass excess  $M_{\text{ex}} = m_i - A_i m_u$  ( $m_u$  is the atomic mass unit) since all reactions conserve baryon number. The nuclear energy release is deposited locally, however there are situation where the energy is not deposited locally, e.g. neutrinos can carry away energy as they escape from the star. In this case, an averaged energy loss term,  $\dot{\epsilon}_{\nu\text{nucl}} = \sum_i \langle E_\nu \rangle \dot{Y}_{i,\text{weak}}$ , can be constructed [65].

### 2.3.3 Solving the Thermonuclear Reaction Network

The nuclear reaction network consists of a set of coupled non-linear first-order differential equations as derived in Eq. (2.27). In principle, this can be solved by any algorithm discussed in literature. However, the physics constrain the optimal choices. The large number of reactions exhibit an almost equally large number of timescales (see Eq. (2.6)) on which the reactions occur. Numerical system which depend on a large range of timescales are called *stiff*. In solving such systems the size of the time step is limited by numerical stability and not by accuracy.

Most nucleosynthesis calculations use — for simplicity — a simple finite difference prescription:

$$\frac{\vec{Y}(t + \Delta t) - \vec{Y}(t)}{\Delta t} = (1 - \Theta) \dot{\vec{Y}}(t + \Delta t) + \Theta \dot{\vec{Y}}(t). \quad (2.31)$$

Here,  $\Delta t$  is the network timestep and  $Y(t + \Delta t)$  is the desired solution. For  $\Theta = 1$  this is an explicit Euler method which is first order accurate. For  $\Theta = 0$ , Eq. (2.31) is the implicit backward Euler

method, being also first order accurate. For  $\Theta = 0.5$ , Eq. (2.31) becomes the semi-explicit trapezoidal method which has second order accuracy. In most astrophysical applications a fully implicit treatment is most successful [65]. Choosing the simple finite difference prescription also has advantages of coupling low order methods to hydrodynamics.

Solving Eq. (2.31) in the fully implicit case is equivalent to finding the zeros of

$$\vec{\mathcal{L}}(t + \Delta t) \equiv \frac{\vec{Y}(t + \Delta t) - \vec{Y}(t)}{\Delta t} - \dot{\vec{Y}}(t + \Delta t) = 0. \quad (2.32)$$

The method of choice for this is the Newton-Raphson method, using a Taylor expansion for  $\vec{\mathcal{L}}(t + \Delta t)$ . For the trial abundances,

$$\Delta \vec{Y} = \left( \frac{\partial \vec{\mathcal{L}}(t + \Delta t)}{\partial \vec{Y}(t + \Delta t)} \right)^{-1} \vec{\mathcal{L}}, \quad (2.33)$$

the Jacobian matrix  $\partial \vec{\mathcal{L}} / \partial \vec{Y}$  has to be computed. The singularity of Eq. (2.32) can potentially be a numerical problem. The individual matrix elements have the form:

$$\frac{\partial \mathcal{L}}{\partial Y_i} = \frac{\delta_{ij}}{\Delta t} - \frac{\partial \dot{Y}_i}{\partial Y_j} = \frac{\delta_{ij}}{\Delta t} - \sum \frac{1}{\tau_j(i)} \quad (2.34)$$

where  $\tau_j(i)$  is the timescale for destruction of nucleus  $i$  by particle  $j$  (see Eq (2.6)). Since more than one reaction can contribute to the destruction of nucleus  $i$  we need to sum over all contributions. The sum is dominated by the fastest reaction. Thus, the term  $\sum 1/\tau_j(i)$  can be orders of magnitude larger than  $1/\Delta t$ , in particular near equilibrium conditions. This can be ameliorated by using physically motivated specializations, see e.g. [65].

For large nuclear reaction networks, the size of the matrix is  $N = 100\text{--}3000$ . The solution of dense matrices scales with  $O(N^3)$ , making the solution computationally expensive. In theory every nucleus can react with every other nucleus. However, in practice in most cases the vast majority of reactions can be neglected. The only important reactions for each nucleus are (with a few exceptions) reactions which capture a neutron, a proton, an  $\alpha$ -particle, or a  $\gamma$  and emit a different one of these particles. The resulting Jacobian matrix is sparse and band diagonal. Other practical aspects of solving nuclear reaction networks includes the amount of memory required to keep track of all the abundances for a large number of computational cells.

## 2.4. Nuclear Statistical Equilibrium

For temperatures above  $(3\text{--}4) \times 10^9$  K any two nuclei are connected through reactions which proceed in both directions. Capture reactions take place due to the high temperatures making it possible to overcome the Coulomb barriers. In the inverse direction, photodisintegrations occur due to the high energy tail in the Planck distribution of photons at high temperatures. In this chemical equilibrium, the nuclear abundances only depend on the nuclear mass, the density, and temperature. This is called *nuclear statistical equilibrium* (NSE).

In this equilibrium situation, the following equalities hold for the chemical potentials

$$\begin{aligned} \bar{\mu}(Z, N) + \bar{\mu}_n &= \bar{\mu}(Z, N + 1) \\ \bar{\mu}(Z, N) + \bar{\mu}_p &= \bar{\mu}(Z + 1, N) \end{aligned} \quad (2.35)$$

of individual neutron and proton captures. In general, for a nucleus with  $N$  neutrons and  $Z$  protons this is equivalent to:

$$N\bar{\mu}_n + Z\bar{\mu}_p = \bar{\mu}_{Z,N}. \quad (2.36)$$

For nuclei, e.g. in an astrophysical plasma, obeying a Maxwell-Boltzmann distribution the chemical potentials are

$$\bar{\mu}_i = kT \ln \left( \frac{\rho N_A Y_i}{G_i} \left( \frac{2\pi\hbar^2}{m_i kT} \right)^{3/2} \right) + m_i c^2. \quad (2.37)$$

The abundance of a nucleus with  $N$  neutrons and  $Z$  protons is then

$$Y(Z, N) = G_{Z,N} (\rho N_A)^{A-1} \frac{A^{3/2}}{2^A} \left( \frac{2\pi\hbar^2}{m_u kT} \right)^{\frac{3}{2}(A-1)} \exp(B_{Z,N}/kT) Y_n^N Y_p^Z. \quad (2.38)$$

In order to solve this equation for the full NSE abundances two additional equations are needed to determine the neutron and protons abundances,  $Y_n$  and  $Y_p$ . These constraints are the total mass conservation,

$$\sum_i A_i Y_i = 1, \quad (2.39)$$

and the relation for the electron fraction  $Y_e$ ,

$$\sum_i Z_i Y_i = Y_e. \quad (2.40)$$

The nuclear abundance distributions are uniquely determined by Eq. (2.38). At high densities large nuclei are favored (dominant term is  $\rho^{A-1}$ ). For high temperatures, the term  $(kT)^{-\frac{3}{2}(A-1)}$  dominates and small nuclei are favored. Finally, for intermediate conditions, a nuclear abundance distribution around  $^{56}\text{Fe}$ , where the tightest bound nuclei are found, is expected due to the dominance of  $\exp(B_{Z,N}/kT)$ .





---

## Inputs and Explosion Models

### 3.1. Inputs

---

For astrophysical nucleosynthesis calculations inputs from many fields are required. In the case of core collapse supernova nucleosynthesis calculations the relevant inputs include cross sections and reaction rates, the equation of state to describe dense nuclear matter, the model of the progenitor star, the treatment of neutrino transport, and the details of the hydrodynamical treatment (e.g. 1D or multi-D, Newtonian gravity or general relativity). In this Chapter the various inputs are described in direct connection to the present work.

#### 3.1.1 Reaction Rates

In Chapter 2, the conceptual aspects of thermonuclear reaction rates and nuclear reaction networks have been discussed. To use these nuclear reaction networks for nucleosynthesis calculations in an astrophysical scenario two types of information are needed: the thermonuclear reaction rate and the temporal behavior of hydrodynamical quantities (e.g. temperature and density) in the given scenario. The most important ingredients to the thermonuclear reaction rate in nucleosynthesis calculations are half-lives, electron and positron capture rates, photodisintegrations, neutrino induced reaction rates, and strong interaction cross sections.

For hydrostatic burning (e.g. during stellar evolution) the timescales for nuclear burning is given by the energy loss timescales. These timescales are long and thus nuclear burning proceeds mainly through stable nuclei. For example for a  $25 M_{\odot}$  star, the timescales for hydrostatic burning range from  $7 \times 10^6$  years (H-burning) to 1 day (Si-burning). In the case of less massive stars, these timescales are even longer. During explosive burning (e.g. in core collapse supernovae) the timescales are determined by the hydrodynamics and therefore are much shorter. The beta-decay half-lives of unstable nuclei are in this case longer than the hydrodynamic timescale. This requires nuclear reaction cross sections for a large number of intermediate and heavy unstable nuclei.

The most desirable approach is of course the direct experimental measurements of the nuclear cross sections of interest. Many of the intermediate and heavy nuclei involved in explosive burning are experimentally not (yet) accessible. However, they intrinsically have a high density of excited states, making the statistical model approach (Hauser-Feshbach) appropriate. Compilations for unstable nuclei using the Hauser-Feshbach method (e.g. [123]) are widely used in astrophysics. If the statistical model is not suitable (i.e. the compound nucleus has a low level density) other methods must be used to estimate the cross section from nuclear structure information of the involved nuclei.

#### Neutral and Charged Particle Reactions

In this work we use a recent REACLIB compilation for the neutral and charged particle reactions. In this reaction rate library, the basis for the individual rates,  $\lambda_j$ ,  $\langle j, k \rangle$ , and  $\langle j, k, l \rangle$ , in the nuclear reaction network (Eq. 2.27) are the following sources. Experimental rates for light nuclei come from [28], neutron capture cross sections from [9, 10], rates for unstable light nuclei are taken from experiments whenever available. The beta-decay half lives, if not known experimentally, are taken from [81, 131]. The compilation includes experimental rates from [1]. The capture cross sections for the vast number of intermediate and heavy nuclei with a high density of excited states at the relevant energies are calculated using a Hauser-Feshbach model [123]. For a detailed discussion of the method, see e.g. [40]. This REACLIB compilation has previously been used in [124] for rp-process calculations.

Mass Number	Nuclides	Mass Number	Nuclides
1	n, H	43	Ti, Sc, Ca, K, Ar, Cl
21	Mg, Na, Ne, F, O	44	V, Ti, Sc, Ca, K, Ar
22	Mg, Na, Ne, F	45	Cr, V, Ti, Sc, Ca, K
23	Al, Mg, Na, Ne, F	46	Cr, V, Ti, Sc, Ca, K
24	Si, Al, Mg, Na, Ne	47	Cr, V, Ti, Sc, Ca, K
25	Si, Al, Mg, Na, Ne	48	Cr, V, Ti, Sc, Ca, K
26	Si, Al, Mg, Na	49	Fe, Mn, Cr, V, Ti, Sc, Ca, K
27	P, Si, Al, Mg, Na	50	Mn, Cr, V, Ti, Sc, Ca
28	S, P, Si, Mg, Na	51	Mn, Cr, V, Ti, Sc, Ca
29	S, P, Si, Al, Mg, Na	52	Fe, Mn, Cr, V, Ti, Sc
30	S, P, Si, Al	53	Co, Fe, Mn, Cr, V, Ti
31	Cl, S, P, Si, Al	54	Co, Fe, Mn, Cr, V, Ti
32	Ar, Cl, S, P, Si	55	Ni, Co, Fe, Mn, Cr, V, Ti
33	Ar, Cl, S, P, Si	56	Ni, Co, Fe, Mn, Cr, V, Ti, Sc
34	Ar, Cl, S, P, Si	57	Zn, Cu, Ni, Co, Fe, Mn, Cr, V
35	K, Ar, Cl, S, P	58	Cu, Ni, Co, Fe, Mn, Cr, V, Ti
36	Ca, K, Ar, Cl, S	59	Cu, Ni, Co, Fe, Mn, Cr, V
37	Ca, K, Ar, Cl, S	60	Zn, Cu, Ni, Co, Fe, Mn, Cr, V, Ti
38	Ca, K, Ar, Cl, S	61	Zn, Cu, Ni, Co, Fe
39	Ca, K, Ar, Cl	62	Ga, Zn, Cu, Ni, Co, Fe
40	Ti, Sc, Ca, K, Ar, Cl	63	Ga, Zn, Cu, Ni, Co, Fe
41	Ti, Sc, Ca, K, Ar, Cl	64	Ge, Ga, Zn, Cu, Ni, Co, Fe
42	Ti, Sc, Ca, K, Ar	65	Ge, Ga, Zn, Cu, Ni, Co

**Table 3.1:** All nuclei per given mass number for which weak interactions by [53, 54] and by [85] are used in the nuclear network.

### Weak Interactions

The electron and positron capture rates are taken from [53, 54] (FFN) for nuclei with  $A \leq 45$  (*sd*-shell) and from [85] (LMP) for mass range  $45 < A \leq 65$  (*pf*-shell). A complete list of all nuclei for which electron/positron captures by FFN or LMP are used is given in Table 3.1. In the newer compilations, [55, 85] a different tabulation is used (involving  $\log\langle ft \rangle$ -values instead of capture rates) for a more accurate interpolation. For details refer to [15].

### 3.1.2 Neutrino-Induced Reactions

In core collapse supernovae the neutrinos carry most of the  $\sim 10^{53}$  erg gravitational binding energy released during core collapse (see also Section 1.1.2). These neutrinos can interact with the matter they pass through as they leave the star and effect the dynamics as well as the composition.

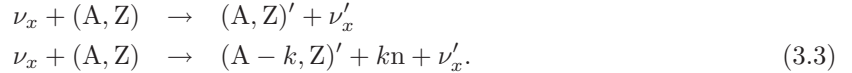
Neutrinos can react with free nucleons and with nuclei either through *charged current* reactions or through *neutral current* reactions. The charged current reactions produce a lepton in the final state of the reaction (semileptonic process). In theory, this is possible with all six neutrino flavor ( $\nu_e, \bar{\nu}_e, \nu_\mu, \bar{\nu}_\mu, \nu_\tau, \bar{\nu}_\tau$ ). However, in supernovae charged current reactions are possible only with electron neutrinos,  $\nu_e$ , and electron antineutrinos,  $\bar{\nu}_e$  due to energetics (muons and taus are too heavy to be produced at supernova energies). Electron neutrino/antineutrino capture reactions occur on free nucleons as well as on nuclei:

$$\begin{aligned} \nu_e + n &\rightarrow p + e^- \\ \nu_e + (A, Z) &\rightarrow (A, Z+1) + e^- \end{aligned} \quad (3.1)$$

$$\begin{aligned} \bar{\nu}_e + p &\rightarrow n + e^+ \\ \bar{\nu}_e + (A, Z) &\rightarrow (A, Z-1) + e^+. \end{aligned} \quad (3.2)$$

Charged current reactions on free nucleons dominate the energy transfer from the neutron star to the shock and subsequently to the mantle. These reactions also play a vital role in setting the neutron to proton ratio in the innermost ejecta (the details are discussed in Section 3.2.3). Charged current capture reactions on nuclei have smaller cross sections than the capture reactions on free nucleons. They might nevertheless be important ahead of the shock for so called “pre-heating” (dissociating a fraction of the nuclei) of the material, see [8] for details. Neutrino capture on heavy nuclei can leave the daughter nucleus in an excited state, allowing the decay via neutron emission or fission [8]. These neutrino-induced fission reactions are not included in our nucleosynthesis calculations.

Neutral current reactions on the other hand can occur involving every flavor of neutrinos,



Of these reactions, only inelastic scattering (second reaction in Eq. (3.3)) excites the nucleus and opens the channel for (light) particle emission like neutrons. In addition to changing the composition, inelastic scattering reactions can heat the material through energy transfer. Other processes involving neutrinos (like neutrino-electron scattering, neutrino-positron scattering, or neutrino-antineutrino production from pair annihilation) are also vital for supernova simulations [25]. However, these processes do not change the electron fraction  $Y_e$  of matter (and therefore its composition). Hence, they are included in the hydrodynamical simulations but not in the nucleosynthesis calculations. Nevertheless, neutrino-induced spallation reactions can change the final abundances of some nuclei and we will investigate this in future calculations.

### Cross Sections

For the charged current neutrino/antineutrino capture cross sections on free nucleons we use the analytic expressions from [25]:

$$\sigma(\epsilon_{\nu_e}) = \sigma_0 \left( \frac{1 + 3g_A^2}{4} \right) \left( \frac{\epsilon_{\nu_e} + \Delta_{np}}{m_e c^2} \right)^2 \left[ 1 - \left( \frac{m_e c^2}{\epsilon_{\nu_e} + \Delta_{np}} \right)^2 \right]^{1/2} W_M\tag{3.4}$$

and

$$\sigma(\epsilon_{\bar{\nu}_e}) = \sigma_0 \left( \frac{1 + 3g_A^2}{4} \right) \left( \frac{\epsilon_{\bar{\nu}_e} - \Delta_{np}}{m_e c^2} \right)^2 \left[ 1 - \left( \frac{m_e c^2}{\epsilon_{\bar{\nu}_e} - \Delta_{np}} \right)^2 \right]^{1/2} W_{\bar{M}}\tag{3.5}$$

where  $\sigma_0 = \frac{4G^2(m_e c^2)^2}{\pi(\hbar c)^2} \sim 1.705 \times 10^{-44} \text{ cm}^2$  and

$$\begin{aligned}W_M &= 1 + \frac{1.1\epsilon_{\nu_e}}{m_n c^2} \quad (\text{for } \nu_e + n \rightarrow p + e^-) \\ W_{\bar{M}} &= 1 - \frac{7.1\epsilon_{\bar{\nu}_e}}{m_n c^2} \quad (\text{for } \bar{\nu}_e + p \rightarrow n + e^+).\end{aligned}\tag{3.6}$$

Here,  $g_A$  is the axial-vector coupling constant,  $\Delta_{np}$  the neutron-proton mass difference,  $m_e$  the electron mass, and  $W_M$  and  $W_{\bar{M}}$  the corrections for weak magnetism. These cross sections per baryon are larger than for any other process [25]. From experiments we know that at high energies the antineutrino-nucleon cross sections are systematically smaller than neutrino-nucleon cross sections. This can be accommodated in theoretical calculations by the inclusion of free space corrections (*weak magnetism* corrections). The weak magnetism arises due to parity violating interference between the weak magnetic moment of a nucleon and its axial vector current and is independent of the model used to describe dense matter. Core collapse supernova simulations and especially core collapse nucleosynthesis calculations benefit from this effect as it has opposite signs for neutrinos and antineutrinos (i.e. it increases the opacity for neutrinos and decreases the opacity of antineutrinos).

The cross sections for charged current capture of neutrinos/antineutrinos on nuclei are taken from a recent calculation [159]. They are based on the random phase approximation calculations [83, 84]. Compared to the previously available cross sections (including empirical estimates [59, 119] or independent particle model calculations [56, 98]) this compilation covers the whole range of nuclei important for explosive nucleosynthesis on a wide grid of parameter values for  $T_\nu$  and  $\alpha$ . Table 3.2 summarizes the nuclei for which neutrino and antineutrino captures are included in the nucleosynthesis calculations.

Element	Mass Range ( $\nu$ capture)	Mass Range ( $\bar{\nu}$ capture)	Element	Mass Range ( $\nu$ capture)	Mass Range ( $\bar{\nu}$ capture)
n	1	1	Fe	48–64	46–64
H	1	1	Co	50–66	49–66
He	6	6	Ni	52–68	51–68
Li	7–9	7–9	Cu	54–70	53–70
Be	8–12	8–12	Zn	56–74	55–74
B	10–14	10–14	Ga	58–78	57–78
C	11–18	11–18	Ge	60–78	59–78
N	13–21	13–21	Se	67–84	66–84
O	14–22	14–22	Br	69–86	68–86
F	16–26	16–26	Kr	71–92	70–92
Ne	18–29	17–29	Rb	73–92	72–92
Na	20–32	19–22	Sr	77–94	74–92
Mg	21–35	21–35	Y	79–96	78–94
Al	22–37	22–37	Zr	81–98	80–96
Si	24–39	23–39	Nb	83–100	82–98
P	26–42	25–42	Mo	85–102	84–100
S	28–42	27–42	Tc	87–104	86–102
Cl	30–42	29–42	Ru	89–108	88–104
Ar	32–44	31–44	Rh	91–110	90–108
K	34–48	33–48	Pd	94–114	92–110
Ca	36–50	35–50	Ag	96–116	95–114
Sc	38–52	37–52	Cd	98–118	97–116
Ti	40–54	39–54	In	100–120	99–119
V	42–56	41–56	Sn	—	101–120
Cr	44–58	43–58			
Mn	45–62	45–62			

**Table 3.2:** Nuclides for which neutrino and anti-neutrino capture reactions are included in the nuclear network. The mass range given indicates for each element the nucleus with the lowest mass number and the nucleus with the highest mass number.

Neutrino Flavor	$T_\nu$ [MeV]	$\alpha$	Reference
$\nu_e$	3.0	4.8	[106] <sup>1</sup>
$\nu_x$	3.0	4.8	[106] <sup>1</sup>
$\nu_e$	4.0	0	[152]
$\bar{\nu}_e$	5	0	[152]
$\nu_x$	8	0	[152]
$\nu_e$	2.8	3	[76]
$\bar{\nu}_e$	4	3	[76]
$\nu_x$	6.4	3	[76]

**Table 3.3:** Summary of the commonly adopted numerical values for  $T_\nu$  and  $\alpha$  used in Fermi-Dirac spectra for supernova neutrinos. *Note:*  $\nu_x$  stands for the neutrino flavors  $\nu_\mu$ ,  $\bar{\nu}_\mu$ ,  $\nu_\tau$ , and  $\bar{\nu}_\tau$ .

<sup>1</sup> These values are the fit values at shock break-out. The authors give different fit values at different times of the evolution (see Tables 1 – 3 therein).

### Consistent Coupling of the Neutrino-Induced Reactions for Nucleosynthesis with the Underlying Dynamics

For use in astrophysical applications the (energy dependent) cross section  $\sigma(E, T_\nu)$  has to be folded with an appropriate energy distribution for neutrinos (see Eq. 2.24 in the previous Chapter):

$$\sigma(T_\nu) = \int_{E_{\min}}^{\infty} \sigma(E, T_\nu) f(E) dE. \quad (3.7)$$

(The mean neutrino energy  $\langle \epsilon_\nu \rangle$  is related to the neutrino temperature through  $\langle \epsilon_\nu \rangle \sim 3.15 T_\nu$ .) For core collapse supernovae the neutrino spectra shortly after core collapse can be approximated by a Fermi-Dirac spectrum depending on the neutrino temperature  $T_\nu$  and a parameter  $\alpha$  related to the degeneracy of the chemical potential:

$$f(E) = \frac{1}{F_2(\alpha)} \frac{1}{T_\nu^3} \frac{E^2}{\exp(\frac{E}{T_\nu} - \alpha) + 1}, \quad (3.8)$$

where  $F_2(\alpha)$  is a normalization constant and  $E$  is the neutrino energy. Values for the temperature  $T_\nu$  and for  $\alpha$  are obtained from fits to spectra. In core collapse nucleosynthesis calculations temporally constant values are broadly used for the neutrino temperatures. However, simulations with detailed neutrino transport show that this is only valid for the long term evolution. Shortly after bounce the neutrino temperatures still vary before the asymptotically value is assumed (see e.g. Fig. 3.1). Commonly used numerical values are summarized in Table 3.3.

In this thesis I implemented a new approach: We use model dependent values for  $T_\nu$  (at  $\alpha = 0$ ) from fits to the actual neutrino spectrum at each time step in the core collapse simulation with detailed neutrino transport. This treatment accommodates for temporal changes in the neutrinos temperatures after shock break-out as well as for the variations in the neutrino properties from model to model (dependent on the progenitor mass, the explosion energy, and the mechanism to trigger the explosion).

Following the general recipe in Chapter 2 of using a density and temperature dependent “decay constant” for the rate of neutrino-induced reactions (see Eq. (2.24)) detailed knowledge of the cross sections, the neutrino spectra, and of the neutrino flux is required. With the current computational power available realistic core collapse simulations with accurate neutrino transport are only able to proceed to a few hundred milliseconds after bounce. However, for accurate nucleosynthesis predictions the long term evolution of the neutrino luminosity is also of importance. Due to the lack of availability from simulations I approximate the luminosity after shock breakout at the neutrinos sphere ( $\sim 4$  ms after maximum density) by an exponential decay with time constant  $\tau \sim 3$  s [36]:

$$L_\nu = \frac{E_\nu}{\tau} \exp(-t/\tau) \quad (3.9)$$

where  $E_\nu = E_G/6$  is the energy carried per neutrino flavor. A typical value is  $E_\nu = E_G/6 = 5 \times 10^{52}$  erg [152].

Putting everything together the flux history of each neutrino flavor is then

$$\phi_\nu = \frac{c}{r^2} L_\nu \text{ cm}^{-2} \text{ s}^{-1}, \quad (3.10)$$

where  $r$  is the distance of the matter from the center and  $c$  is a normalization constant. The reaction rate per neutrino flavor is then given by:

$$\lambda_{\nu,\nu'}(T_\nu) = \sigma_{\nu,\nu'}(T_\nu) \phi_\nu. \quad (3.11)$$

where  $\sigma_{\nu,\nu'}(T_\nu)$  is the inelastic neutrino/antineutrino cross section averaged over the neutrino spectrum of temperature  $T_\nu$ . The reaction rate  $\lambda$  has units of  $\text{s}^{-1}$ , as required.

Summarizing, using this new treatment for the neutrino temperatures and taking all weak interactions contributing to changes of  $Y_e$  into account allows for consistent calculations of core collapse supernova nucleosynthesis. The results of these calculations are presented and discussed in the following chapters.

### 3.1.3 Progenitors

The core collapse supernova models used in this thesis are based on progenitor models from different groups. The model series A and B use the progenitor model with main sequence mass of  $20 M_\odot$  by Nomoto & Hashimoto [109]. This star is evolved from a  $6 M_\odot$  He-star, undergoing all the hydrostatic burning stages, and eventually ending with an iron core of  $1.65 M_\odot$ . For silicon burning a nuclear network of 250 nuclear species is used. The progenitor model was followed until the onset of collapse (central density being at  $10^{10} \text{ g/cm}^3$ ).

The progenitor model for the  $20 M_\odot$  model (part of series LS07), extensively discussed in Section 4.6, is taken from [144] and is the same as that being used in [142]. The model series LS07 employs progenitor structures of  $13 M_\odot$ ,  $15 M_\odot$ ,  $18 M_\odot$ ,  $25 M_\odot$ , and  $30 M_\odot$  also from [142, 144]. These models are evolved with a Henyey type code including metallicity dependent mass loss. A nuclear reaction network of 51 isotopes is used for hydrogen and helium burning. For the burning stages after He burning a larger network including 240 isotopes is used.

The size of the Fe-core (here, defined as the region with the electron fraction  $Y_e \leq 0.49$ ) for the different models at the onset of collapse is given in Table 3.1.3. In the future, we will also use progenitors by [153]. These are non-rotating pre-supernova models with main sequence masses of  $10.8 M_\odot$ ,  $13 M_\odot$ ,  $15 M_\odot$ ,  $20 M_\odot$ ,  $25 M_\odot$ ,  $30 M_\odot$ , and  $35 M_\odot$  at solar metallicity.

		initial mass [ $M_\odot$ ]				
Z	13	15	18	20	25	30
0.02	1.27	1.34	...	1.52	1.67	...

**Table 3.4:** Fe-core masses for the progenitor models of [144]. Here, the Fe-core is defined as the region with an electron fraction  $Y_e \leq 0.49$ . No values are given for the  $18 M_\odot$  and  $30 M_\odot$  in [144].

### 3.1.4 The Equation of State

Core collapse simulations depend on input from nuclear physics. One of the most important nuclear inputs is the equation of state. The equation of state relates the temperature, density, and electron fraction of the material with its pressure, internal energy, composition etc.

For the core collapse simulations used in this thesis for explosive nucleosynthesis investigations the Lattimer & Swesty equation of state [87] has been employed. In this equation of state the matter consists of photons, electrons, positrons, free neutrons, free protons, alpha particles (representing the

light nuclei), and a "heavy nucleus" (average of different nuclei heavier than alpha particles). It employs a compressible liquid drop model for nuclei. The nuclear force (potential or mean field interaction) can be adjusted and takes nuclear parameters as input. These parameters include: the saturation density of symmetric nuclear matter, the binding energy of saturated, symmetric nuclear matter, the incompressibility of bulk nuclear matter, the symmetry energy parameter of bulk nuclear matter, and the bulk level density parameter. Some of these nuclear parameter can have relatively large uncertainties.

In the future, we also plan to use core collapse supernova simulations which employ the Shen equation of state [125, 126]. This equation of state uses a relativistic mean field approach. Matter consists of neutron, protons, alpha particles, and nuclei in equilibrium. The parameters are a parameter set TM1 (for details, see [125] or [126]), the symmetry energy, and the compressibility. Since this equation of state exhibits a different compressibility we expect a different behavior of the core collapse simulations [44] and therefore differences in the nucleosynthesis resulting from these models.

## 3.2. Core Collapse Supernova Models with Neutrino Transport

In this Section the hydrodynamical models will be presented on which the nucleosynthesis investigations are based. We will discuss the features of these models, with an emphasis on aspects relevant to explosive nucleosynthesis. The discussion of the influence of neutrino radiation on matter and on the electron fraction is based on two model series: series A and series B. The analyses in Sections 3.2.2 and 3.2.3 are work done by M. Liebendörfer.

### 3.2.1 Hydrodynamics

The framework for this investigation are spherically symmetric simulations with implicit general relativistic Boltzmann neutrino transport, see [104] and [88] for a detailed description of the code AGILE-BOLTZTRAN. It features a dynamically adaptive grid [90] that concentrates grid points at the developing mass cut. The simulations are performed until the density drops to  $\sim 10^6$  g/cm<sup>3</sup> in the region of bifurcation between the ejecta and the remnant. At this time, the mass contained in radial mass zones is becoming very small and the run experiences ill-conditioned Jacobian matrices in the Newton-Raphson scheme. A major feature of these simulations is — in the context of nucleosynthesis — the emergence of the mass cut (separating remnant and ejecta) consistently from the simulations.

The simulations are then continued by an explicit hydrodynamic code. This code employs an explicit difference scheme similar to [35] and a simplified nuclear reaction network [17]. The reaction network is a so-called  $\alpha$ -network, consisting of <sup>4</sup>He, <sup>12</sup>C, <sup>16</sup>O, <sup>20</sup>Ne, <sup>24</sup>Mg, <sup>28</sup>Si, and <sup>56</sup>Ni. These nuclei are connected through ( $\alpha, \gamma$ ) reactions (and their inverse reactions), plus the triple- $\alpha$  reaction, <sup>12</sup>C + <sup>12</sup>C and <sup>16</sup>O + <sup>16</sup>O reactions, and <sup>28</sup>Si + 7 $\alpha$  (to simulate Si-burning). The rates are taken from [28]. Such reduced  $\alpha$ -network (while not suitable to trace the detailed abundance changes) enables the energy feedback from nuclear burning to the hydrodynamics of the problem (reactions involving the  $\alpha$ -nuclei are the main sources for the energy production from nuclear burning).

In our models we use two different approaches to enforce explosions in otherwise non-explosive supernova models.

1. We parametrize the neutral current neutrino scattering opacities on free nucleons with a factor ranging from 0.1 to 0.7 (series A).
2. We multiply the absorptivities and emissivities (i.e. the reaction rates for forward and backward reactions in  $\nu_e + n \rightleftharpoons p + e^-$  and  $\bar{\nu}_e + p \rightleftharpoons n + e^+$ ) in the heating region by equal factors (series B).

For the models of series A, in addition to scaling the neutral current neutrino scattering opacities on free nucleons, we also use a finite differencing (see footnote 1 in [49] for details) that helps to artificially increase the diffusive fluxes in regions of very high matter density. The net result is a faster deleptonization of the protoneutron star such that the neutrino luminosities are boosted in the heating region. For the sake of computational efficiency, this first series of parametrized runs (series A) has been calculated with the lowest possible angular resolution, involving only inwards and outwards propagating neutrinos. However, all of these measures only affect the propagation of neutrinos in the model; the models are still closed and respect energy and lepton number conservation. We expect that series A represents a simplification of the phenomenology of supernovae that would be driven by higher neutrino luminosities than in the standard cases, for example different forms of protoneutron star convection [20, 79, 102, 149] or improvements in the uncertain nuclear matter physics.

The simulations of the second series (series B) in this parameter study were performed using standard resolution (6 angular bins, 12 energy groups) for the Boltzmann neutrino transport. Series B also includes the weak magnetism corrections in the neutrino cross sections [69]. Enhancing the absorptivities and emissivities in the heating region reduces the timescale for neutrino heating without changing the important equilibrium  $Y_e$  and temperature. With this approach we hope to mimic a potentially increased heating efficiency in the heating region as is expected in combination with overturn in this convectively unstable domain [21, 26, 62, 77, 102].

The parameters in series A and B are chosen such that each series contributes with a barely exploding model, an extremely exploding model (in terms of parameter range, the explosion energy itself seems



Run	Parameter	$E_{\text{expl}}$ [erg]	$m_{\text{cut}}$ [ $M_{\odot}$ ]	$t_{v>0}$ [s]	$t_{\text{end}}$ [s]
A60	60% scatt.	$0.24 \times 10^{51}$	1.585	0.46	0.64
A40	40% scatt.	$0.78 \times 10^{51}$	1.511	0.27	0.53
A20	20% scatt.	$1.24 \times 10^{51}$	1.444	0.20	0.44
B05	factor 5	$0.31 \times 10^{51}$	1.586	0.38	0.53
B07	factor 7	$0.78 \times 10^{51}$	1.531	0.26	0.43
B10	factor 10	$1.12 \times 10^{51}$	1.509	0.24	0.40

**Table 3.5:** The parameter of series A specifies the percentage of neutral current interactions considered in the model. The parameter of series B specifies the reduction of the heating timescale. The time after bounce where we had to stop the runs with neutrino transport is displayed in the last column labeled by  $t_{\text{end}}$ . The time of the first appearance of positive velocities is given in the column  $t_{v>0}$ . The mass cut  $m_{\text{cut}}$  has been determined at the point where the total energy integrated from outside inwards reaches a maximum. The estimate for the explosion energy  $E_{\text{expl}}$  has been composed from the total energy of the unbound material between the mass cut and the shock front at  $t_{\text{end}}$  (mostly material that was in NSE) and a correction for the total energy of the bound layers ahead of the shock at progenitor composition.

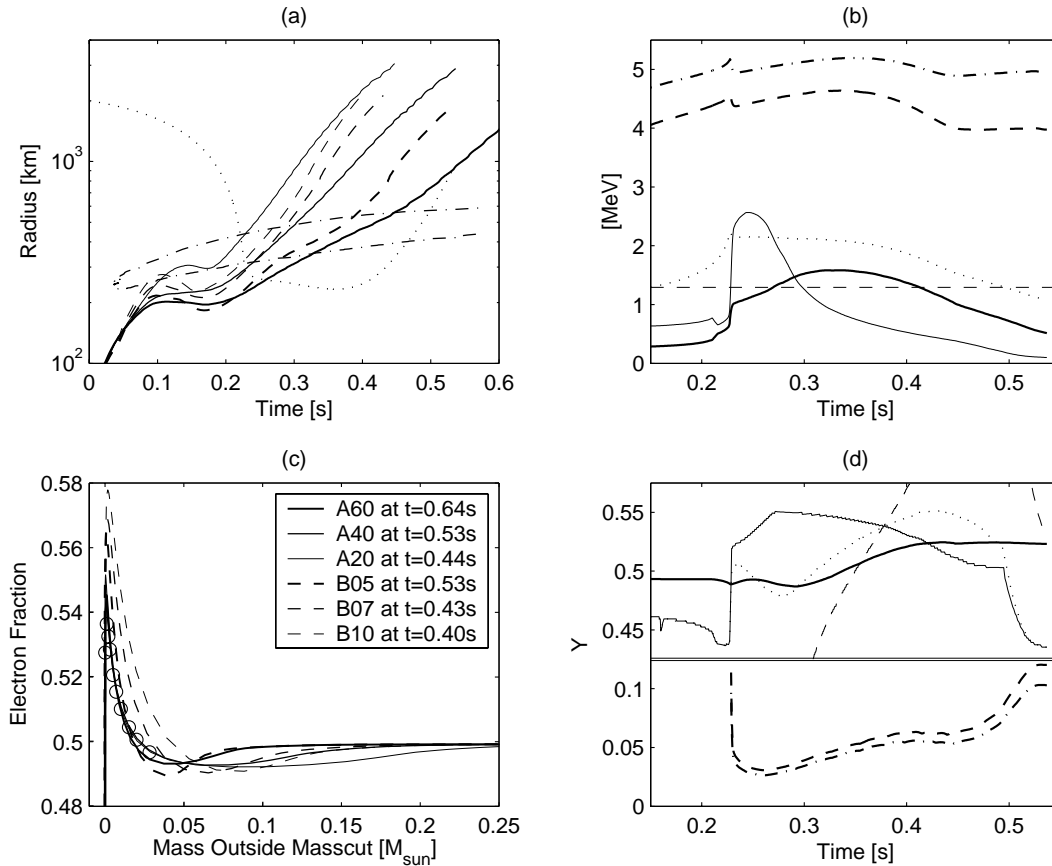
to saturate around  $1.2 \times 10^{51}$  erg), and a model with average parameter setting. Important properties of the different runs are listed in Table 3.5. Based on the parameter studies with series A and B, we use the method of series B with a factor 7 to enhance the rates for the new 20  $M_{\odot}$  model (part of series LS07). An increase in computer power enables us to use 20 energy groups for the Boltzmann neutrino transport.

Figure 3.1a presents an overview of the shock trajectories. Runs from series A are presented with solid lines and runs from series B with dashed lines. The legend in Figure 3.1c also applies to Figure 3.1a. In all runs, the accretion front stalls at about 100 ms after bounce at a radius between 180 and 300 km, depending on the parameters. The accretion front is slowly receding in the more optimistic models. Shortly before 200 ms after bounce, the accretion front moves outward again. There may still be some additional delay until the inwards drifting material behind the shock reverses its velocity and starts to accumulate kinetic energy for the ejection. This happens at 199 ms after bounce for the fastest explosion (A20) and at 461 ms after bounce for the slowest run (A60). Bruenn’s suggestion to locate the mass cut where the integrated total energy of all external material assumes a maximum agrees well with the actual bifurcation in the mass trajectories. The mass cuts,  $m_{\text{cut}}$ , range from 1.444  $M_{\odot}$  to 1.585  $M_{\odot}$ . Realistic 3D calculations where convection (responsible for the corrections applied to the weak rates in both series A and B) turned on in a delayed fashion could delay the explosions and lead to larger mass cuts.

### 3.2.2 Matter in a Neutrino Field

Even though it is uncertain how significantly absorptions of the neutrinos emitted from the protoneutron star surface contribute to the revival of the shock, it is necessary to include the neutrinos and their copious interaction with the matter in the vicinity of the protoneutron star. If the explosion is launched such that the mass cut is directly determined by the early dynamics of the explosion, this neutrino heated material will contribute to the deepest layers of the ejecta. If fallback occurs after the initial explosion, contributions by these innermost layers are only possible if strong mixing occurs. In any case, this neutrino heated material will have significantly changed its composition with respect to its original progenitor composition. Hence, in this section we investigate the conditions in ejecta that are subject to large neutrino fluxes.

The energy spectrum of the neutrinos is set in the vicinity of the neutrinospheres at a radius of initially  $\sim 70$  km. Before the launch of the explosion, about two thirds of the emitted neutrinos stem from the infalling matter which is squeezed in the gravitational potential and settles on the surface of the protoneutron star. The rise in the electron energies by the compression leads to more electron neutrino emissions than electron antineutrino emissions. After the launch of the explosion, this contribution will decrease with the accretion rate and the less accretion-sensitive neutrino diffusion flux from the



**Figure 3.1:** (a) Trajectories of the (accretion-) shock as a function of time. Series A (solid lines) explodes because of artificially increased core diffusion luminosities. The neutral current neutrino opacity is used as parameter with 20% of the standard values (thin line), with 40% (medium line width), and with 60% (thick line). Series B (dashed lines) explodes because of artificially accelerated neutrino absorption and emission processes in the heating region. The acceleration factors are 10 (thin line), 7 (medium line width), and 5 (thick line). See also the legend in panel (c) for an identification of the shock trajectories. The dotted line traces the trajectory of a representative fluid element located at  $0.005 M_{\odot}$  outside of the estimated mass cut. Its electron fraction and specific energy can change by weak interactions on a timescale represented by the dot-dashed lines (reaction time scale as a function of radius). The lower branch belongs to the infall phase and the upper branch to the ejection.

(b) Energy scales sampled at the representative fluid element as a function of time. Thick lines show the fluid temperature (solid), the neutrino temperature (dashed), and the antineutrino temperature (dot-dashed). Thin lines represent the electron chemical potential (solid), the mass difference between neutron and proton (dashed), and the temperature that would be obtained after infinite exposure to the neutrino field (dotted). The electrons in the representative fluid element are degenerate during collapse and after shock compression. Neutrino heating and expansion during the ejection lifts the electron degeneracy and the neutron to proton mass difference becomes the dominant energy scale.

(c) Electron fraction as function of mass when the runs are stopped (0.4 – 0.6 s after bounce) with (A) reduction of the neutral current scattering opacities (solid lines), or (B) enhancement of the reaction timescales (dashed lines). The open circles represent the final electron fractions of run A40 after the freeze-out of charged current interactions.

(d) Abundances sampled at the representative fluid element. Thick lines show the electron fraction (solid), neutrino fraction (dashed), and antineutrino fraction (dot-dashed). Thin lines represent electron fractions that would obtain after infinite exposure to the neutrino field. Only neutrino absorptions have been considered for the solid line and only emissions have been considered for the dashed line. The dotted line includes all charged current reactions. Panel (b) and (d) show that the electron fraction is first kept high by neutrino absorptions, later by neutrino emissions. The electron fraction at freeze-out is determined by competition between the neutrino interaction rates and the matter ejection timescale.

hot protoneutron star will dominate. An energy equipartition among the different neutrino flavors is expected to set in when the accretion luminosities have reduced to a negligible contribution. A more detailed description of this transition, however, requires multi-dimensional simulations because the evolution of the accretion rate shows quite aspherical features with narrow downflows and broad upflows [21, 26, 62, 77] that are ignored in spherical symmetry. The emitted electron flavor neutrinos may essentially interact with the material behind the accretion shock out to radii of about 300 km (“essential” meaning electron fraction changes on a timescale of 100 ms). The interactions decrease steeply with increasing radius due to geometric  $1/r^2$  dilution of the neutrino field.

In order to illustrate the basic behaviour of shock-heated matter in a neutrino bath, we first consider only the four dominant reactions, electron capture on free protons  $e^- + p \rightleftharpoons n + \nu_e$ , and positron capture on free neutrons  $e^+ + n \rightleftharpoons p + \bar{\nu}_e$ , and their inverse reactions. Two independent conditions are required to specify the electron fraction and the entropy of the material, for example weak equilibrium and balance in the energy exchange with neutrinos.

The change of the electron fraction,  $Y_e$ , with time,  $t$ , is given by Eqs. (C15) and (C20) in [18]. The neutrino opacities,  $\chi$ , and emissivities,  $j$ , are linked by the reciprocity relation (detailed balance) described in Eqs. (C7) and (C8) in the above reference. The reciprocity relation involves the temperature,  $kT = \beta^{-1}$ , the neutrino energy,  $E$ , measured in the rest frame of the fluid, and the chemical potentials,  $\mu_n$ ,  $\mu_p$ , and  $\mu_e$ , for neutrons, protons, and electrons respectively. We can therefore label contributions from electron, positron, neutrino, and antineutrino capture with  $EC$ ,  $PC$ ,  $NC$ , and  $AC$  respectively, and express the opacities in  $NC$  and  $AC$  by the neutrino emissivities. After having collected all terms that do not depend on the neutrino energy into a common factor,  $K$ , we write the total change in the electron fraction in the following form:

$$\begin{aligned} \frac{1}{c} \frac{dY_e}{dt} &= K \int dE E^2 [h(E+Q)(-EC + NC) \\ &+ \Theta(E-Q-m_e)h(E-Q)(PC - AC)]. \end{aligned} \quad (3.12)$$

Here, the details of the roughly quadratic energy dependence of the cross sections are hidden in the function

$$h(x) = x^2 \left[ 1 - \left( \frac{m_e c^2}{x} \right)^2 \right]^{1/2},$$

and a step function  $\Theta(x)$  is used to describe the energy threshold in the positron and antineutrino capture reactions. A very similar equation can be used to describe the change of the specific internal energy,  $e$ , of the fluid due to neutrino interactions:

$$\begin{aligned} \frac{1}{c} \frac{de}{dt} &= K \int dE E^3 [h(E+Q)(-EC + NC) \\ &+ \Theta(E-Q-m_e)h(E-Q)(-PC + AC)]. \end{aligned} \quad (3.13)$$

The density in the supernova ejecta is low enough that we can neglect the nucleon degeneracy and nucleon final state blocking described in Eq. (C14) of [18]. The contributions to Eqs. (3.12) and (3.13) from the individual reactions are given by

$$\begin{aligned} EC &= \frac{1}{1 + e^{\beta(E+Q-\mu_e)}} n_p (1 - f_\nu) \\ NC &= \frac{e^{\beta(E+Q-\mu_e)}}{1 + e^{\beta(E+Q-\mu_e)}} n_n f_\nu \\ PC &= \frac{1}{1 + e^{\beta(E-Q+\mu_e)}} n_n (1 - f_{\bar{\nu}}) \\ AC &= \frac{e^{\beta(E-Q+\mu_e)}}{1 + e^{\beta(E-Q+\mu_e)}} n_p f_{\bar{\nu}} \end{aligned} \quad (3.14)$$

where  $n_n$  and  $n_p$  are the neutron and proton number densities, respectively, and  $f(E)$  is the neutrino distribution function in the rest frame of the fluid.

Note that Eqs. (3.12) and (3.13) do not presume that the neutrinos are in equilibrium with matter, nor that they assume any particular spectrum. Some of these assumptions, however, lead to useful

analytical formulas for the equilibrium electron fraction. Dominance of the neutrino absorption terms has been assumed for the investigation of the  $r$ -process in the neutrino wind of a protoneutron star [120, 138]; and the cases where emission terms dominate or where the neutrinos are in thermal equilibrium have been analysed in a study of gamma-ray burst fireballs [11]. The balance between the four reactions in Eq. (3.14) is determined by the ratio of the neutron and proton number densities and the exponential  $\exp(\beta[E \pm Q \mp \mu_e])$ . Its energy integral depends on a competition between the neutrino energy,  $E$  (in NC and AC populated according to the neutrino distribution functions  $f$ ), the mass difference between neutrons and protons,  $Q$ , and the electron chemical potential,  $\mu_e$ . Depending on the conditions, any one of these three quantities can assume a dominant influence on the balance in above reactions.

For neutrinos at high energies compared to  $|Q - \mu_e|$  the term  $\exp(\beta E)$  is large and the neutrino absorption terms,  $NC$  and  $AC$  in Eq. (3.14), dominate over neutrino emission. Hence, if the abundance of these high energy neutrinos is large, the equilibrium  $Y_e$  is determined by the balance between neutrino and antineutrino absorption and therefore dependent on the unknown neutrino distribution functions. The rate of change of  $Y_e$  is given by

$$\frac{dY_e}{dt} \approx \lambda_{\nu_e n} - Y_e(\lambda_{\nu_e n} + \lambda_{\bar{\nu}_e p}). \quad (3.15)$$

Using Eqs. (64a) and (64b) of [120] for  $\lambda_{\nu_e n}$  and  $\lambda_{\bar{\nu}_e p}$  and using the fact that neutrino and antineutrino luminosities are similar (upper right panel of Figure 4.1) it can be shown that  $Y_e > 0.5$  is achieved provided that  $4(m_n - m_p) > (\varepsilon_{\bar{\nu}} - \varepsilon_{\nu})$  (see also Fig. 5 in [120] and the discussion in §3 of [66]).

However, at earlier time, and as long as the eventual ejecta are close to the neutron star, all four reactions in Eq. (3.14) are active and the neutrino distribution functions are nontrivial functions of the accretion rate, the distance from the neutrinospheres, and the local weak interactions. Changes in the electron fraction are not only determined by the local neutrino fluxes and spectra, but also by the ability of the matter to accept captured electrons or neutrinos at the given conditions. Especially, when the electrons are degenerate the electron chemical potential can dominate the exponential for average neutrino energies. In this case,  $\exp(\beta(E + Q - \mu_e))$  in Eq. (3.14) is small and  $\exp(\beta(E - Q + \mu_e))$  becomes large. Hence, neutrino absorption,  $NC$ , and positron capture,  $PC$ , are suppressed and the electron fraction decreases because of more prolific electron captures and antineutrino absorptions. Balance is only established when the ratio between proton and neutron number densities has sufficiently decreased to compensate for the suppression of  $NC$  and  $PC$  introduced by the exponential. This leads to  $n_p < n_n$  and an equilibrium electron fraction  $Y_e < 0.5$ .

Finally, in a plasma with nondegenerate electrons, the electron chemical potential becomes rather small so that the neutron to proton mass difference,  $Q$ , may actually dominate the exponentials in the balance equations, making  $\exp(\beta(E + Q - \mu_e))$  in Eq. (3.14) larger and  $\exp(\beta(E - Q + \mu_e))$  smaller. Reversing the trend under degenerate conditions,  $NC$  and  $PC$  are favored and  $n_p > n_n$  is assumed in equilibrium. For similar neutrino and antineutrino fluxes and spectra after shock break-out, equilibrium will establish at  $Y_e > 0.5$ . According to the analytical investigation in [11] for the  $EC$  and  $PC$  reactions, this situation will occur if the electron chemical potential fulfills the condition  $\mu_e < Q/2$ . The larger binding energy favors protons over neutrons. High electron fractions just below  $Y_e = 0.5$  have been predicted for supernova explosions [56, 136]. But recent supernova simulations with accurate neutrino transport have even exceeded the estimates, consistently finding values of  $Y_e > 0.5$  in the vicinity of the mass cut in explosion settings [21, 48, 75, 93, 118, 137].

### 3.2.3 The Electron Fraction

In the following discussion, we trace a mass element in the exemplary run A40. We choose a mass element that is  $0.005 M_{\odot}$  outside of the mass cut. The trajectory of this mass element is represented in Figure 3.1a by a dotted line: At first, the element is falling into the gravitational potential. After 200 ms it passes through the accretion shock at about 300 km radius and is instantaneously decelerated. A second phase of drifting around in the heating region follows until about 400 ms after bounce. Finally, the mass element is ejected to larger radii.

Figure 3.1b illustrates important energy scales along the trajectory. The dashed and dash-dotted thick lines at the top of the graph indicate the neutrino temperature for the electron neutrinos and antineutrinos respectively. They show a rising trend in the first half of the graph. This is because

the protoneutron star shrinks and the neutrinospheres become hotter as they shift deeper into the gravitational well. The discontinuity at the crossing of the shock front stems from the Doppler shift when the mass element crosses the velocity jump at the accretion front. The change of the rise into a decline around  $t = 350$  ms after bounce is due to the decrease of the accretion rate after the launch of the explosion. Neutrino temperatures resume rising at a very small accretion rate after  $t = 450$  ms.

With the full neutrino spectrum and abundances from the simulation and with the matter density as input, we calculate the equilibrium matter temperature along the trajectory according to Eq. (3.13) by requiring  $de/dt = 0$ . For consistency with the simulation, we have also included the charged current reactions with nuclei according to the simple model described in [18]. The dotted line in Figure 3.1b shows the equilibrium temperature of matter subject to the neutrino luminosities (the neutrinos themselves are not in thermal equilibrium with matter, their temperature is set in the vicinity of the neutrinospheres where the matter temperature is higher). The lower part of Figure 3.1b shows the matter temperature (thick solid line) and the electron chemical potential (thin solid line). The electrons are degenerate in the cool infalling matter. The first little blip in the trajectory after  $t = 200$  ms is due to the burning of the initial silicon layer to nuclear statistical equilibrium. It causes a slight rise in the temperature and decline in the electron chemical potential. The pronounced step up in both quantities is due to shock compression when the mass element hits the accretion front. During the drift in the heating region, we note a temperature increase towards temperature balance (dotted line) by neutrino heating. The onset of the explosion during this time also leads to an expansion and drop in matter density. Both effects work together to lift the electron degeneracy shortly before 300 ms after bounce (crossing of temperature and electron chemical potential lines). The evolution during the third phase (ejection) is characterised by a density decrease. The weak interaction rates decrease and the temperature declines due to adiabatic expansion. The electrons stay nondegenerate and the electron chemical potential remains smaller than the neutron to proton mass difference (dashed thin line). In contrast to the electron-degenerate conditions found in past supernova simulations that fail to explode, the expanding hot plasma under neutrino irradiation favors electron fractions that exceed 0.5 as discussed in section 3.2.2.

The lower part in Figure 3.1d shows the neutrino and antineutrino abundances with dashed and dash-dotted lines respectively. The variations are due to density changes rather than luminosity variations. The upper part of Figure 3.1d shows the electron fraction from the simulation (thick solid line) and the equilibrium value determined by Eq. (3.12) (dotted line). The dash-dotted line in Figure 3.1a shows the reaction timescale as a function of radius. The upper branch belongs to infall, the lower branch to the ejection. Outside a radius of 600 km the reaction timescale is much larger than the dynamical timescale; during the drift phase of our mass element in the heating region it assumes values around 50 ms. Thus, the low electron fraction during infall is mainly set by the progenitor model. Before the shock front is crossed by the mass trajectory, the equilibrium  $Y_e$  is also low because many neutrons are bound in nuclei and not available as targets for antineutrino absorption. After the shock transition, matter is dissociated and higher electron fractions are favored. At first sight, the equilibrium electron fraction appears higher than expected at the given electron degeneracy. The reason is that neutrino absorption rates that are larger by an order of magnitude than the neutrino emission rates at these moderate temperatures. The thin solid line shows the high electron fraction equilibrium as it would evolve if only neutrino absorption were considered. The emission reactions alone favor a much lower equilibrium  $Y_e$  (thin dashed line) because there are only few positrons to capture under degenerate conditions. With the following rise of the temperature, however, the neutrino emission reactions (e.g. electron capture) gain weight with respect to the absorption reactions and the equilibrium  $Y_e$  correspondingly adjusts to lower values in the time window between  $t = 235 - 275$  ms. But as the electron degeneracy is lifted with further temperature increase and expansion, and the electron chemical potential dips below half the neutron to proton mass difference, the emission rates start to join the absorption rates in favoring higher electron fractions (steep rise of the thin dashed line). The equilibrium  $Y_e$  increases again. The descent at very late time is, as in the beginning, due to the reappearance of nuclei. The electron fraction in the simulation (thick solid line) can now easily be understood: At each time it evolves towards the equilibrium value for the combined reactions (dotted line) at the pace of the local reaction timescale. It freezes out when the mass element is ejected. Note that for an analytical estimate of the electron fraction in our application one would have to combine the approximations for neutrino absorption rates in Eq. (64) in [120] with the approximation for neutrino emission rates in Eqs. (9-10) in [11] and to

consider the reaction timescale in order to find the correct freeze-out value in the  $Y_e$  evolution.

We find that all simulations that lead to an explosion by neutrino heating develop a proton-rich environment around the mass cut with  $Y_e > 0.5$ . This is illustrated by the electron fraction profiles shown in Figure 3.1c. The open circles denote the final (i.e. at  $T < 2 \times 10^8$  K) electron fraction for the run A40. The mass scale is normalized to the respective mass cut. The different runs from series A show an almost identical electron fraction profile at the mass cut. The competition by the reaction and ejection timescale is not directly influenced by the different explosion parameters, i.e. the enhanced neutrino diffusion at higher densities. The electron fraction profiles of series B, however, respond to the different reaction timescales set by the explosion parameters in the heating region.

The electron fractions around and outside of  $m_{\text{cut}} + 0.1 M_{\odot}$  are still close to the progenitor values. Differences in this region stem from the different locations of the mass cuts within the progenitor composition. It is important to note that the investigated region at the mass cut is highly unstable against convection because of a large negative entropy gradient. It is likely that the discrepancies in  $Y_e$  are heavily mixed on a dynamical timescale [80]. We expect, however, that the  $Y_e$  remains high in an averaged sense [see also 118]. Moreover, matter blobs that leave the heating region in an environment of large convective turnover may still show qualitatively similar features in comparison with our spherically symmetric shells, because the high electron fraction in the neutrino field is enabled by the discussed general features of expanding hot matter. We believe that the dependence on the details of our different simulations is small.

# 4

---

## Nucleosynthesis

---

### 4.1. Introduction

The nucleosynthesis results presented in this thesis are calculated in a post-processing framework. In a first step, the full hydrodynamical simulation is carried out including a reduced network of  $\alpha$ -nuclei for the energy generation due to nuclear burning. For a complete description of the hydrodynamical calculations refer to Section 3.2. Then, based on the temperature-density profiles of all matter in our hydrodynamical simulations the detailed nucleosynthesis is calculated for the temperature range  $T \geq 2 \times 10^8$  K. The extended nuclear reaction network consists of 1160 nuclei with  $Z \leq 46$  and neutrons (see Table 4.1 for a complete list).

The neutral and charged particle reactions are taken from a recent REACLIB compilation (see Section 3.1.1). Weak interaction rates (electron and positron captures and  $\beta$ -decays are taken from [53, 54] for the *sd*-shell nuclei and from [85] for *pf*-shell nuclei. As a first, rates for neutrino and antineutrino captures on free nucleons and on nuclei are included consistently in the network calculations. The meaning of consistent in this context is explained in Section 3.1.2 where the details of the treatment for neutrino-induced reactions is given. Hence, all weak interactions responsible for changes of  $Y_e$  are taken into account in the reaction network, namely: neutrino/antineutrino capture on free neutrons and protons, neutrino/antineutrino capture on nuclei, electron/positron capture, and  $\beta^-/\beta^+$  decays. Neutrino scattering processes do not contribute to abundance changes and are thus not included in the reaction network used for post-processing. Nevertheless, neutrino-induced spallation reactions can change the final abundances of some nuclei and we will investigate this in future calculations.

As explained in Section 1.2.1 the location of the mass cut is essential to the final Fe-group ejecta. In nucleosynthesis calculations based on induced explosions (via a thermal bomb or a piston) the location of the mass cut is a free parameter which has to be constrained from observational data (like the light curve powered by the decay chain of  $^{56}\text{Ni} - ^{56}\text{Co} - ^{56}\text{Fe}$ ). The nucleosynthesis calculations in this thesis are based on hydrodynamical simulations in which the position of the mass cut emerges consistently from the simulation as the region of bifurcation in which the density has dropped below  $\sim 10^6$  g/cm<sup>3</sup>. This allows a prediction for the total amount of Fe(group) nuclei ejected.

This Chapter is organized as follows. First, the effect of neutrinos on the innermost ejecta from core collapse supernova models with accurate neutrino transport is presented. The different approaches to induce explosions will be compared in the context of nucleosynthesis. Then the Fe-group ejecta will be discussed based on abundances from the models of this thesis for the innermost ejecta combined with abundances from TNH96. The third part of this Chapter is devoted to a new nucleosynthesis process, the  $\nu p$ -process. To conclude the Chapter, nucleosynthesis results for a new  $20 M_{\odot}$  model at solar metallicity are shown.

---

### 4.2. The Innermost Ejecta

In this Section, the innermost ejecta (just outside of the mass cut) enclosing a few hundredths of a solar mass where values of  $Y_e$  higher than 0.5 are achieved are discussed. An exemplary model is used to analyze the individual contributions from different reactions to the final electron fraction of  $Y_e > 0.5$ . The resulting effects on the nucleosynthesis in this zone are presented.

Element	Mass Range	Element	Mass Range	Element	Mass Range
n	1	H	1–3	He	3–6
Li	6–9	Be	7–12	B	8–14
C	9–18	N	11–21	O	13–22
F	16–26	Ne	17–34	Na	17–40
Mg	20–38	Al	21–40	Si	22–44
P	23–44	S	24–48	Cl	26–50
Ar	27–52	K	29–54	Ca	30–58
Sc	32–60	Ti	34–64	V	36–66
Cr	38–68	Mn	40–70	Fe	42–72
Co	44–72	Ni	46–74	Cu	48–77
Zn	51–80	Ga	53–84	Ge	55–84
As	57–88	Se	59–90	Br	61–94
Kr	63–98	Rb	66–102	Sr	68–100
Y	70–104	Zr	72–106	Nb	74–106
Mo	77–108	Tc	79–110	Ru	81–114
Rh	83–113	Pd	86–120		

**Table 4.1:** Nuclear species used in nuclear reaction network for post-processing. The mass range given indicates for each element the nuclei with the minimum and maximum neutron number.

#### 4.2.1 The Effect of Neutrinos

An important feature of all our models is the region just outside of the mass cut (located at  $1.503 M_{\odot}$  in this model) where the electron fraction reaches values as high as 0.56. The dominant processes in changing the electron fraction during the early phases of the explosion are neutrino absorption reactions on neutrons and on protons as well as electron and positron captures reactions on free neutrons and protons:

$$\frac{dY_e}{dt} = \lambda_{\nu_e n} + \lambda_{e+n} - (\lambda_{\nu_e n} + \lambda_{e+n} + \lambda_{\bar{\nu}_e p} + \lambda_{e-p})Y_e \quad (4.1)$$

where the  $\lambda$ 's are the rates for the reactions:



The final  $Y_e$  in the ejecta is mainly set by the neutrino and antineutrino capture reactions and therefore the properties of the  $\nu_e$  and  $\bar{\nu}_e$  fluxes [120]. For the following discussion we therefore neglect electron and positron captures. The change of  $Y_e$  is then given by:

$$\frac{dY_e}{dt} = \lambda_{\nu_e n} - Y_e(\lambda_{\nu_e n} + \lambda_{\bar{\nu}_e p}). \quad (4.3)$$

The rates for neutrino and antineutrino captures at  $r \gg R_{\nu}$  can be written as [120]:

$$\lambda_{\nu_e n} \approx \frac{L_{\nu_e}}{r^2} \sigma_0 \left( \epsilon_{\nu_e} + 2\Delta + \frac{\Delta^2}{\epsilon_{\nu_e}} \right) \quad (4.4)$$

and

$$\lambda_{\bar{\nu}_e p} \approx \frac{L_{\bar{\nu}_e}}{r^2} \sigma_0 \left( \epsilon_{\bar{\nu}_e} - 2\Delta + \frac{\Delta^2}{\epsilon_{\bar{\nu}_e}} \right). \quad (4.5)$$

Here,  $\Delta = 1.293$  MeV is the neutron-proton mass difference and  $L_{\nu}$  is the neutrino luminosity. The neutrino energy  $\epsilon_{\nu}$  is defined through  $\epsilon_{\nu}^2 \equiv \langle E_{\nu}^3 \rangle / \langle E_{\nu} \rangle$  where  $\langle E_{\nu}^n \rangle$  is the  $n$ th moment of the neutrino energy distribution. Substituting the rates (Eqs. (4.4) and (4.5)) into Eq. (4.3) and assuming similar luminosities for neutrinos and antineutrinos, i.e.  $L_{\nu_e} \approx L_{\bar{\nu}_e}$ , gives:

$$\frac{dY_e}{dt} = \frac{L_{\nu}}{r^2} \sigma_0 \left\{ \epsilon_{\nu_e} + 2\Delta + \frac{\Delta^2}{\epsilon_{\nu_e}} - Y_e(\epsilon_{\nu_e} + \epsilon_{\bar{\nu}_e}) + \Delta^2 Y_e \left( \frac{1}{\epsilon_{\nu_e}} + \frac{1}{\epsilon_{\bar{\nu}_e}} \right) \right\}. \quad (4.6)$$



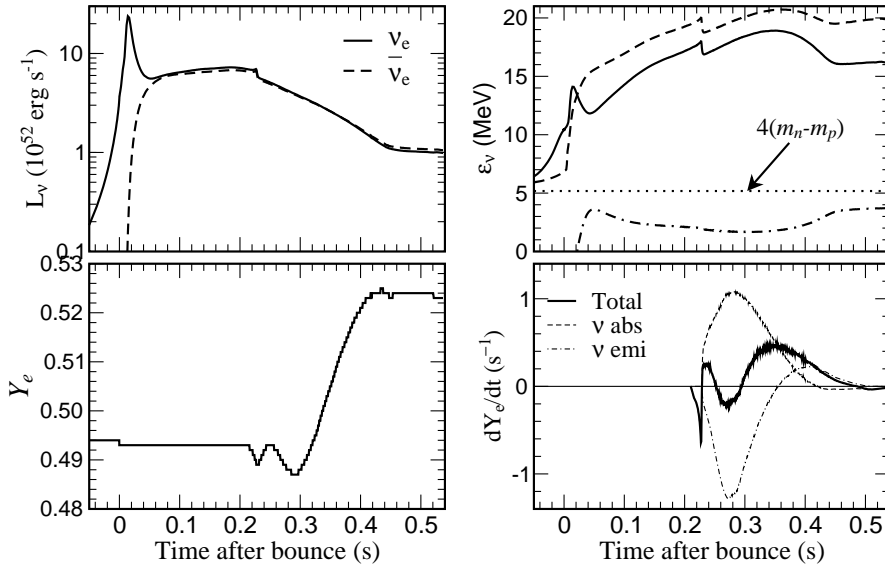


**Figure 4.1:** Time evolution after core bounce of an ejected layer at  $0.005 M_\odot$  outside of the mass cut from a  $20 M_\odot$  supernova progenitor. Top left: Luminosity of neutrinos and antineutrinos felt by a Lagrangian mass zone. Bottom left: Electron fraction  $Y_e$ . Top right: Average neutrino energy  $\epsilon_\nu = \langle E_\nu^2 \rangle / \langle E_\nu \rangle$  (thick solid and dashed lines). The difference in average neutrino energy,  $(\epsilon_{\bar{\nu}_e} - \epsilon_{\nu_e})$  (thick dot-dashed line) and four times the mass difference between neutron and protons (thin dashed line) are shown in the lower part. Bottom right: Individual weak interaction contributions leading to  $Y_e > 0.5$ . The individual contributions from neutrino/antineutrino captures and electron/positron captures are a factor ten larger than the total resulting  $dY_e/dt$ .

A detailed discussion of the solution of Eq. (4.6) is given in [120]. For our purpose here, we estimate the constraints to achieve  $Y_e > 0.5$ . Assuming a typical value of  $Y_e \approx 0.5$  for the initial  $Y_e$  the above expression for the change in  $Y_e$  reduces to

$$\frac{dY_e}{dt} = \frac{L_\nu}{r^2} \sigma_0 \left\{ 2\Delta - \frac{1}{2}(\epsilon_{\nu_e} + \epsilon_{\bar{\nu}_e}) + \frac{\Delta^2}{2} + \frac{\Delta^2}{2} Y_e \left( \frac{1}{\epsilon_{\nu_e}} + \frac{1}{\epsilon_{\bar{\nu}_e}} \right) \right\}. \quad (4.7)$$

Neglecting the last term in Eq. (4.7) we conclude that  $Y_e > 0.5$  will be achieved provided that  $4\Delta > \epsilon_{\bar{\nu}_e} - \epsilon_{\nu_e}$  (see upper right panel of Fig. 4.1).

An example of the influence of the individual weak interaction contributions leading to  $Y_e > 0.5$  is given in Fig. 4.1 (bottom right) for an exploratory study of one mass zone of model A40. Also shown are the neutrino luminosities  $L_\nu$  (top left) and energies  $\epsilon_\nu = \langle E_\nu^2 \rangle / \langle E_\nu \rangle$  (top right). For this exemplary mass zone it can be seen in the upper right panel of Fig. 4.1 that  $(\epsilon_{\bar{\nu}_e} - \epsilon_{\nu_e})$  is always smaller than  $4(m_n - m_p)$ . There are several phases that can be identified in Fig. 4.1 and that have been discussed in Section 3.2.2. At early times ( $t < 0.3$  s) matter is degenerate and electron capture dominates. At the same time matter is being heated by neutrino energy deposition and around  $t \approx 0.3$  s the degeneracy is lifted (see upper panel of Fig. 4.1). At this time, the ratio between electron captures and positron captures significantly decreases and neutrino absorption reactions start to dominate the change of  $Y_e$  and, as discussed before, the average neutrino energies favor  $Y_e > 0.5$ . As the matter expands the density decreases, reducing the electron chemical potential. This results in positron captures dominating electron captures beginning around  $t \approx 0.3$  s. From this time, the combined effect of positron capture and  $\nu_e$  absorption contributes to the final increase of  $Y_e$ .

The time evolution of the hydrodynamical quantities relevant to nucleosynthesis for a representative layer of models A40 (scattering cross sections on nucleons reduced by 40%) for the whole computational time are depicted in Fig. 4.2. The entropy and electron fraction rise to their final value shortly after the maximum in temperature is reached. The temperature range relevant for nucleosynthesis in such proton-rich environments is between  $T_9 = 2$  and  $T_9 \approx 0.8$ . For this layer, the cooling from  $T_9 = 2$

to  $T_9 = 0.8$  takes about 6 s. The final decline in the electron fraction  $Y_e$  is due to  $\beta$ -decays of the nucleosynthesis products.

Figure 4.3 shows the abundances after decay to stability of all nuclei for model A40 integrated over mass zones with  $Y_e > 0.5$ , including in total  $\sim 0.02 M_\odot$ . For these mass zones, we are only concerned with the Fe-group composition. In Fig. 4.4 integrated abundances after decay to stability are presented for model B07. In this model, the zones with  $Y_e > 0.5$  enclose  $\sim 0.036 M_\odot$ . The positions of the mass cut and the explosion energies for both models are given in Table 3.5. Note that unlike earlier supernova nucleosynthesis simulations, nuclei beyond  $A = 64$  are also produced in appreciable amounts, ranging in fact up to  $A = 80$  or even beyond, due to neutrino interactions with matter during the whole period of explosive processing. This is due to the  $\nu p$ -process to which Section 4.4 is devoted.

### 4.2.2 Comparison of Model A40 and B07

The models of series A and series B differ in the manner in which the neutrino interactions were modified in order to produce an explosion. In series A, the neutral current neutrino scattering opacities are scaled with a factor ranging from 0.1 to 0.7. This treatment leads to a faster deleptonization of the protoneutron star which in turn boosts the neutrino luminosities in the heating region. However, only the neutrino propagation properties are affected. The timescales for reaction and for ejection are not modified by the scaling of the neutral current neutrino opacities. This is underlined by the comparison of different models of series A. Although the parameter for scaling the neutrino opacities covers the whole parameter range all the models show an almost identical electron fraction profile when normalized to the respective mass cut (see Fig. 3.1, panel (c)).

In series B, the neutrino/antineutrino capture reactions and their inverse reactions (electron/positron captures) are enhanced by a constant factor equal for both directions of the reactions. The factor ranges from 1 to 10, however at least a factor of 5 is needed to obtain a barely exploding model. In addition to the different treatment of causing explosions, series B also includes weak magnetism corrections to the neutrino cross sections [69]. Since this effect has opposite sign for neutrinos and antineutrinos it further helps to drive the electron fraction to higher values. The treatment used to cause explosions in this series changes the timescales for neutrino heating. However, the equilibrium  $Y_e$  and temperature remain unaltered. Different models of series B therefore have different heating timescales and resulting  $Y_e$  profiles (again, see Fig. 3.1c). In general, the models of series B achieve larger  $Y_e$ -values than the models of series A.

The general features of the explosive nucleosynthesis in zones with electron fraction above 0.5 are the same for comparable models from series A and from series B (model A40 and B07). In both models, the innermost ejecta is proton-rich and shows enhanced synthesis of elements beyond mass number 64 (see Figs. 4.3 and 4.4). However, as explained above, model B07 shows larger  $Y_e$  than A40 in the innermost ejecta and therefore in this model matter is subject to a larger neutrino exposure. This makes the effect of neutrino-induced reactions stronger at a given location outside of the mass cut and more matter experiences a given neutrino flux. In total, this results in an enhancement of the effect of neutrinos on the nucleosynthesis, especially on the production of elements with  $A > 64$ . The details of how neutrinos contribute to the synthesis of these elements is deferred to Section 4.4.

## 4.3. Iron Group Nucleosynthesis

Core collapse supernovae eject large amounts of  $\alpha$ -elements (of the order of  $\sim 1 M_\odot$ ) and smaller amounts of Fe and Fe-group elements (about a tenth of a solar mass). The Fe-group elements originate from the innermost ejecta and are most sensitive to the explosion mechanism (and the location of the mass cut if it doesn't emerge from the simulations). In this Section the Fe-group ejecta of core collapse models with detailed neutrinos transport are analyzed with respect to their role of the neutrinos and the final abundances.

As noted in the previous Section, the innermost ejecta in these models also contributes to the synthesis of nuclei beyond iron — unlike earlier supernova nucleosynthesis simulations. These nuclei and the Fe-group nuclei are mainly produced in the zones close to the mass cut where the electron fraction depends strongly on neutrino captures. For these mass zones relatively high entropies are

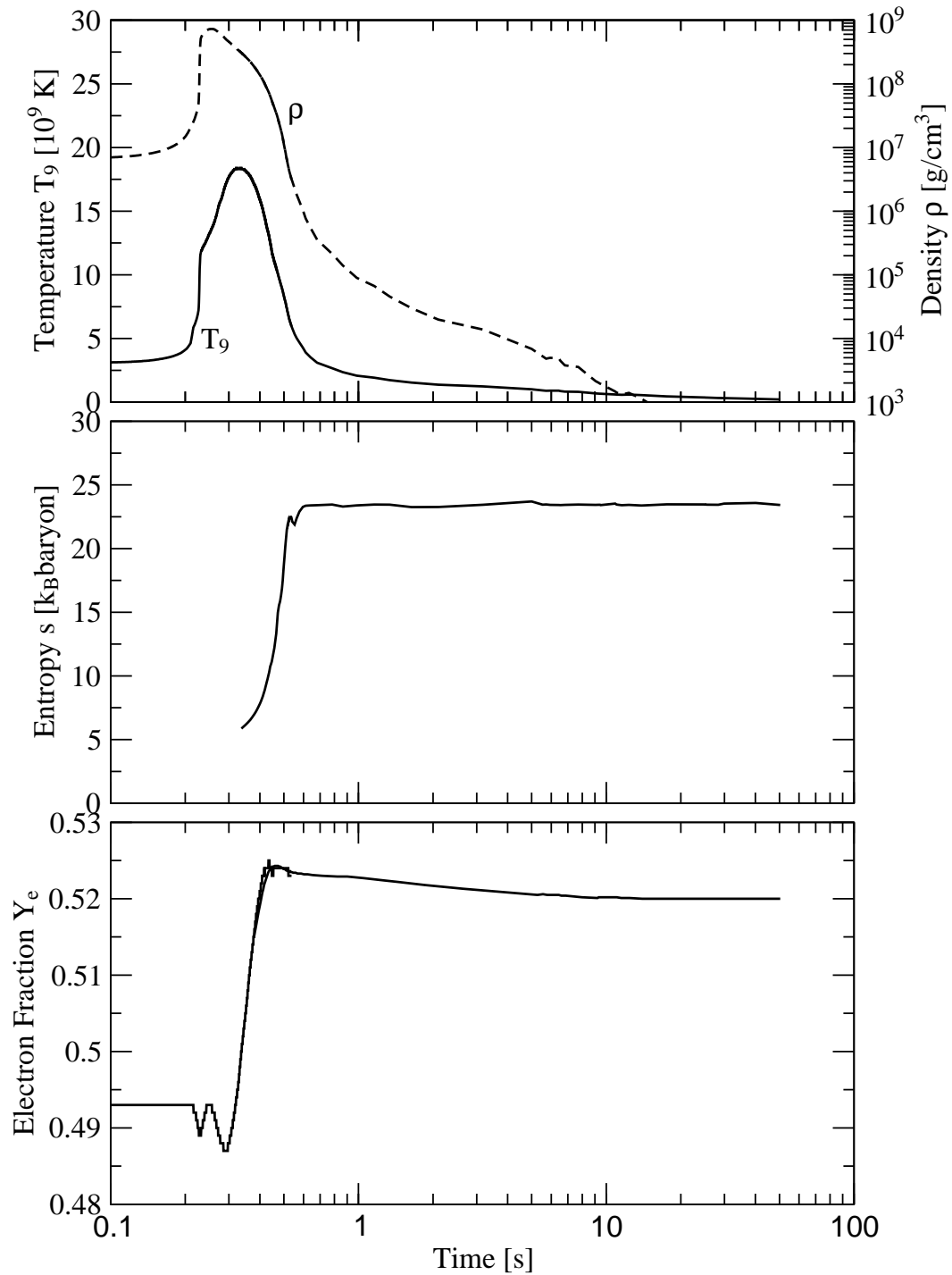


**Figure 4.2:** Evolution after core bounce for a representative ejected layer at  $0.005 M_{\odot}$  outside of the mass cut for model A40. For this layer the time for cooling from  $T_9 = 2$  to  $T_9 = 0.8$  is about 6 s. Top: Temperature (solid line) and density (dashed line) evolution. Middle: Entropy  $s$  per baryon in units of the Boltzmann constant. Bottom: Electron fraction  $Y_e$ . The final decline is due to  $\beta$ -decays of the nucleosynthesis products.

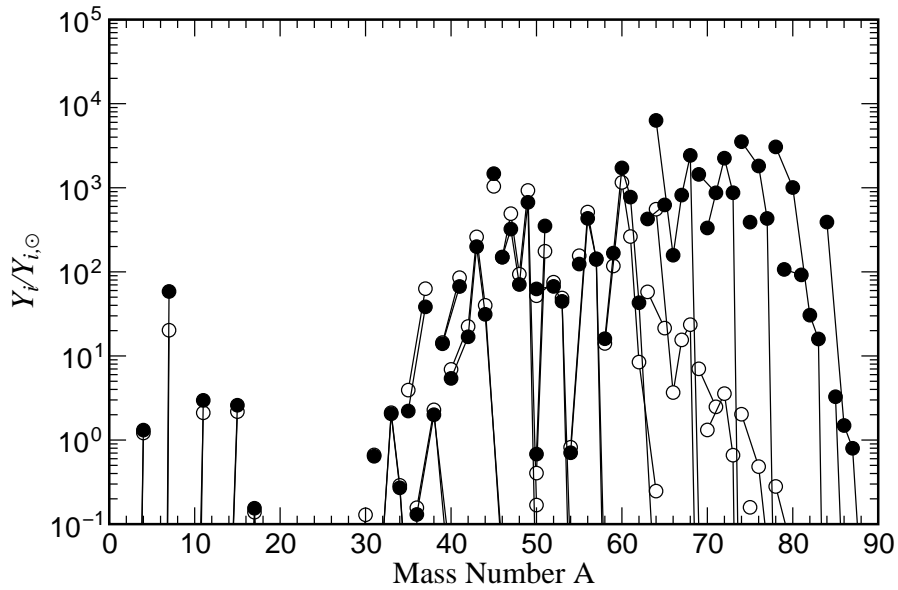


**Figure 4.3:** Abundances for model A40 relative to solar abundances [94]. Two different calculations are shown: with neutrino-induced reactions in the network (filled circles) and without neutrino-induced reactions in the network (open circles).

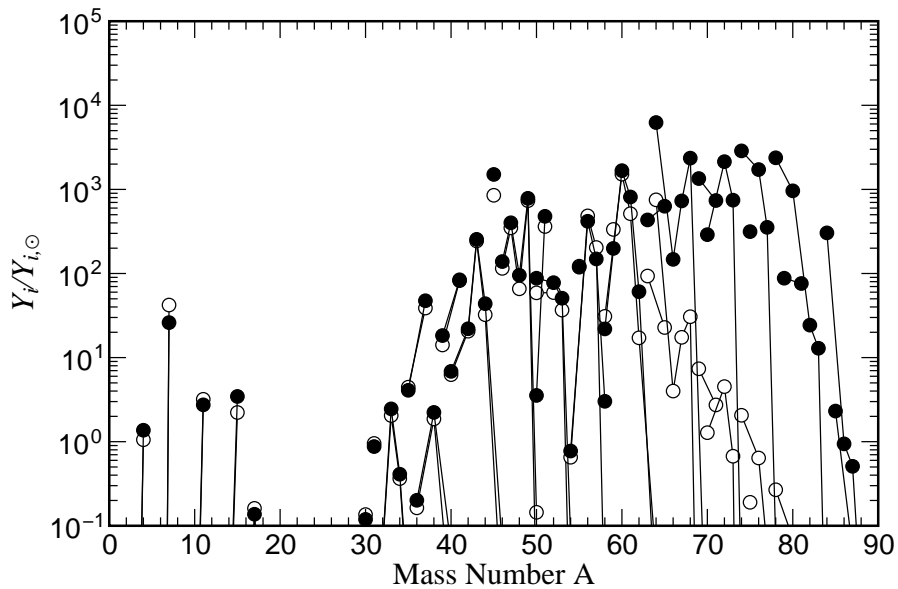


**Figure 4.4:** Abundances for model B07 relative to solar abundances [94]. Two different calculations are shown: with neutrino-induced reactions in the network (filled circles) and without neutrino-induced reactions in the network (open circles).

attained:  $s/k_b \sim 30\text{--}51$ . In nucleosynthesis terms this corresponds to complete explosive Si-burning with a strong alpha-rich freeze-out which also leaves a finite proton abundance ( $0.0007M_\odot$ ) due to  $Y_e$  being larger than 0.5. The high proton abundance permits the onset of an rp-process which, however, does not proceed too far in  $A$  as (due to the high entropies) the densities are too small. The abundances result from the accumulation of matter at the waiting-point nuclei  $^{64}\text{Ge}$ ,  $^{68}\text{Se}$ ,  $^{72}\text{Kr}$ ,  $^{76}\text{Sr}$ . After decay to stability they produce the high abundances of  $^{64}\text{Zn}$ ,  $^{68}\text{Zn}$ ,  $^{72}\text{Ge}$ , and  $^{76}\text{Se}$ . A relatively high abundance of  $^{78}\text{Kr}$  is also obtained.  $^{78}\text{Kr}$  is considered to be produced by the p- or  $\gamma$ -process in the ONe layers of the star. Chemical evolution studies [e.g. 140] underproduce  $^{64}\text{Zn}$  by about a factor 5. A possible site for the production of  $^{64}\text{Zn}$  is the modest early-time neutrino-driven wind occurring after core bounce in supernovae [154]. The authors of [143] have found that the  $^{64}\text{Zn}/^{56}\text{Fe}$  ratio is enhanced *if*  $Y_e$  is close to 0.5 and the explosion energy is as high as  $\sim 10^{52}$  erg. Our proton-rich environment constitutes an alternative or complementary production site.

For the intermediate mass elements the main improvement compared to earlier calculations is the higher production of individual nuclei like  $^{45}\text{Sc}$  and  $^{49}\text{Ti}$ . Scandium is mainly produced by the  $\beta^+$ -decays originating from  $^{45}\text{Cr}$  and  $^{45}\text{V}$  decaying via  $^{45}\text{Ti}$  to  $^{45}\text{Sc}$ . Different calculations of abundance yields (TNH96, [157],[30]) fail to predict the observed abundance of scandium [29, 57]. Our calculations show that Sc can be consistently produced with iron in the inner regions of the supernova where  $Y_e$  is higher than 0.5. The ejected yield of Sc is  $10^{-6} M_\odot$  which is a factor of 10 larger than the value obtained for a similar star by TNH96. If we assume that our total production of Fe is similar to the one obtained in TNH96 our Sc yield will be consistent with observations.  $^{49}\text{Ti}$  is underproduced by a factor 5 in the chemical evolution studies of [140]. The nucleus  $^{49}\text{Ti}$  originates from the decay chain of  $^{49}\text{Mn}$  which decays via  $^{49}\text{Cr}$  and  $^{49}\text{V}$  to  $^{49}\text{Ti}$ . After decay to stability, the resulting yield of  $^{49}\text{Ti}$  is  $\sim 5 \times 10^{-6} M_\odot$ . We find that the origin of the differences in nucleosynthesis yields is a consequence of an electron fraction above 0.5 which is due to a consistent treatment of all weak interaction processes on free nucleons. The obtained  $Y_e$  values are not sensitive to the inclusion of neutrino and antineutrino captures on nuclei.

For a first exploratory investigation covering the entire region responsible for Fe-group production we combine our abundances with the results of TNH96. The two calculations are combined in such a way that the resulting amount of Fe-group elements is the same as in this earlier work. For the inner zones, where neutrino and antineutrino capture reactions play an important role, the results of the present calculation are used. They constitute about 30% of the total production of Fe-group elements. For the other zones where neutrino/antineutrino captures do not have significant influence on the final  $Y_e$  we use the abundance results from TNH96. This procedure allows us to estimate the influence of a consistent treatment of weak interaction processes on the total production of Fe-group elements. To further solidify these results full nucleosynthesis calculations are being performed based on the exploding models.

The effect of neutrino-induced reactions on the total Fe-group ejecta is clearly seen in Fig. 4.5 for model A40 (left panel) and B07 (right panel). The isotopic abundances presented here stem from combining the innermost ejecta with  $Y_e > 0.5$  of the models A40 and B07 with abundance results from TNH96, as described above. The scatter seen for  $A > 64$  in Fig. 4.5 is in agreement with the large scatter seen in  $[\text{Sr}/\text{Fe}]$  at low metallicities [141].

Figure 4.6 shows elemental abundances of two calculations compared to two sets of observational data. One set of observational data [57] originates from a sample of stars with  $-2.7 < [\text{Fe}/\text{H}] < -0.8$ , relevant for the average type II supernova contribution. The second set of observational data represents a sample of extremely metal-poor stars [29]. The nucleosynthesis results for model A40 (corresponding to the left panel in Fig. 4.5) of this work are shown in combination with the results of the earlier calculation as explained above (the results for model B07 (right panel in Fig. 4.5) are very similar with the exception of Zn and heavier nuclei). For comparison, the theoretical prediction by TNH96 is also shown. We clearly see an improvement for Sc and the heavy elements Cu and Zn.

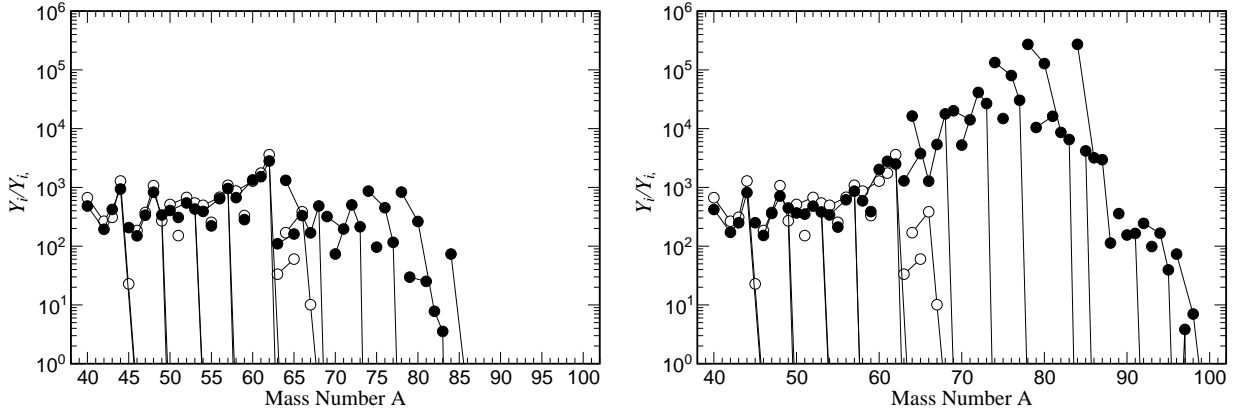


**Figure 4.5:** *Left panel:* Combined abundances of this work (model A40) and TNH96. The open circles are the combined abundances and the filled circles are the original abundances of the above reference. For details see text. *Right panel:* The same as in the left panel but for model B07.

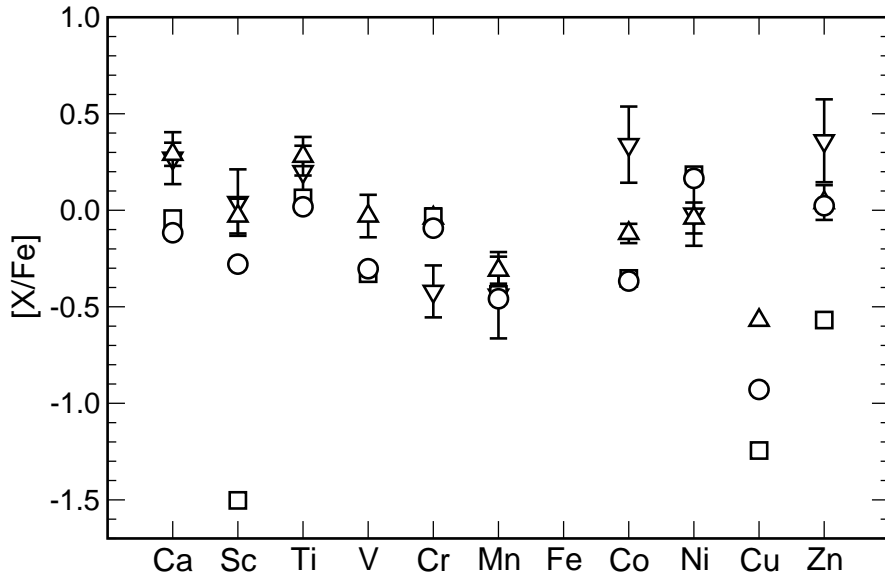


**Figure 4.6:** Comparison of elemental overabundance in the mass range Ca to Zn for different calculations. The triangles with error bars represent observational data. The triangles facing upwards [57] originate from an analysis of stars with  $-2.7 < [Fe/H] < -0.8$ . The triangles facing downwards [29] is data for a sample of extremely metal poor stars ( $-4.1 < [Fe/H] < -2.7$ ). The circles are abundances of this work combined with the work of TNH96 to obtain the same amount of Fe-group elements. The squares show the pure abundances of the previous reference.

## 4.4. The $\nu p$ -Process

In this Section I will present a new nucleosynthesis process, the  $\nu p$ -process, which occurs in all core collapse supernovae. The  $\nu p$ -process is primary and is associated with explosive scenarios where proton-rich matter is ejected under the influence of strong neutrino fluxes. It could explain the existence of Sr and other elements beyond Fe in the very early stage of galactic evolution, thus being a candidate for the postulated lighter element primary process LEPP[141] which seems independent of the heavy r-process abundance pattern. It can also contribute to the nucleosynthesis of light  $p$ -process nuclei. The material presented here is published [50].

First, the open issues are presented. After a brief intermezzo on other types of neutrino-induced nucleosynthesis processes the focus will be directed to the  $\nu p$ -process. The mechanism will be explained, followed by a discussion of the sensitivity of the process. The Section concludes with linking the  $\nu p$ -process to observations.

### 4.4.1 Open Questions

Supernova explosions produce iron, underlined by the lightcurves powered by radioactive decay of  $^{56}\text{Ni}$ . The production of elements beyond Fe has long been postulated by three classical processes, the r- and the s-process (caused by rapid or slow neutron capture) and the p-process, standing either for proton capture or alternative means to produce heavy neutron deficient, stable isotopes[23, 146]. The s-process acts during stellar evolution via neutron captures on Fe produced in previous stellar generations (thus being a “secondary process”). The location and/or *operation and uniqueness* of the r- and p-process in astrophysical sites is still a subject of debate. Most of the p-nuclei are thought to be produced in hot (supernova) environments, via the disintegration of pre-existing heavy elements due to black-body radiation photons (also being a secondary process). The r-process is required to be a primary process in stellar explosions. Primary here means that the production of such elements is independent of the initial heavy element content in the star.

Observations of extremely “metal-poor” stars in the Milky Way provide us with information about the nucleosynthesis processes operating at the earliest times in the evolution of our Galaxy. They are thus probing the earliest supernova events from massive stars, the fastest evolving stellar species. Such events are in all cases observed to produce Fe. The recently discovered hyper-metal-poor stars in the Milky Way [32, 47] with large C/Fe ratios witness chemical enrichment by the first generation of faint massive supernovae which experience extensive matter mixing (due to instabilities) and fallback of matter after the explosion [73]. However, the detection of Sr/Fe, exceeding 10 times the solar ratio in the most metal-poor star known to date ( $[\text{Fe}/\text{H}] = -5.4 \pm 0.2$ ) [47] suggests the existence of a primary process, producing elements beyond Fe and Zn. Recent galactic chemical evolution studies of Sr, Y, and Zr [141] also suggest the existence of a *primary process* denoted “lighter element primary process” (LEPP), operating very early in the Galaxy and being independent of the r-process [39, 127].

There exist also problems to account for the correct amount of the light p-elements with mass numbers  $A < 100$ . Currently, the precise mechanism for the production of the light  $p$ -nuclei,  $^{92,94}\text{Mo}$  and  $^{96,98}\text{Ru}$ , is unknown. The “ $p$ -process”, occurring in supernovae of a second generation and acting upon pre-existing heavy nuclei, accounts for the heavy  $p$ -nuclei but underproduces the light ones (see e.g. ref.[6, 37, 60]). These shortcomings are strengthened by the chemical evolution studies of the cosmochronometer nucleus  $^{92}\text{Nb}$ [41] – a light  $p$ -nucleus shielded from the decay of other  $p$ -nuclei – which underline the need for a supernova origin and thus represent a problem to present supernova models.

Here, we consider only the inner ejecta of core-collapse supernovae, but the winds from the accretion disk in the collapsar model of gamma-ray bursts [52, 117, 129] may also be a relevant site for the  $\nu p$ -process. In the studies presented here the detailed neutrino spectral information provided by neutrino radiation hydrodynamical calculations [49] are used to determine the neutrino and antineutrino absorption rates at each point of the nucleosynthesis trajectory (temperature, density and radius). Our network calculations follow the detailed abundances of 1435 isotopes between  $Z = 1$  and  $Z = 54$  plus neutrons, which allows an accurate treatment of the changes in composition induced by neutrino interactions. The discussion below includes only the innermost proton-rich supernova ejecta before the emergence of the neutrino-wind from the proto-neutron star. This neutrino-wind will initially be

proton-rich [118] but will turn neutron-rich in its later phases allowing for the synthesis of r-process nuclei [56, 66, 98].

#### 4.4.2 Intermezzo: Neutrino-Induced Nucleosynthesis

This very short Section diverts from the main line of argument concerning the mechanism of operation and sensitivity of the  $\nu p$ -process. However, it is important to distinguish between various types of “neutrino nucleosynthesis”. The process discussed in this Section is distinct from previous nucleosynthesis processes involving neutrinos. Previous neutrino-induced nucleosynthesis processes are briefly mentioned in order to clarify the novel aspects of the  $\nu p$ -process.

Neutrino-induced nucleosynthesis has been suggested since the 1970s. The neutrino process, involving neutrino-induced spallation of nucleons, has been discussed [42, 43, 152] for the production of some nuclei like  ${}^7\text{Li}$ ,  ${}^{11}\text{B}$ ,  ${}^{19}\text{F}$ ,  ${}^{138}\text{La}$ , and  ${}^{180}\text{Ta}$ . Although these spallation reactions occur very rarely (on only about 1% of the nuclei) this still is a dominant production process for rare nuclei which are one mass unit below abundant nuclei such as C, O, or Ne. It also has been suggested that antineutrino absorption on protons as a source of neutrons for the production of light nuclei up to Li [42]. Finally, the production of light  $p$ -nuclei by neutrino absorption on nuclei in alpha-rich freezeouts from the neutron-rich neutrino wind that develops in later phases of a supernova explosion is discussed in [56, 66].

#### 4.4.3 The Mechanism

As a full understanding of the core collapse supernova mechanism is still pending and successful explosion simulations are difficult to obtain [22], the composition of the innermost ejecta – directly linked to the explosion mechanism – remained to a large extent unexplored. Recent supernova simulations with accurate neutrino transport [22, 93, 137] show the presence of proton-rich neutrino-heated matter, both in the inner ejecta [22, 93] and in the early neutrino wind from the proto-neutron star [22]. This matter is subject to a large neutrino energy deposition by the absorption of neutrinos and antineutrinos with initially similar intensities and energy spectra. As soon as the heating and expansion lifts the electron degeneracy, the reactions  $\nu_e + n \rightleftharpoons p + e^-$  and  $\bar{\nu}_e + p \rightleftharpoons n + e^+$  drive the composition proton-rich due to the smaller mass of the proton [49, 118]. As this proton-rich matter expands and cools, nuclei can form resulting in a composition dominated by  $N = Z$  nuclei, mainly  ${}^{56}\text{Ni}$  and  ${}^4\text{He}$ , and protons. Without the further inclusion of neutrino and antineutrino reactions the composition of this matter will finally consist of protons, alpha-particles, and heavy (Fe-group) nuclei (in nucleosynthesis terms a proton- and alpha-rich freeze-out), with enhanced abundances of  ${}^{45}\text{Sc}$ ,  ${}^{49}\text{Ti}$ , and  ${}^{64}\text{Zn}$  [49, 118]. In these calculations the matter flow stops at  ${}^{64}\text{Ge}$  with a small proton capture probability and a beta-decay half-life (64 s) that is much longer than the expansion timescale ( $\sim 10$  s) [118].

Synthesis of nuclei heavier than  $A = 64$ , including light  $p$ -nuclei, is possible in proton-rich ejecta if the entropy per nucleon is in the range  $s \approx 150\text{--}170 k_B$  (where  $k_B$  is the Boltzmann constant) [78]. Such large entropies are, however, not attained in core-collapse supernovae simulations with detailed neutrino transport which give  $s \approx 50\text{--}75 k_B$  [49, 118]. However, the synthesis of nuclei with  $A > 64$  can also be obtained with realistic entropies, if one explores the previously neglected effect of neutrino interactions on the nucleosynthesis of heavy nuclei. Nuclei with  $N \sim Z$  are practically inert to neutrino capture (converting a neutron in a proton), because such reactions are endoergic for neutron-deficient nuclei located away from the valley of stability. The situation is different for antineutrinos that are captured in a typical time of a few seconds, both on protons and nuclei, at the distances at which nuclei form ( $\sim 1000$  km). This timescale is much shorter than the beta-decay half-life of the most abundant heavy nuclei reached without neutrino interactions (e.g.  ${}^{56}\text{Ni}$ ,  ${}^{64}\text{Ge}$ ). As protons are more abundant than heavy nuclei, antineutrino capture occurs predominantly on protons, causing a residual density of free neutrons of  $10^{14}\text{--}10^{15} \text{ cm}^{-3}$  for several seconds, when the temperatures are in the range 1–3 GK. This effect is clearly seen in Figure 4.7, where the time evolution of the abundances of protons, neutrons, alpha-particles and  ${}^{56}\text{Ni}$  is shown ( ${}^{56}\text{Ni}$  serves to illustrate when nuclei are formed). The dashed lines show the results for a calculation where neutrino absorptions are neglected once the temperature drops below 6 GK. Without the inclusion of antineutrino capture the neutron abundance soon becomes too small to allow for any capture on heavy nuclei. The Figure also compares the evolution of the electron fraction  $Y_e$ .



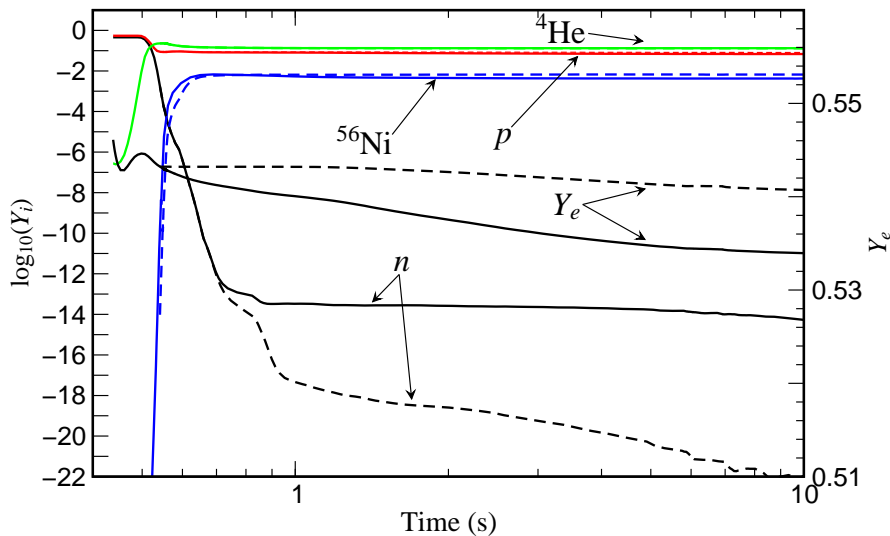


**Figure 4.7:** Evolution of the abundances of neutrons, protons, alpha-particles, and  $^{56}\text{Ni}$  in a nucleosynthesis trajectory resulting from model B07 of reference [49]. The abundance,  $Y$ , is defined as the number of nuclei of the species  $i$  present divided by the total number of nucleons which is conserved during the calculation. The solid (dashed) lines display the nucleosynthesis results which include (omit) neutrino and antineutrino absorption interactions after nuclei are formed. The abscissa measures the time since the onset of the supernova explosion.

The neutrons produced via antineutrino absorption on protons can easily be captured by neutron-deficient  $N \sim Z$  nuclei (for example  $^{64}\text{Ge}$ ), which have large neutron capture cross sections. The amount of nuclei with  $A > 64$  produced is then directly proportional to the number of antineutrinos captured. While proton capture,  $(p, \gamma)$ , on  $^{64}\text{Ge}$  takes too long, the  $(n, p)$  reaction dominates (with a lifetime of 0.25 s at a temperature of 2 GK), permitting the matter flow to continue to nuclei heavier than  $^{64}\text{Ge}$  via subsequent proton captures with freeze-out at temperatures around 1 GK. The rates for the  $(n, p)$  reaction, the  $(n, \gamma)$  reaction, and the  $\beta$ -decay of  $^{64}\text{Ge}$  are shown in Fig. 4.8 for illustration. This is different to r-process environments with  $Y_e < 0.5$ , i.e. neutron-rich ejecta, where neutrino capture on neutrons provides protons that interact mainly with the existing neutrons, producing alpha-particles and light nuclei. Their capture by heavy nuclei is suppressed because of the large Coulomb barriers [56, 98]. Consequently, in r-process studies an enhanced formation of the heaviest nuclei does not take place when neutrino interactions are included. In proton-rich ejecta, in contrast to expectation [118], antineutrino absorption produces neutrons that do not suffer from Coulomb barriers and are captured preferentially by heavy neutron-deficient nuclei.

The composition of supernova ejecta obtained with the hydrodynamical model B07 is described in detail in Section 4.3 and in [49] (see also the right panel of Fig. 4.5). In addition to the proton-rich conditions in the innermost ejected zones visible in simulations by different groups [22, 93, 137], our models consistently include neutrino-absorption reactions in the nucleosynthesis calculations allowing for the occurrence of the  $\nu p$ -process. However, in our stratified spherically symmetric models the accretion rate is rapidly reduced (and with this the neutrino luminosities) after the onset of the explosion. In a more realistic scenario considering convective turnover in the hot mantle, continued accretion is expected to maintain a large neutrino luminosity beyond the onset of the explosion and to further support the  $\nu p$ -process.

#### 4.4.4 Sensitivity

In order to understand the sensitivity of our results one must consider the dependence of the  $\nu p$ -process on the conditions during the ejection of matter in supernova explosions. There are several essential parameters in addition to the entropy  $s$  (set during the explosion it determines the nature of

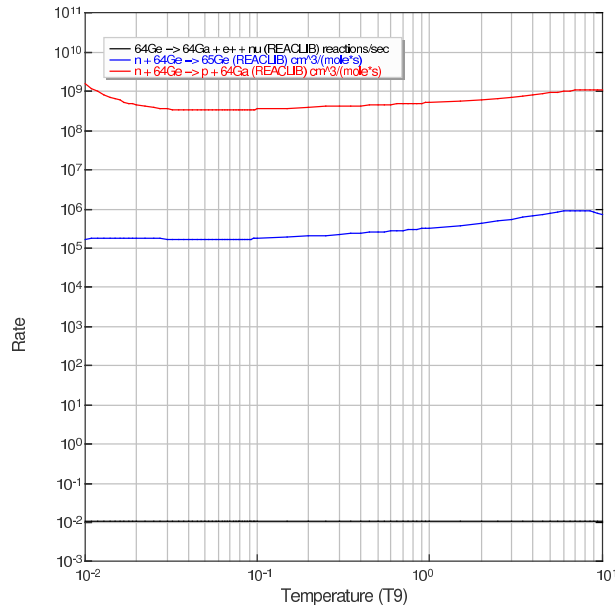


**Figure 4.8:** Reaction rates for different reactions ( $(n, p)$ ,  $(n, \gamma)$ , and  $\beta$ -decay on  $^{64}\text{Ge}$  as function of temperature. It can clearly be seen that the  $(n, p)$  reaction dominates at the conditions experienced during the  $\nu p$ -process.

the alpha-rich freeze-out of explosive nucleosynthesis). One is the  $Y_e$ -value of the matter when nuclei are formed. The larger the  $Y_e$ -value, the larger is the proton abundance, producing a larger neutron abundance for the same antineutrino flux during the  $\nu p$ -process. This permits a more efficient bridging of beta-decay waiting points by  $(n, p)$ -reactions in the flow of proton captures to heavier nuclei. The location (radius  $r$ ) of matter during the formation of nuclei and the ejection velocity also influence the  $\nu p$ -process by determining the intensity and duration of the antineutrino flux which the matter will experience. Finally, the long-term evolution of the neutrino luminosities and energy spectra during the cooling phase of the proto-neutron star plays an important role. These factors are poorly known due to existing uncertainties in the supernova explosion mechanism.

To test the dependence of the nucleosynthesis on these parameters we have also carried out parametric calculations based on adiabatic expansions similar to those used in refs. [78, 97] but for a constant realistic entropy per nucleon  $s = 50 k_B$ . This allows exploration of the sensitivity of the nucleosynthesis without the need to perform full radiation-hydrodynamical calculations. An example is given in Figure 4.9 which shows the dependence of the  $p$ -nuclei abundances as a function of the  $Y_e$  value of the ejected matter. The different  $Y_e$  values have been obtained by varying the temperatures of the neutrino and antineutrino spectra assuming Fermi-Dirac distributions for both. Close to  $Y_e = 0.5$  (and below) essentially no nuclei beyond  $A = 64$  are produced. Nuclei heavier than  $A = 64$  are only produced for  $Y_e > 0.5$ , showing a very strong dependence on  $Y_e$  in the range 0.5–0.6. A clear increase in the production of the light  $p$ -nuclei,  $^{92,94}\text{Mo}$  and  $^{96,98}\text{Ru}$ , is observed as  $Y_e$  gets larger. However, the abundances of these nuclei are still a factor 10 smaller than the ones of  $^{84}\text{Sr}$ . Similar results have been recently obtained by Pruet *et al.* [116], in a study of the nucleosynthesis that occurs in the early proton-rich neutrino wind. These authors suggest that the production of  $^{92}\text{Mo}$  is sensitive to the experimentally unknown masses of nuclei around  $^{92}\text{Pd}$ . Future experimental determinations of these masses will help to decide if the solar system abundances of light  $p$ -nuclei can be due to the  $\nu p$ -process.

#### 4.4.5 Conclusions

All core-collapse supernova explosions, independent of existing model uncertainties, will eject hot, proton-rich explosively processed matter subject to strong neutrino irradiation. In all cases, the  $\nu p$ -

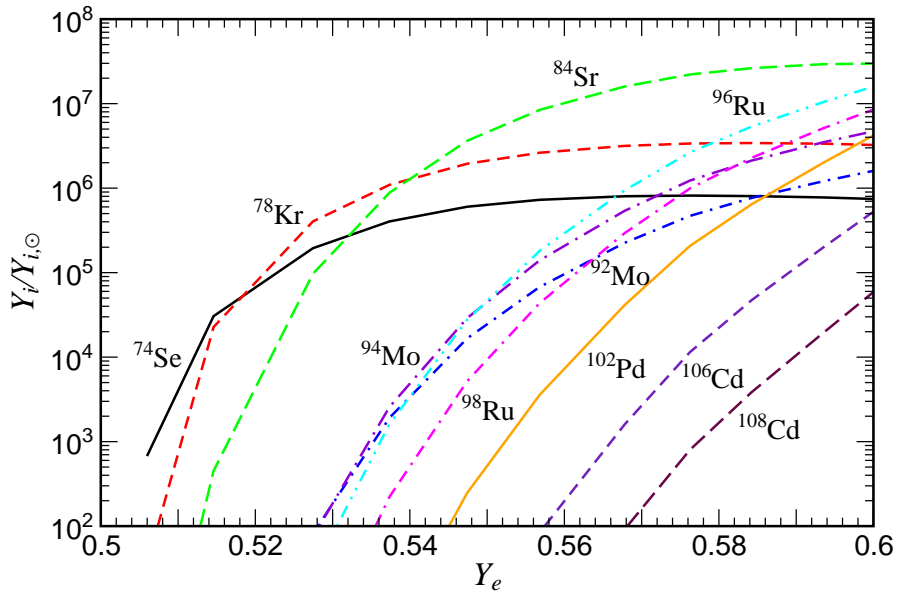


**Figure 4.9:** Light  $p$ -nuclei abundances in comparison to solar abundances as a function of  $Y_e$ . The  $Y_e$ -values given are the ones obtained at a temperature of 3 GK that corresponds to the moment when nuclei are just formed and the  $\nu p$ -process starts to act.

process will operate in the innermost ejected layers producing neutron deficient nuclei above  $A = 64$ . As the innermost ejecta, this matter is most sensitive to the details of individual explosions, thus their abundances will vary noticeably from supernova to supernova (e.g. as a function of stellar mass, rotation, etc.). The final amount of matter ejected will also depend on the intensity of the fallback, but as discussed in ref. [73], mixing before fallback will always lead to the ejection of elements synthesized, even in the innermost layers. Ref. [73] explains the abundances seen in hyper-metal poor stars by the ejecta of faint/weak core-collapse supernovae. Such faint supernova will generally have small expansion velocities favoring an enhanced production of  $\nu p$ -elements, offering an explanation for the presence of Sr in the star HE 1327-2326 [47]. Our studies of the  $\nu p$ -process show that the elements between Zn and Sr should be co-produced together with Sr. The observation of these elements, which with the exception of Ge and Rb are not detectable from the ground in optical lines, but possible from space in the infrared or near ultraviolet (e.g. the Hubble Space and Spitzer Space telescopes), can provide support for the occurrence of the  $\nu p$ -process at early times in the Galaxy and contribute valuable information about the conditions experienced by the inner supernova ejecta in order to constrain current theoretical models of supernova explosions.

Chemical evolution studies[141] require such a nucleosynthesis component and will also be a valuable aid in coming to a full understanding of the  $\nu p$ -process contribution to the chemical evolution of galaxies. If the Sr observed in the star HE1327-2326 is in fact produced by the  $\nu p$ -process, a similar abundance ratio  $[X/Fe]$  should be expected for all the elements X between Zn and Sr. The observation of the lines of many of these elements is not possible from the ground. Thus, the predictions given here can be a motivation for observations by other means (e.g. the Hubble Space Telescope). Moreover, the observed elemental abundances of elements between Zn and Sr could provide us with valuable information about the conditions experienced by the inner supernova ejecta that can be used to constrain current theoretical models of supernova explosions. The variations in the contribution of the  $\nu p$ -process (represented by Sr, Y, and Zr) and the r-process (producing the heaviest elements up to Th and U) [39, 127], can shed light on the connection of these two processes (both experiencing a strong neutrino flux) and provide information about the class of supernovae producing also heavy r-process nuclei. Further studies are required to fully understand the  $\nu p$ -process contribution to the chemical evolution of the Galaxy.

## 4.5. The Reaction Flow

In the previous Sections, the characteristics of the Fe-group ejecta due to neutrino-induced reactions and the mechanism and properties of the  $\nu p$ -process have been discussed. Now, we will illustrate how the nucleosynthesis proceeds as function of time (and therefore temperature and density) in a typical mass layer experiencing the  $\nu p$ -process. The layer of model B07 is located  $0.002 M_{\odot}$  outside of the mass cut. Due to the high temperatures achieved the matter is fully dissociated at shock passage and nucleosynthesis processes start from free neutrons and protons only. For each selected time slice values for temperature and density are given. The time indicates time after maximum temperature. In the top panel of each Figure isotopic abundances are shown. On the  $N$ - $Z$ -plane (bottom panel) each nucleus is indicated by a square located at its neutron number  $N$  and proton number  $Z$ . Stable nuclei are indicated by filled black squares. For all the unstable nuclei, the abundance is color-coded on a logarithmic scale. Only nuclei with abundances larger than  $10^{-30}$  are drawn. The time slices are selected to show the different phases of nucleosynthesis which can be observed.

The maximum temperature reached by a layer experiencing the  $\nu p$ -process is of the order of  $2 \times 10^{10}$  K while the density is of the order of  $10^8$  g/cm<sup>3</sup>. At these conditions matter consists mainly of neutron and proton plus some  $^4\text{He}$  (Fig. 4.10, top left). As the matter expands and cools after the shock passage, the nucleons and  $\alpha$ -particles combine to heavier nuclei. At  $\sim 10^{10}$  K and  $10^7$  g/cm<sup>3</sup> (Fig. 4.10, top right) the  $3\alpha$ -reaction helps to bridge the mass gap at  $A = 8$ . Now the matter flow continues through the  $\alpha$ -elements (O, Ne, Mg, Si, S, Ar, Ca, and Ti) and eventually synthesizing Fe-group nuclei. At temperatures of  $\sim 6 \times 10^9$  K matter falls out of NSE (see the discussion on NSE in Section 2.4). The bottom left panel of Fig. 4.10 is a snapshot at these conditions. At non-NSE conditions (Fig. 4.10, bottom right) the even-even  $\alpha$ -elements at  $A = 20, 24, 28, 32, 36, 40$  (corresponding to  $^{20}\text{Ne}$ ,  $^{24}\text{Mg}$ ,  $^{28}\text{Si}$ ,  $^{32}\text{S}$ ,  $^{36}\text{Ar}$ , and  $^{40}\text{Ca}$ ) show enhanced abundances compared to the odd elements. The Fe-group elements are produced in a broad peak around  $A = 56$ . However, there is no significant production of elements beyond  $A = 64$ . At temperatures around  $10^9$  K (Fig. 4.11, top row) the reaction flow is on the proton-rich side (in the region of the  $rp$ -process; see [124]) and starts to overcome the waiting point at  $A = 64$ . The waiting points of the reaction flow can clearly be seen in the bottom left panel of Fig. 4.11. Also in this Figure, the enhancement of the even-even waiting point nuclei  $^{64}\text{Ge}$ ,  $^{68}\text{Se}$ ,  $^{72}\text{Kr}$ , and  $^{76}\text{Sr}$  (producing  $^{64}\text{Zn}$ ,  $^{68}\text{Zn}$ ,  $^{72}\text{Ge}$ , and  $^{76}\text{Se}$  after decay to stability) is apparent. The last time slice in this series (Fig. 4.11, bottom right) show the situation when charged particle reactions freeze-out and matter starts to  $\beta$ -decay to stability.

## 4.6. A $20 M_{\odot}$ Model at Solar Metallicity

This Section is devoted to the nucleosynthesis calculations for a  $20 M_{\odot}$  pro-collapse star. This model is part of a new series of models, series LS07. This series uses the same method to obtain explosions as in series B (as described in Section 3.2) where the rates for the neutrino and antineutrino absorptivities and emissivities are enhanced by a constant factor. Choosing a value of seven for the parameter corresponds to an average choice in the parameter space. Dense nuclear matter is described using the Lattimer-Swesty equation of state. The series LS07 consists of pre-collapse stars on a grid of initial main sequence masses which includes  $15 M_{\odot}$ ,  $18 M_{\odot}$ ,  $20 M_{\odot}$ ,  $25 M_{\odot}$ ,  $30 M_{\odot}$ ,  $40 M_{\odot}$ , and  $50 M_{\odot}$ . Note that the  $40 M_{\odot}$  and the  $50 M_{\odot}$  models do not explode for the current choice of the enhancement factor.

The supernova shock increases the temperatures and densities when passing through the Si, O, Ne, C, He, and H zones. This allows for nuclear reactions to proceed on a much shorter timescale (compared to the hydrostatic evolution) and also additional reactions become possible. Figure 4.12 shows the maximum temperatures and densities obtained during the explosion in the explosion calculations based on AGILE-BOLTZTRAN. In particular, the explosion energy for this  $20 M_{\odot}$  star is  $0.4396 \times 10^{51}$  erg at  $t = 0.3217$  s after bounce. This does not include the nuclear energy generated during explosive nuclear burning. Including the nuclear energy we find a total explosion energy of  $0.285 \times 10^{51}$  erg. The mass cut for this model is located at  $1.503 M_{\odot}$ . Already in 1980, Weaver & Woosley [148] have recognized that the matter behind the shock is strongly radiation dominated. For the assumption of an almost homogeneous density and temperature distribution behind the shock, the supernova energy is related

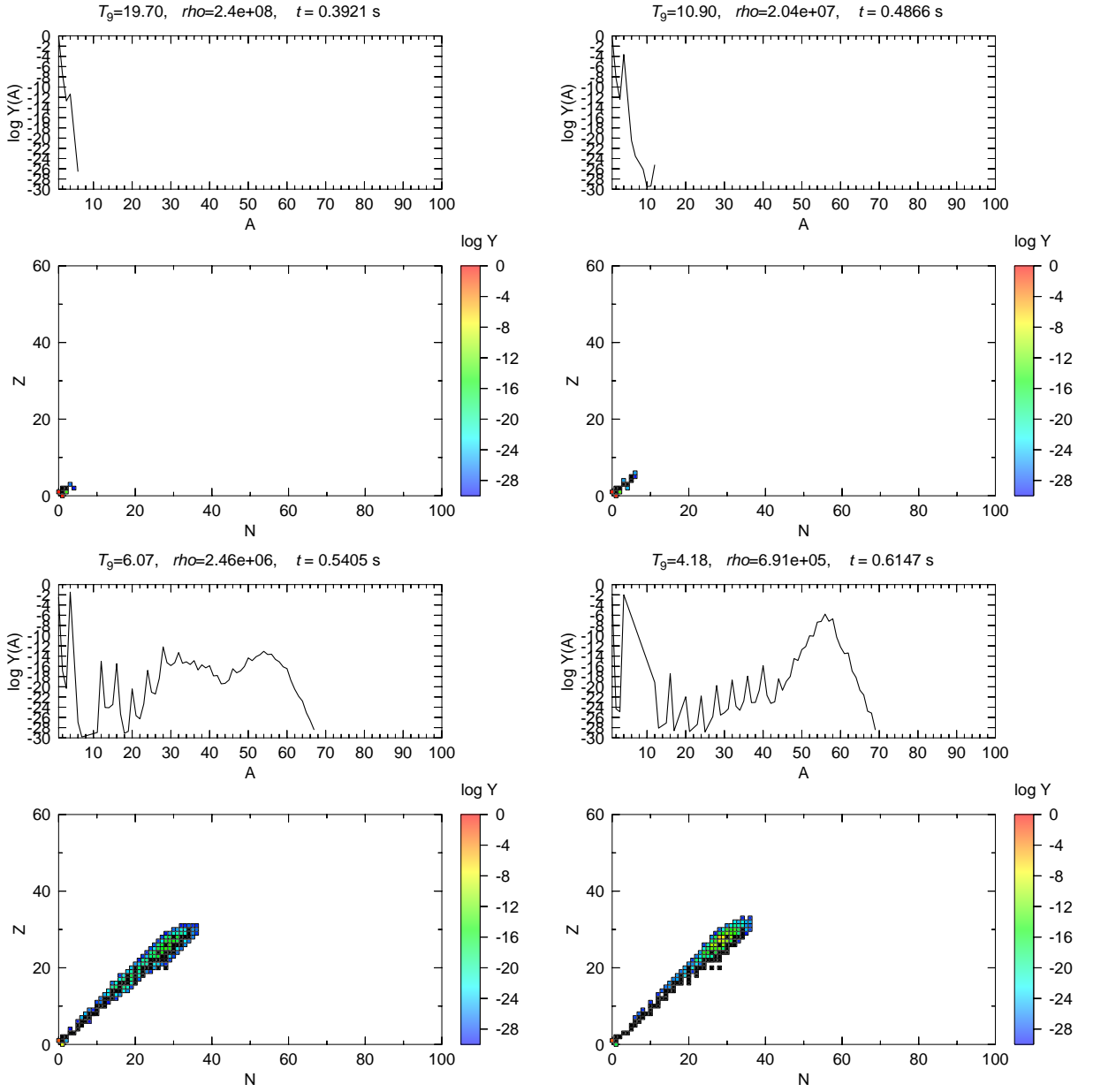


**Figure 4.10:** Time slices of isotopic abundances (versus mass number) and individual abundances for each nucleus in the  $N$ - $Z$ -plane. The time indicates time after the temperature maximum is reached. The temperature is given in units of  $10^9$  K and the density in units of  $\text{g}/\text{cm}^3$ .  
*Top left:*  $T_9 = 19.70$ ,  $\rho = 2.4 \times 10^8$ . *Top right:*  $T_9 = 10.90$ ,  $\rho = 2.04 \times 10^7$ . *Bottom left:*  $T_9 = 6.07$ ,  $\rho = 2.46 \times 10^6$ . *Bottom right:*  $T_9 = 4.18$ ,  $\rho = 6.91 \times 10^5$ .

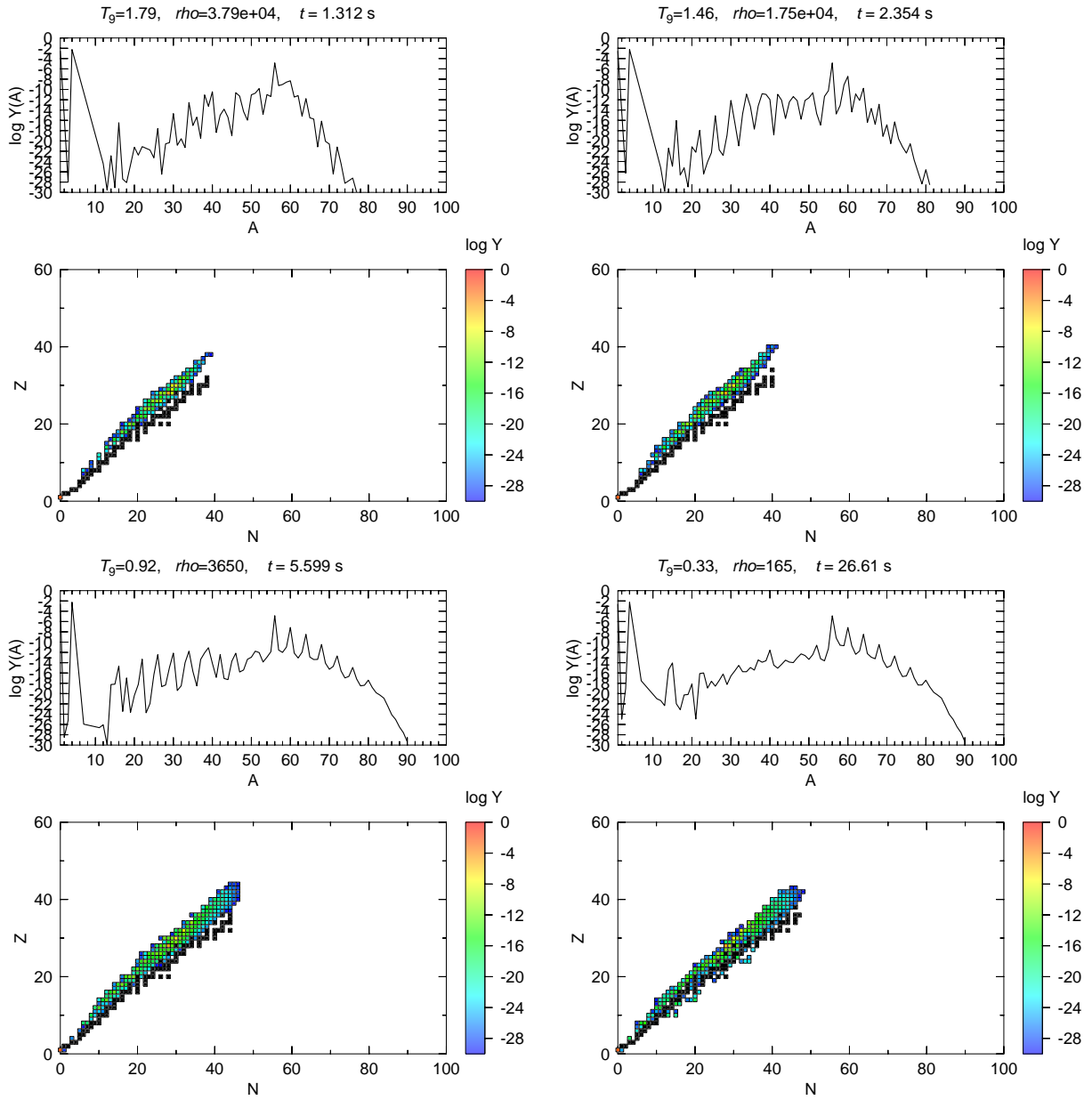


**Figure 4.11:** Time slices of isotopic abundances (versus mass number) and individual abundances for each nucleus in the  $N$ - $Z$ -plane. The time indicates time after the temperature maximum is reached. The temperature is given in units of  $10^9$  K and the density in units of  $\text{g}/\text{cm}^3$ . *Top left:*  $T_9 = 1.79$ ,  $\rho = 3.79 \times 10^4$ . *Top right:*  $T_9 = 1.46$ ,  $\rho = 1.75 \times 10^4$ . *Bottom left:*  $T_9 = 0.92$ ,  $\rho = 3.65 \times 10^3$ . *Bottom right:*  $T_9 = 0.33$ ,  $\rho = 1.65 \times 10^2$ .

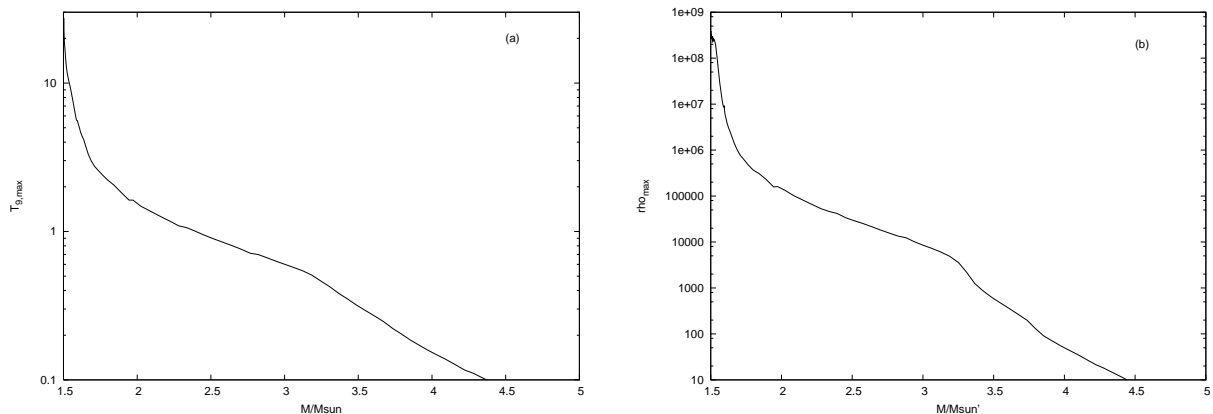


**Figure 4.12:** Maximum temperatures and densities attained in the inner part of the ejecta ( $1.5 < M/M_{\odot} < 5$ ) during the passage of the shock front. Only the inner parts of the ejecta experience temperatures in excess of  $2 \times 10^9$  K.

to the radiation energy within the radius  $r$  of the shock front:

$$E_{\text{SN}} = \frac{4\pi}{3} r^3 T(r)^4. \quad (4.8)$$

Knowing the explosion energy and for an appropriate choice of temperature this equation can be solved for  $r$ . For example, using  $T = 5 \times 10^9$  K the lower boundary of complete Si exhaustion can be estimated without performing nucleosynthesis calculations.

Explosive Si burning can be divided into three different regimes: (i) incomplete Si burning, (ii) complete Si burning (Si exhaustion) undergoing a normal freeze-out, and (iii) complete Si burning undergoing an alpha-rich freeze-out. It has been long recognized that it depends on the peak temperatures and densities during the passage of the shock which of the three regimes is encountered (see Fig. 20 in [151] and Fig. 5 in [135]). Complete Si burning is characterized by abundances following an NSE distribution (depending only on nuclear binding energies, partition functions, temperatures, and densities). The continuing expansion leads to decreasing temperatures and densities until the freeze-out of charged-particle reactions. The type of freeze-out obtained depends on how long NSE can be sustained during the expansion (and hence the cooling). When the final abundances correspond to the NSE abundances, this means that the NSE was sustained until freeze-out of charged-particle reactions. This normal freeze-out occurs at high densities due to the strong density dependence of the  $3\alpha$ -reaction. At high densities the  $3\alpha$ -reaction can still burn  ${}^4\text{He}$  into heavier nuclei while the temperature decreases, favoring heavier nuclei over  $\alpha$ -particles. At lower densities the  $3\alpha$ -reaction freezes-out earlier, decoupling the abundances of  ${}^4\text{He}$  from the abundances of the heavier nuclei. Figure 4.13 shows the conditions of mass zones undergoing explosive Si burning. In our model only  $\alpha$ -rich freeze-out and incomplete Si burning occurs. Normal freeze-out occurs predominantly in type Ia supernovae with densities in excess of  $10^8 \text{ g cm}^{-3}$ .

In Figure 4.14 we show major abundances resulting from the nucleosynthesis calculations. In the innermost mass zones which experience complete Si exhaustion ( $M < 1.6M_{\odot}$ ) the dominant nucleus is  ${}^{56}\text{Ni}$ . Outside of this region, incomplete Si burning and explosive O burning occur, producing  ${}^{28}\text{Si}$ ,  ${}^{32}\text{S}$ ,  ${}^{36}\text{Ar}$ , and  ${}^{40}\text{Ca}$ . Explosive Ne burning contributes to the abundance of  ${}^{16}\text{O}$  and to a smaller extent to the abundances of  ${}^{24}\text{Mg}$  and  ${}^{28}\text{Si}$ . In layers beyond explosive Ne burning the composition remains essentially unaltered. For comparison we also show the abundances of the pre-supernova star (Fig. 4.15). For the region below  $1.4 M_{\odot}$  no detailed composition is given. This corresponds to the Fe core and will become part of the neutron star during the supernova explosion.

When we compare our results here to induced explosive nucleosynthesis calculations [134] (TNH96) the boundary between complete and incomplete Si burning is about one tenth of a solar mass deeper in the star in our model here. This is related to the explosion energy ( $\approx 3 \times 10^{50}$  erg) which is lower

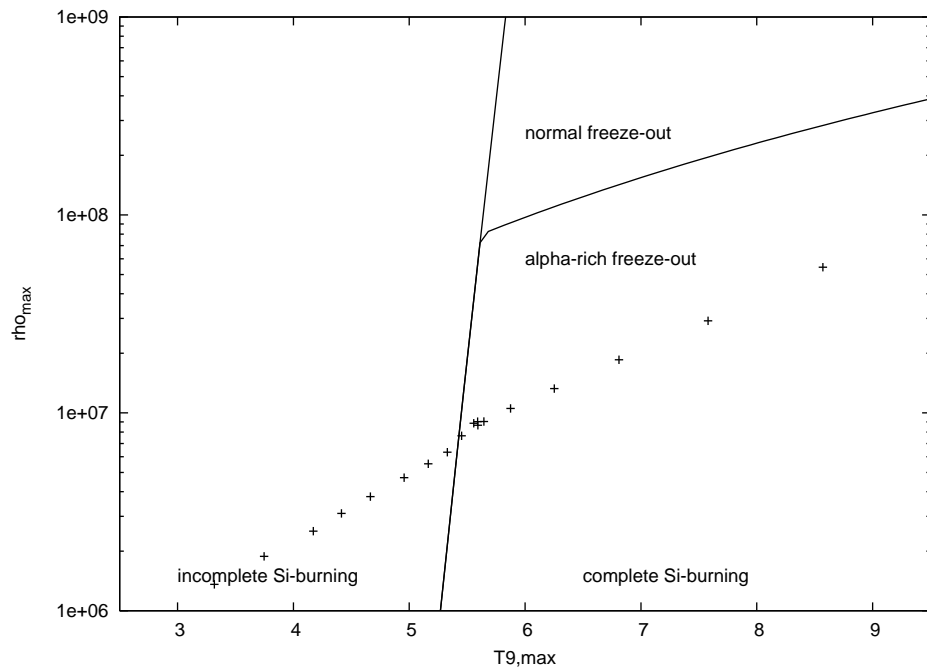


**Figure 4.13:** Peak temperatures and densities of the innermost ejecta in supernova explosions. Each filled square marks the conditions of one masszone. The lines divided the peak temperature and density plane into the different regimes of Si burning.

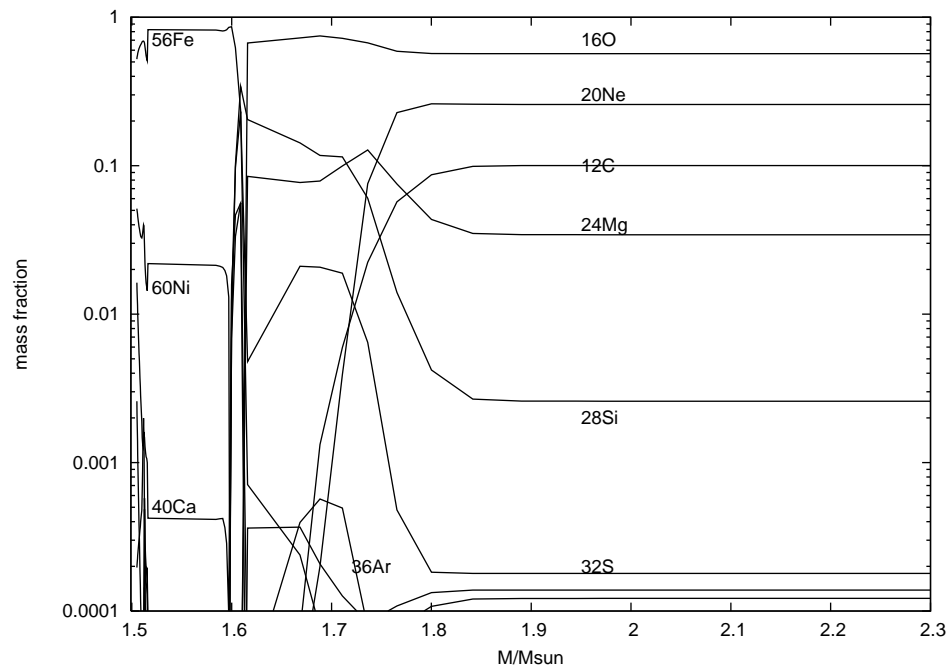


**Figure 4.14:** Mass fractions for the major nuclei resulting from explosive nucleosynthesis. Below  $1.6M_{\odot}$  Fe group nuclei dominate. Outside  $2M_{\odot}$  matter is essentially unaltered.



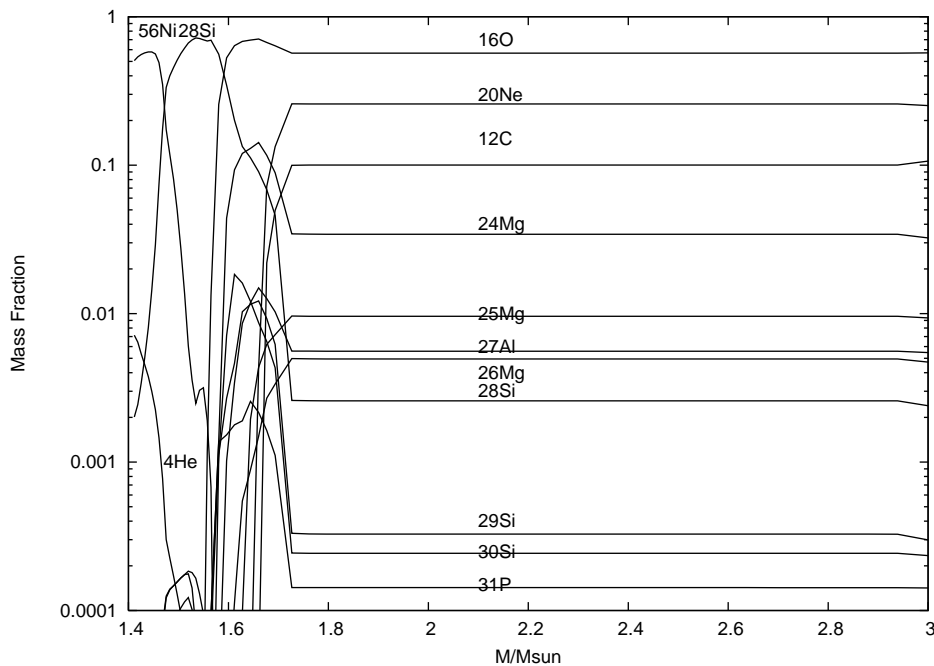


**Figure 4.15:** Mass fractions for the major nuclei at the end of hydrostatic burning and before collapse and passage of the supernova shock front. No composition is given for zones with  $M < 1.4M_{\odot}$ .

than the canonical value of  $10^{51}$ erg. For induced supernova explosions the thermal energy is chosen such that the explosion energy is about  $10^{51}$ erg (and the ejected Ni mass is about  $0.07M_{\odot}$ ). Such a low explosion energy as seen in our model results in reduced supernova shock heating, especially in the layers undergoing explosive O burning. This leads to lower abundances of intermediate mass elements, e.g. like  $^{40}\text{Ca}$  compared to observations. However, a significant difference between our calculations here and the nucleosynthesis calculations by [134] is the determination of the location of the mass cut. In a thermal bomb induced explosion model the location of the mass cut is essentially a free parameter which needs to be constrained through observations (for details see for example [134]). The explosion simulations used here are based on either an enhancement of the neutrino and antineutrino absorptivities or based on the decrease of neutrino neutral current scattering cross sections. This allows for the mass cut to emerge consistently from the simulation. In particular, the explosion simulations used here take into account the changes in the electron fraction of matter during the explosion. This can be seen in Figures 4.16 and 4.17.

The most proton-rich mass zone in this model reaches an electron fraction of  $Y_e = 0.529$ . In such a proton rich environment the nucleosynthesis proceeds well on the proton-rich side of the valley of  $\beta$ -stability. Figures 4.18 to 4.21 show the abundance distributions in the  $N$ - $Z$ -plane (where  $N$  denotes the number of neutrons and  $Z$  denotes the number of protons in each nucleus) for four snapshots of hydrodynamical conditions. Figure 4.18 shows the initial abundance distribution in this masszone in the pre-supernova phase of the star. The second snapshot (Fig. 4.19 at  $T = 19.4 \times 10^9\text{K}$ ) shows an almost dissociated phase of the ejected which is associated with the passage of the supernova and shock and the accompanying temperature increase. Figure 4.20 is taken at a temperature of  $T = 6.2 \times 10^9\text{K}$ . This is still well within a NSE regime for the abundances. Figure 4.21 corresponds to a temperature of  $T = 0.8 \times 10^9\text{K}$ . We note that the most abundant nuclei are  $N \approx Z$  nuclei, several units away from the valley of  $\beta$ -stability. It can also be noted that the nucleosynthesis flow proceeds well beyond the Fe group nuclei, in this case reaching the region of the light p-nuclei Mo and Ru. However, the total abundances of Mo and Ru synthesized in this model is not sufficient to account to the observed values.

To conclude this Section we show integrated abundances for the He-core ( $\sim 5M_{\odot}$ ) of the  $20M_{\odot}$

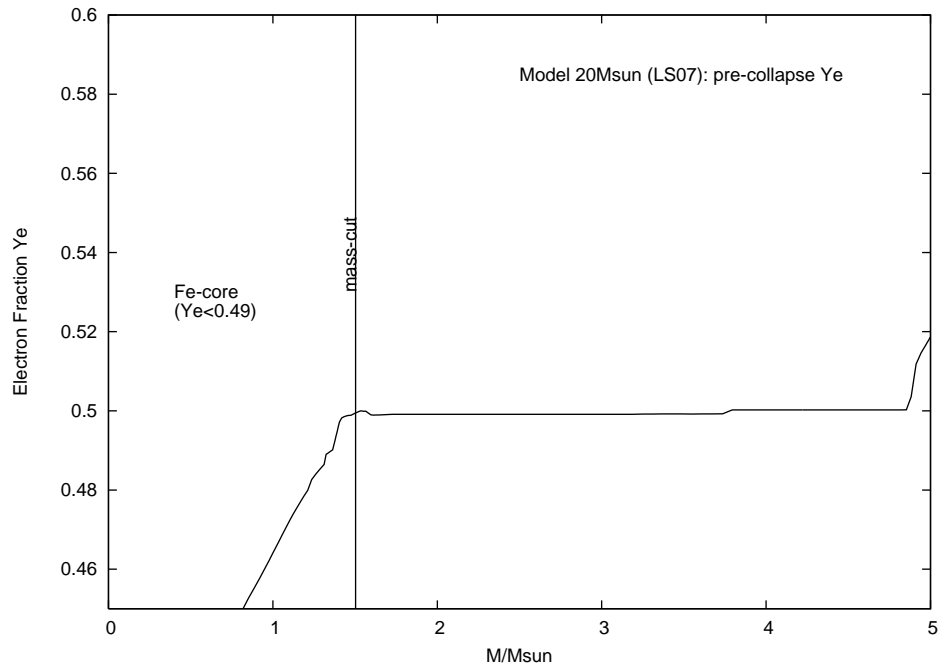


**Figure 4.16:** Electron abundances  $Y_e$  as function of radial mass. The drop to  $Y_e < 0.49$  indicates the Fe-core. The position of the mass cut is crucial for the composition of the Fe group elements.

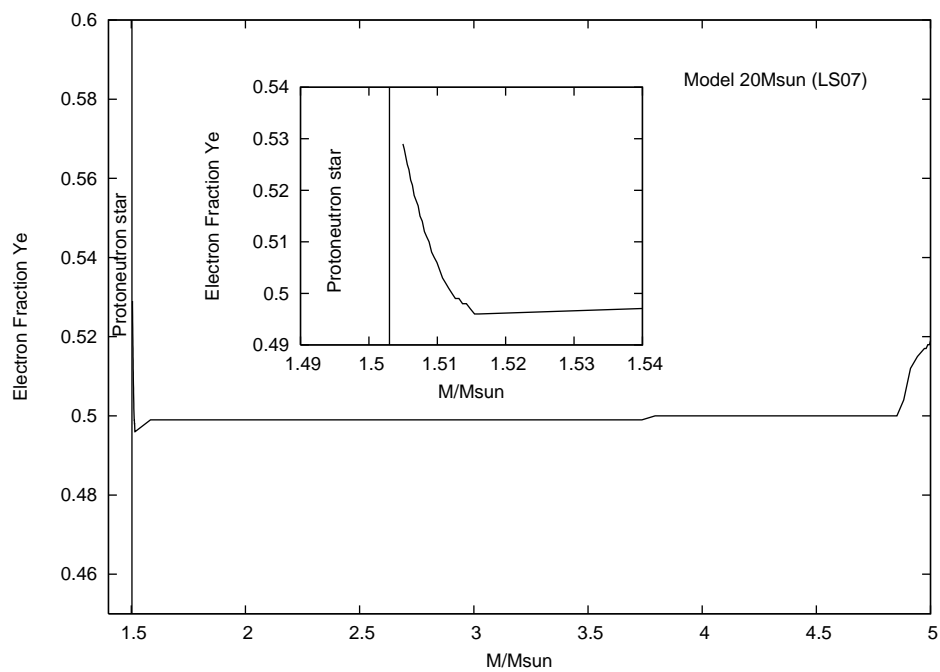


**Figure 4.17:** Electron fraction  $Y_e$  as function of radial mass after freeze-out of charged particle reactions. Note the narrow proton-rich layer in the innermost ejecta. The horizontal line indicates the location of the mass cut. The inset is a zoom-in on the proton-rich layers.

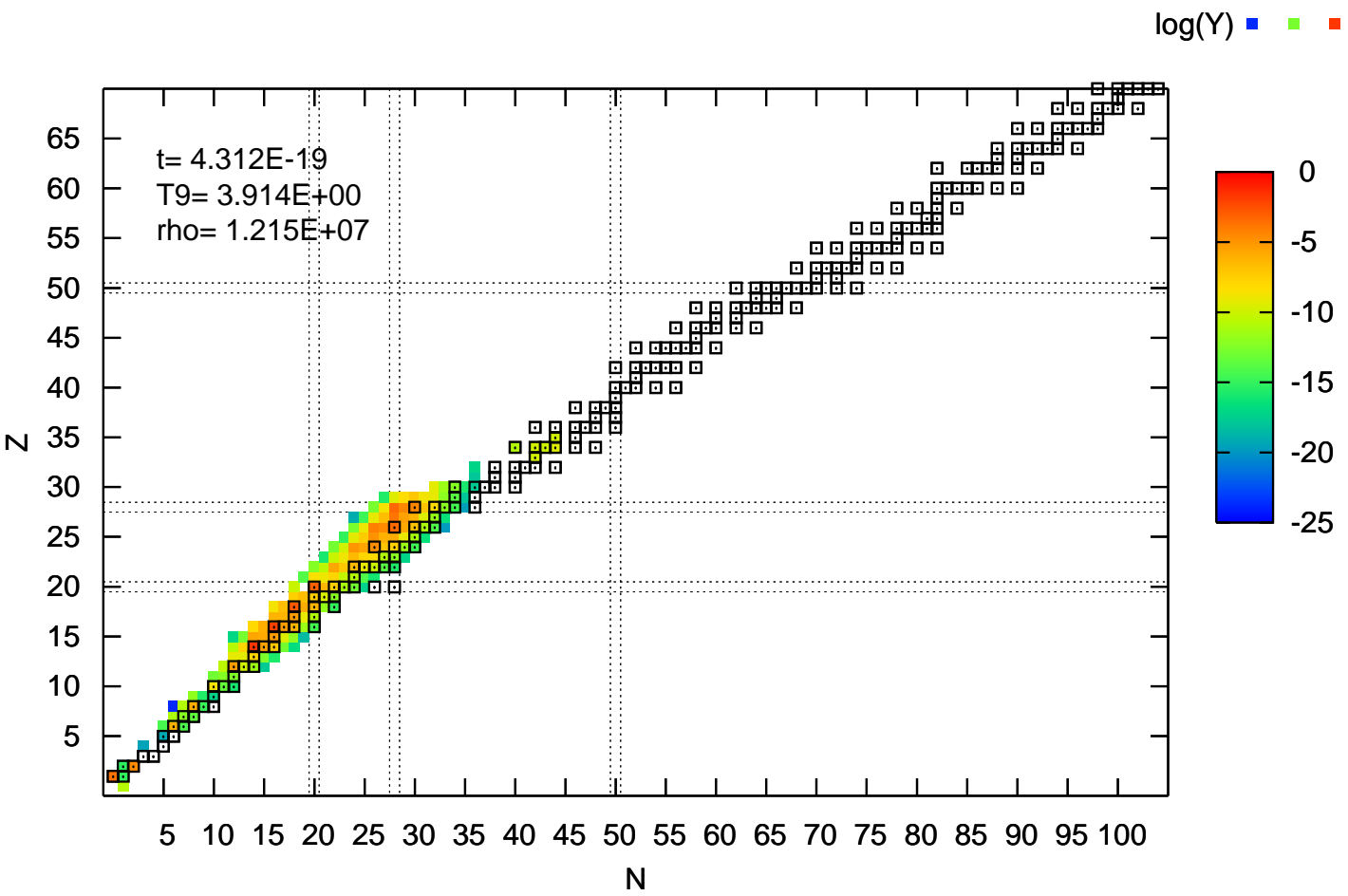


**Figure 4.18:** Initial abundance distribution in the  $N$ - $Z$ -plane for a the most proton-rich mass zone of the  $20M_{\odot}$  model. This zone is located at  $1.505M_{\odot}$  and reaches a final electron fraction of  $Y_e = 0.529$ . This snapshot is taken before collapse.

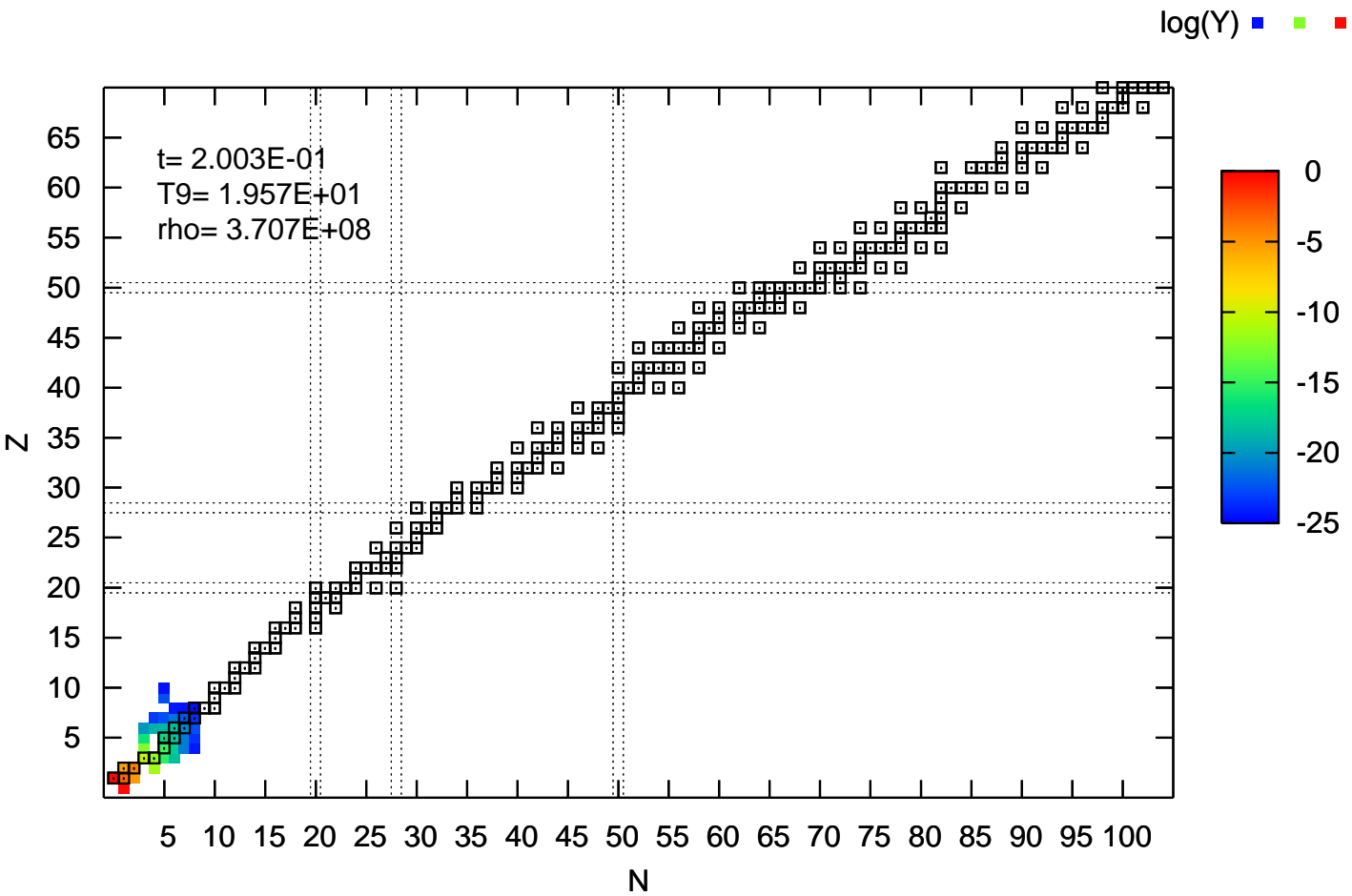


**Figure 4.19:** Abundance distribution in the  $N$ - $Z$ -plane for a the most proton-rich mass zone of the  $20M_{\odot}$  model. This zone is located at  $1.505M_{\odot}$  and reaches a final electron fraction of  $Y_e = 0.529$ . This snapshot is taken for a temperature  $T = 19.4 \times 10^9$  K.

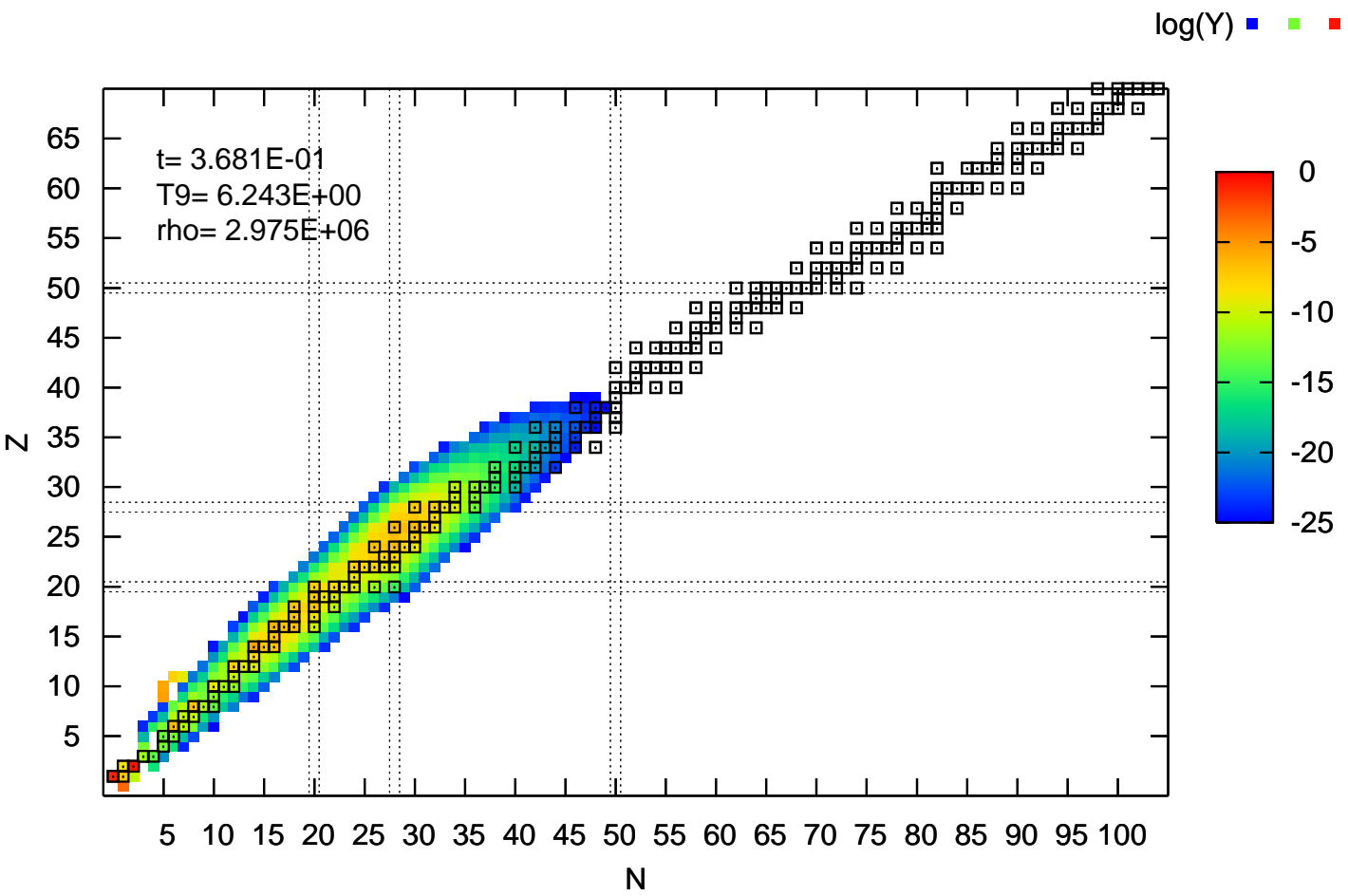


**Figure 4.20:** Abundance distribution in the  $N$ - $Z$ -plane for a the most proton-rich mass zone of the  $20M_{\odot}$  model. This zone is located at  $1.505M_{\odot}$  and reaches a final electron fraction of  $Y_e = 0.529$ . This snapshot is taken for a temperature  $T = 6.2 \times 10^9$  K.

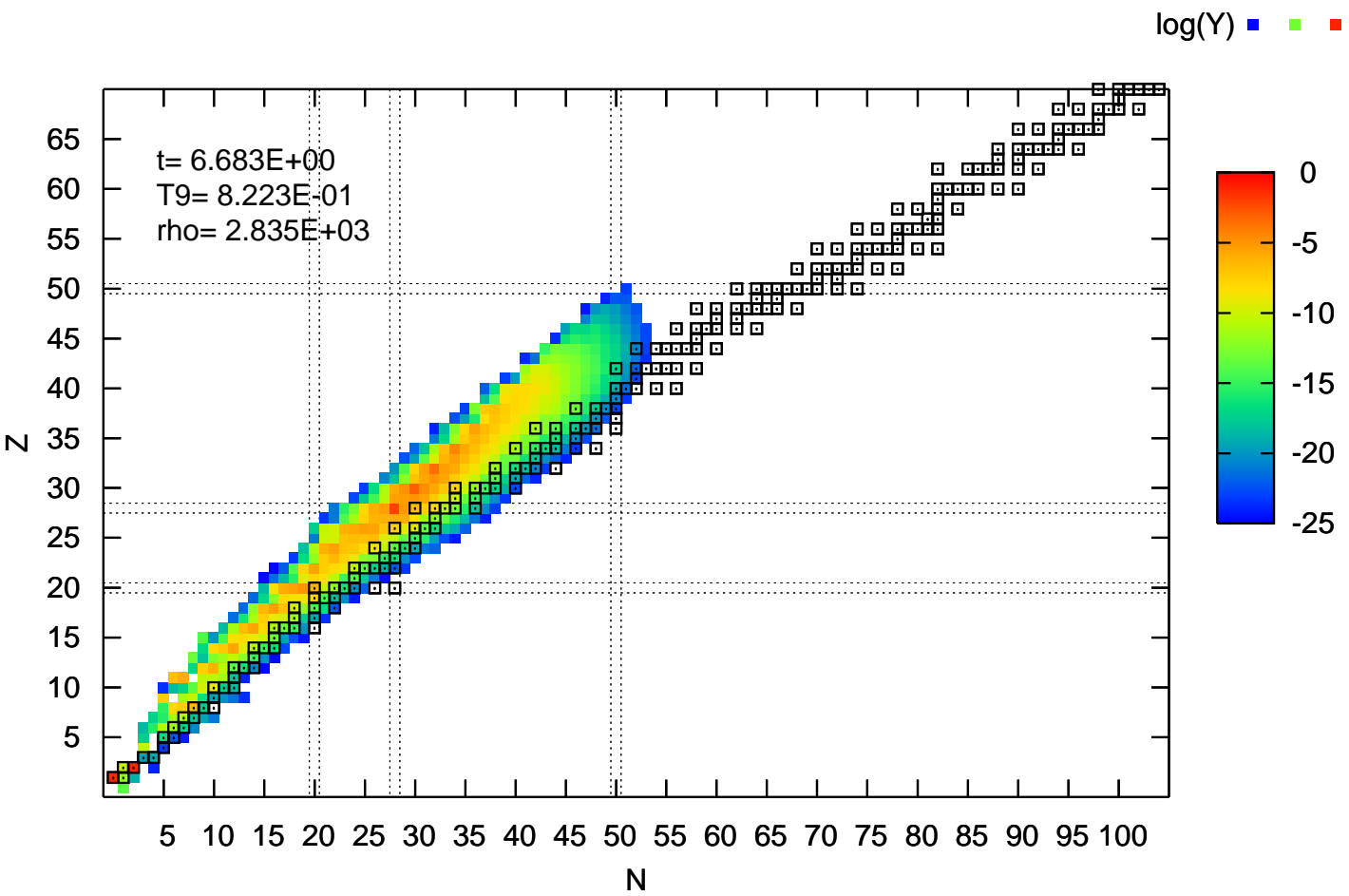


**Figure 4.21:** Abundance distribution in the  $N$ - $Z$ -plane for a the most proton-rich mass zone of the  $20M_{\odot}$  model. This zone is located at  $1.505M_{\odot}$  and reaches a final electron fraction of  $Y_e = 0.529$ . This snapshot is taken for a temperature  $T = 0.8 \times 10^9$  K.

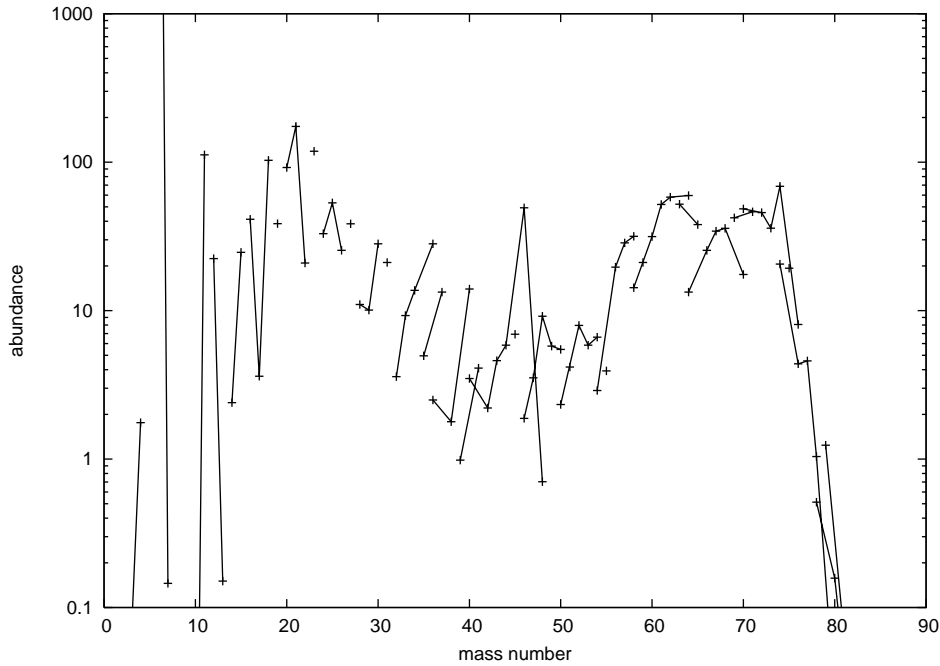


**Figure 4.22:** Isotopic abundances from the explosive processing of the He-core of a  $20M_{\odot}$  star. Note that the star was pre-enriched in s-process elements prior to the supernova explosion.

star. Figure 4.22 shows isotopic abundances. The pre-supernova star has a strongly s-process enhanced composition. In combination with the  $\nu p$ -process also contributing to the production of elements like Sr, this leads to an overproduction of the light n-capture elements relative to Fe. Second, our supernova model only has about one third of the canonical explosion energy for a core collapse supernova. Hence the shock wave and the resulting shock heating is weaker. This leads to a larger region of the star being essentially unaltered during the supernova explosion. Figure 4.23 shows the elemental yields from explosive processing of the He core. The elemental abundances are shown relative to their solar ratio.

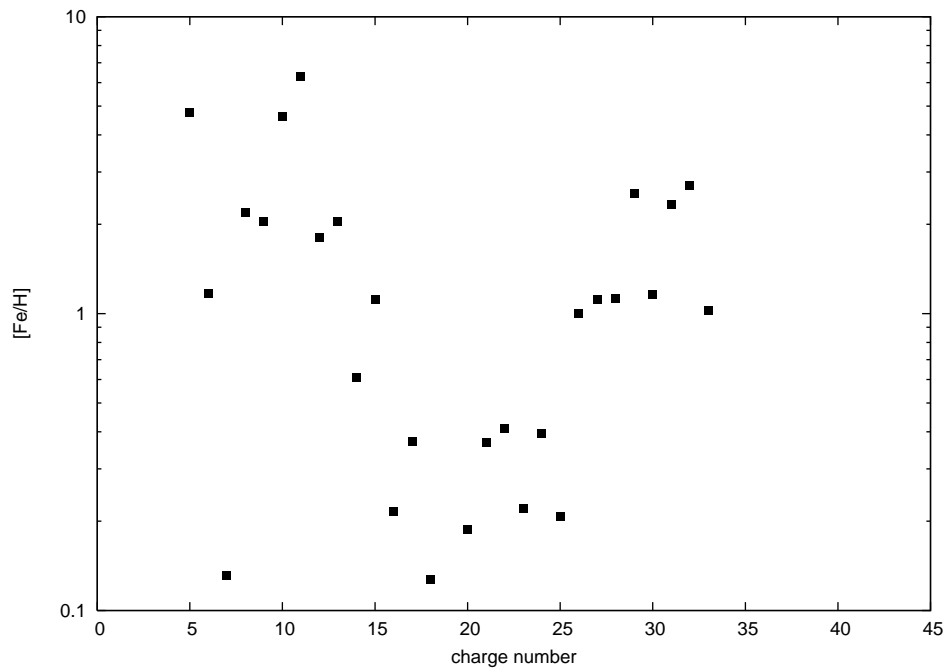


**Figure 4.23:** Elemental overabundances for the He-core of a  $20M_{\odot}$  star.



# 5

---

## The Bigger Picture: Supernovae and Galactic Chemical Evolution

The evolution of galaxies is dominated by its stellar sources contributing to the enrichment of the interstellar medium. The contributing stellar objects are low/intermediate mass stars ( $M < 8 M_{\odot}$ ) and massive stars ( $M > 8 M_{\odot}$ ). Depending on the initial mass and metallicity, different end stages like planetary nebulae, supernovae, or hypernovae/gamma-ray bursts can be expected. Planetary nebulae contribute to the light elements, whereas the elements from oxygen to nickel are due to explosive events (combination of type II and type Ia supernovae). Understanding the evolutionary endpoints of stars is therefore essential in understanding the enrichment of heavy elements as function of time (and space). Especially understanding supernovae which are the main contributors to nucleosynthesis in galaxies is indispensable. Galactic chemical evolution is a global test for all contributing stellar yields, especially ejecta of SNe II and SNe Ia (e.g. [46]).

In this Chapter, the question is addressed whether the initial metallicity affects the way of explosive processing (e.g. by changing the neutron-richness of matter measured by  $Y_e$ ) or influences the stellar evolution and consequently the final nucleosynthesis products. First, the dependence of the stellar evolution of single stars on the initial metallicity is outlined. Then, the possible direct/indirect metallicity dependence of the explosive end stages, i.e. type Ia and type II supernovae, and their yields will be given. Also, the expected rates of these events will be briefly discussed. The general questions will be outlined and the trend of individual elements will be contrasted to observations.

### 5.1. Stellar Evolution and Explosive End Stages

---

The evolution of single stars can be followed in the Hertzsprung-Russell (HR) diagram (see e.g. [70]). Their fate is mainly determined by the initial mass and composition. This implies in principle also the history of mass loss, but in theoretical modeling the mass loss prescription adds a degree of freedom. Rotation can drastically affect the evolutionary track of a star in the HR diagram due to modification of the surface composition, induced by rotational diffusion, which directly affects the mass loss by stellar winds. The mass loss rates depend on metallicity via the interaction of radiation transport with the surface composition. The present theoretical and observational knowledge was recently summarized (see e.g. [99]). In general this leads to low metallicity stars, experiencing less mass loss than high metallicity stars and therefore possessing larger He cores and H envelopes at the end of their life. The same applies to the C-O core size after He-burning, which determines the final fate of the star, due to the much shorter burning timescales of the later burning stages (see Figure 5.1). The metallicity also enters stellar nucleosynthesis processes: (i) Some nucleosynthesis processes are of secondary nature, like e.g. the s-process, requiring initial Fe in stellar He-burning. (ii) Other processes are of primary nature, like the production of Fe-group elements in both types of supernovae.

The resulting end stage (SN II, SN Ia, or planetary nebula) of a star depends on its initial mass and metallicity. The lower boundary for stars to form massive enough cores to undergo core collapse is at  $\sim 9 M_{\odot}$ . For stars above  $10 M_{\odot}$  core collapse is the only fate. In between, stars form O-Ne-Mg cores which can either collapse and form a neutron star or lose their envelope and result in a white dwarf. While the size of the C-O core determines the final stellar fate, its relation to the progenitor mass depends on the metallicity. Core collapse with neutron star formation leads to supernovae. Figure 5.1 (right panel) shows quantitatively the resulting explosion energy for solar metallicities from calculations discussed in Chapter 4 [92].

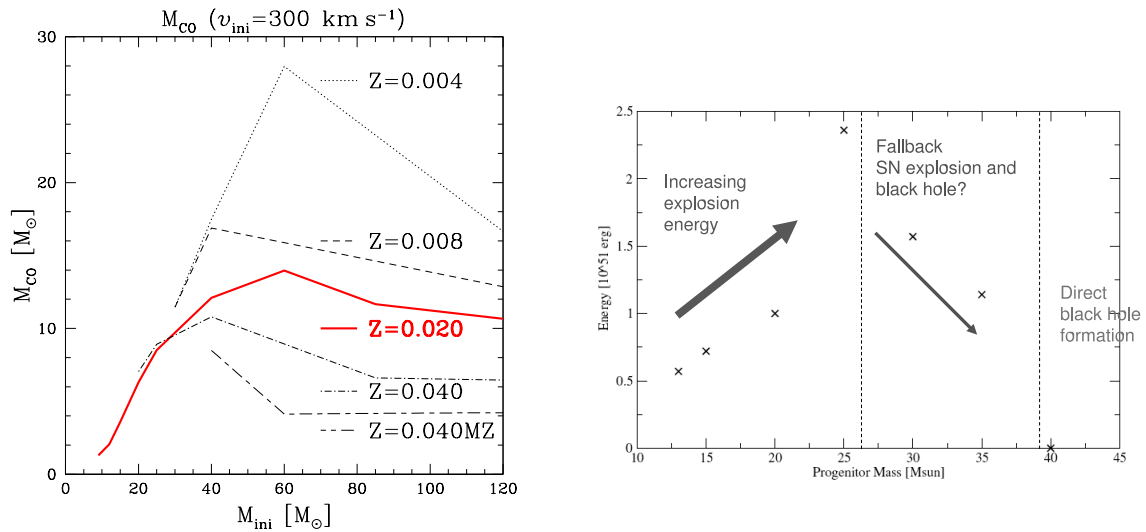


**Figure 5.1:** *Left panel:* C-O core masses from stellar evolution calculations for different metallicities as function of the initial stellar mass [63]. (Figure courtesy of R. Hirschi). *Right panel:* Explosion energy as function of progenitor mass for core collapse supernovae (of solar metallicity) due to neutrino absorption [92]. The explosion energy shows a peak around  $\sim 25 M_{\odot}$ , increasing with increasing progenitor at lower masses and decreasing fast for higher masses. Above  $\sim 40 M_{\odot}$  no explosions are observed.

At low metallicities massive stars end their life either as neutron stars (for initial mass of  $\sim 10 M_{\odot}$  to  $\sim 40 M_{\odot}$ ), as black holes through fallback onto the neutron star (initial mass between  $\sim 25 M_{\odot}$  and  $\sim 40 M_{\odot}$ ), or directly as black holes (initial mass above  $\sim 40 M_{\odot}$ ) (for a recent review see [61]). At higher metallicities mass loss becomes more important, producing smaller He and C-O cores for a given initial mass. For very massive stars the metallicity dependence can be so strong that, with increasing metallicity, the mass loss during stellar evolution is large enough to exclude black hole formation, permitting neutron stars as the only possible type of remnant.

Type Ia supernovae are not due to core collapse of a single massive star but are attributed to the thermonuclear explosion of a carbon-oxygen white dwarf in a binary system. This is supported by strong theoretical and observational indications. The basic idea of the explosion mechanism is simple: A white dwarf in a binary system grows towards the Chandrasekhar mass limit through accretion of material from the companion. The contraction and central carbon ignition cause a thermonuclear runaway since the pressure is dominated by a degenerate electron gas and shows no temperature dependence. This prevents stable and controlled burning, causing a complete explosive disruption of the white dwarf [111, 156]. The central ignition density is related to the mass accretion rate, the initial white dwarf mass, its C/O ratio, and possibly its metallicity. For details see the recent review by Höflich [67] and references therein.

## 5.2. Predicted Yields and Observations

In type Ia supernovae, most of the central region experiences conditions for complete Si burning and subsequent normal (or alpha-rich) freeze-out. The main nucleosynthesis products are Fe-group nuclei. The outer part of the central region undergoes incomplete Si burning (due to lower peak temperatures) and has therefore Ca and other alpha elements as main products. The total nucleosynthesis yields in slow deflagration models show that the production of Fe-group nuclei in comparison to their solar values is a factor of 2–3 larger than the production of intermediate nuclei from Si to Ca [16, 72].

Generally speaking, to first order we do not expect these main features to change with galactic

evolution or metallicity. The main Fe-group composition is determined by the  $Y_e$  resulting from electron captures in the explosion. The  $Y_e$  of the outer layers, not affected by electron captures, depends mildly on the initial CNO (i.e. metallicity). However, secondary effects like (a) the main sequence mass distribution of the progenitors (determining the C-O core from core He-burning and the C-O layers from burning during the accretion phase), (b) the accretion history within the progenitor binary system, or (c) the central ignition density (determined by the binary accretion history) can implicitly be affected by the metallicity [67].

The lack of a full and self consistent understanding of the explosion mechanism of core collapse supernovae aggravates the detailed prediction of nucleosynthesis yields. The correct prediction of the amount of Fe-group nuclei ejected (which includes also one of the so-called alpha-elements, i.e. Ti) and their relative composition depends directly on the explosion mechanism and the size of the Fe core. Three types of uncertainties are inherent in the Fe-group ejecta, related to (i) the total amount of Fe(group) nuclei ejected and the mass cut between neutron star and ejecta, mostly measured by  $^{56}\text{Ni}$  decaying to  $^{56}\text{Fe}$ , (ii) the total explosion energy which influences the entropy of the ejecta and with it the amount of radioactive  $^{44}\text{Ti}$  as well as  $^{48}\text{Cr}$  (decaying to  $^{48}\text{Ti}$  and being responsible for elemental Ti), and (iii) finally the neutron richness or  $Y_e = \langle Z/A \rangle$  of the ejecta, dependent on stellar structure, electron captures, and neutrino interactions [49]. The electron fraction  $Y_e$  influences strongly the overall Ni/Fe ratio. The ejecta of core collapse supernovae from models with accurate neutrino transport has been discussed in detail in Chapter 4.

High mass stars (as discussed in Section 5.1) will lead to direct black hole formation or black hole formation via fallback onto the initially formed neutron star. Accretion phenomena onto stellar mass black holes (if the surroundings are of sufficiently low density) can cause a fireball behavior and be related to gamma-ray bursts or the collapsar/hypernova phenomenon [112, 113, 150]. They indicate higher explosion energies beyond  $10^{52}$  erg and large ejected  $^{56}\text{Ni}$  masses (see e.g. [107, 143]). While the general explosive nucleosynthesis behavior is similar to supernovae (see Figs. 4.5 and 4.6), the higher explosion energy of hypernovae shifts both the complete Si-burning region ( $T_{\text{peak}} > 5 \times 10^9$  K with Co, Zn, V, and some Cr as products) and the incomplete Si-burning region ( $4 \times 10^9 > T_{\text{peak}} > 5 \times 10^9$  K with Cr and Mn as products after decay) outwards in mass. With this outward shift of the boundary the ratio of complete to incomplete Si-burning becomes larger and therefore higher ratios of [(Zn, Co, V)/Fe] and lower ratios of [(Mn, Cr)/Fe] are obtained [112]. Which fraction of high mass stars lead to such events is still uncertain and depends on rotation and magnetic field effects.

In the literature, a large amount of data for abundance ratios of various elements at low metallicity [Fe/H] is available (e.g. [2, 29, 39, 47, 68, 128]). The observational data (see Fig. 5.2) used here originate from various observational sources (collected by Prantzos [115]) and includes data from a Very Large Telescope VLT survey [29].

Explosive nucleosynthesis yields leave fingerprints in spectra, light curves, X-rays, and radioactivities/decay gamma-rays of individual events for the explosive outbursts as well as their remnants. The observed enrichment of the interstellar medium is dominated by combined contributions from type II and type Ia supernovae and depends on the onset of the event in time, the composition of the ejecta, and amount of ejecta. Galactic chemical evolution witnesses these sources and also serves as a test for yield predictions.

*Supernova rates:* Early in Galactic evolution massive stars will dominate due to their short evolution timescales. The death of these massive stars results correspondingly in a large type II + type Ib/c supernova rate. The longer lifetime of intermediate mass stars (leading to white dwarfs) and the required mass transfer in binary systems delays the onset of type Ia supernovae (for further details see [140]). Such chemical evolution calculations indicate the strong influence of SNe Ia starting at metallicities of about [Fe/H] = -1. Estimates of the present type II + type Ib/c supernova rate are 2.4 – 2.7 per century in our Galaxy, while the type Ia rate is 0.3 – 0.6 per century [145]. Thus, the total rate amounts to about 3 per century, while the ratio of core collapse (type II + type Ib) to thermonuclear (type Ia) is about 6 or inversely  $Ia/(II+Ib)=0.167$ . This will play a role for the relative Fe-group contribution from both supernova types.

*General Fe-group contribution:* For a slightly low SN Ia frequency of type  $Ia/(II+Ib)=0.15$  and typical W7 type abundances for SNe Ia [16, 72, 111]  $^{56}\text{Fe}$  from SNe Ia amounts to about 55% of the total  $^{56}\text{Fe}$ . Larger frequencies would increase this contribution. Other estimates for the contributions to Fe and Fe-group elements from SNe II and SNe Ia are  $\sim 1/3$  and  $\sim 2/3$ , respectively [115]. Other

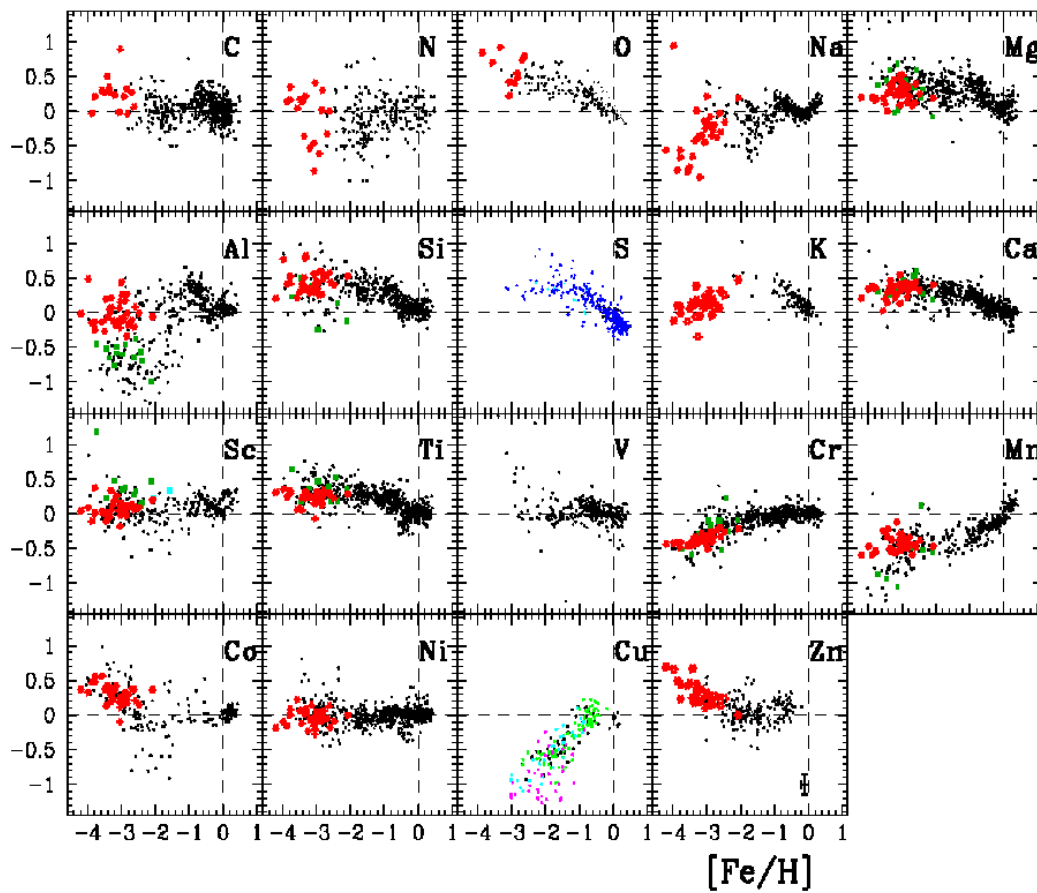


**Figure 5.2:** Abundance ratios  $[X/Fe]$  for various elements from C to Zn as a function of metallicity  $[Fe/H]$  in stars of the Milky way. Small data points represent various observational sources collected by Prantzos (2005, private communication), large data points at low metallicity are from a recent VLT survey [29]. A typical uncertainty is indicated by the error bar in the last frame. (Figure courtesy of N. Prantzos).

Fe-group elements are co-produced with Fe. Their ratio could be different in SNe Ia and SNe II and could be dependent on metallicities as well. This would reflect the evolution of  $[X/Fe]$ . The fact that  $[(Sc, V, Cr, Co, Ni, Zn)/Fe]$  remains constant and equal to its solar value for metallicities down to about -2, indicates that both SNe Ia and II/Ibc reproduce these elements on average in solar proportions as discussed above. Especially the abundances of Sc and Zn can now be explained by the effect of neutrinos in the innermost ejected zones of SNe II. Lower metallicity effects remain to be discussed.

*Alpha elements:* Alpha elements (O, Ne, Mg, Si, S, Ar, Ca) are enhanced in comparison to Fe in SNe II (as seen in low metallicity stars and expected from Section 4.3). To obtain solar abundance ratios for combined nucleosynthesis products near solar metallicity, this overabundance of alpha elements in SNe II has to be compensated by a higher Fe to alpha element ratio in SNe Ia (as seen above). The ratio of alpha elements to Fe,  $[\alpha/Fe]$ , is found to be constant above its solar value at low metallicities and to slowly decline to the solar value at about  $[Fe/H]=-1$ .

*Indirect metallicity effects:* The evolution of a single massive star, i.e. its explosion mechanism and therefore its nucleosynthesis, is determined by the core size which in turn depends on its initial mass, rotation, and metallicity. For a given initial mass the mass of the C-O core decreases with increasing metallicity due to stronger mass loss (Figure 5.1 and [63]). This has the effect that with decreasing metallicity in galactic evolution the explosive nucleosynthesis results are shifted towards those of larger C-O cores (or if we speak in simple terms the explosive nucleosynthesis products of more massive supernovae start to dominate).

While the typical explosion energy of a core collapse supernovae is of the order of  $10^{51}$  erg, very probably individual events will show variations. Studies of explosions due to neutrino absorption exhibit a twofold behavior (Figure 5.1): the explosion energy increases steadily with progenitor mass, peaking around progenitor masses of  $\sim 25 M_{\odot}$ , with a fast decline thereafter. At progenitors of about  $\sim 40 M_{\odot}$  no explosions are observed, corresponding to a direct black hole formation. If one combines this apparent increase of explosion energy with progenitor mass with the metallicity effect discussed above, one expects on average an increase in explosion energy for the core collapse supernovae contributing to very low metallicity galactic evolution. This would alter nucleosynthesis products on average similar to the discussion of hypernovae above, i.e. higher ratios of  $[(Zn, Co, V)/Fe]$  and lower ratios of  $[(Mn, Cr)/Fe]$ .

*V, Cr, Mn, Co, and Zn:* Mn seems on average to be somewhat underproduced below  $[Fe/H]=-1$  (i.e. by SNe II) and overproduced by SNe Ia in order to attain solar values at  $[Fe/H]=0$ . All the other elements show typically a solar behavior down to  $[Fe/H]=-3$ . At very low metallicities the deviations which are discussed in the previous paragraph occur. That is, we seem to see explosive nucleosynthesis results of explosions with increasing energy. There are three explanations which might act in combination: (a) the implicit metallicity effect discussed above, (b) hypernova nucleosynthesis as first explosive nucleosynthesis events, and (c) correlated inhomogeneities. Metallicities of  $[Fe/H]=-3$  can be attained if a single supernova pollutes pristine material of the order of  $10^4 M_{\odot}$ . At such early times the interstellar medium is not well mixed. We could just see the effects of single supernovae/hypernovae for  $[Fe/H]<-3$ . As with increasing explosion energy, the amount of interstellar medium (mostly H) with which the ejecta are mixed increases, higher explosion energies cause smaller  $[Fe/H]$ . Thus, one would also expect increasing deviations of V, Cr, Mn, Co, and Zn just as observed.

*Cu, N, Na, Al:* These are elements where secondary processes play an important role. Cu is dominated by the s-process; N, Na, and Al have contributions from the CNO, NeNaMg, and MgAlSi cycles, respectively. These are processes acting in H- and He-burning shells and in parts of stellar wind ejecta which have not been discussed here.

*Sr, Y, Zr:* The production of elements beyond iron is traditionally attributed to two neutron capture processes: the s-process (slow process) and the r-process (rapid process). The s-process occurs in He-burning as a secondary process, building about half the nuclides from Fe to Bi, in particular the elements Sr, Y, Zr, Ba to Nd, and Pb (corresponding to the three main s-process peaks). Asymptotic giant branch (AGB) star nucleosynthesis for a variety of metallicities and  $^{13}C$  pocket efficiencies show a strong decrease in the production efficiency with decreasing metallicity [141]. Summing all the contributions to the elements Sr, Y, and Zr there are large fractions of the observed Sr, Y, and Zr missing. They are assumed to be of primary origin, independent of the r-process, and result from all massive stars [141]. The  $\nu p$ -process discussed in Section 4.4 could explain their origin.

### 5.3. Concluding Outlook

---

At very early times, when the interstellar medium is essentially pristine, we will see the ejecta of individual supernovae where the amount of H with which these ejecta mix is dependent on the explosion energy and the stellar progenitor mass. At these times (i.e. at low metallicities) the observed scatter is also large. The scatter becomes smaller with increasing metallicities where the average signature of supernovae integrated over the initial mass function (IMF; essentially giving the mass distribution for star formation) is seen. While the comparison of supernova yields to observed abundances from hyper metal-poor stars can test individual supernova events, nucleosynthesis predictions for a series of progenitor masses can test IMF integrated samples. We will calculate nucleosynthesis yields for a series of pre-collapse models with different main sequence masses. These yields will be used in galactic evolution studies.

# 6

## Summary and Outlook

---

Presently, self-consistent core collapse supernova simulations in 1D do not lead to successful explosions while 2D models show some promise. Remaining uncertainties in neutrino opacities and/or the expected strong influence of convection (due to hydrodynamic instabilities caused by entropy gradients and/or rotation and magnetic fields) are likely to change this result. They may lead either to higher neutrino luminosities or higher efficiencies of neutrino energy deposition via neutrino and antineutrino captures on nucleons. In order to examine the accompanied nucleosynthesis in 1D calculations of successful explosions, simulations with variations in neutrino scattering cross sections on nucleons and/or neutrino and antineutrino captures on neutrons and protons were performed. In both cases successful explosions emerge with an interesting evolution of the  $Y_e$  gradient in the innermost ejecta.

This dissertation contains nucleosynthesis calculations based on these core collapse models which ameliorate two of the traditionally inherent uncertainties in core collapse supernova nucleosynthesis. First, the location of the mass cut now emerges from the simulation, allowing predictions for the total amount of Fe ejected. And second, the electron fraction in the innermost ejecta is now consistently set by all weak interactions contributing to changes of  $Y_e$ . The nucleosynthesis calculations are done in a postprocessing framework.

The detailed nucleosynthesis calculations with a consistent treatment of all weak interactions show an electron fraction  $Y_e > 0.5$ , i.e. a slightly proton-rich environment with relatively high entropies of up to  $\sim 50 k_B$  per nucleon. This causes complete Si-burning with an alpha-rich (and proton-rich) freeze-out. About  $0.0007 M_\odot$  of hydrogen remains in the innermost ejecta and does not stem from mixing this matter in from the hydrogen envelope. Such a proton-rich environment at relatively high entropies permits to produce also nuclei beyond  $A=64$  with a major contribution to  $^{64}\text{Zn}$ .

In addition, we find improvements within the Fe-group. The strong overabundances of  $^{58,62}\text{Ni}$  found in previous (too neutron-rich) environments are reduced.  $^{45}\text{Sc}$  and  $^{49}\text{Ti}$  are enhanced to permit predictions closer to solar proportions. Especially the emergence of  $^{45}\text{Sc}$  seems to be a solution to the previously not understood abundance of this only stable isotope of Sc. This discussion is also of interest with respect to  $^{44}\text{Ti}$ , made in the alpha-rich freeze-out in the inner explosive ejecta.  $^{44}\text{Ti}$  is sensitive to  $Y_e$  and reduced in the mass range where  $^{45}\text{Sc}$  is high. This will influence the overall predictions of  $^{44}\text{Ti}$ .

The observed production of nuclei with  $A > 64$  is due to an  $\nu p$ -process like process for which we coined the name  $\nu p$ -process. This process is expected to take place in all core collapse supernovae, when hot and proton-rich matter is ejected under the influence of a strong neutrino irradiation. It operates in the innermost ejecta which is sensitive to the details of the explosion. The final amount of ejected matter also depends on fallback but mixing may additionally complicate the situation. The studies on the  $\nu p$ -process in this thesis show that elements between Zn and Sr should be co-produced with Sr, making it a candidate for the suggested light element primary process. This novel process is also a possible candidate to explain the origin of the solar abundances of  $^{92,94}\text{Mo}$  and  $^{96,98}\text{Ru}$  and the large observed abundance of Sr seen in a hyper metal-poor star.

Cosmology and the early universe witness the abundances of the light elements such as hydrogen, deuterium, helium, and lithium. The remain vast majority of heavy elements originates from the stellar components (supernovae of type Ia and type II) in galaxies. Nucleosynthesis predictions are vital to the growing field of galactic chemical evolution and can also serve as test for the supernova mechanism. Hence, the nucleosynthesis studies of this thesis will be extended to a large range of progenitor masses and metallicities. From this, the effects of the initial metallicity on the stellar evolution, explosive processing, and the final nucleosynthesis can be investigated. Nucleosynthesis calculations for a range of progenitor masses and metallicities will also provide standard core collapse supernova yields which are important to other fields such as galactic evolution.





---

## Bibliography

- [1] C. Angulo, M. Arnould, M. Rayet, P. Descouvemont, D. Baye, C. Leclercq-Willain, A. Coc, S. Barhoumi, P. Aguer, C. Rolfs, R. Kunz, J. W. Hammer, A. Mayer, T. Paradellis, S. Kossionides, C. Chronidou, K. Spyrou, S. Degl'Innocenti, G. Fiorentini, B. Ricci, S. Zavatarelli, C. Providencia, H. Wolters, J. Soares, C. Gram, J. Rahighi, A. Shotter, and M. Laméhi Rachti. A compilation of charged-particle induced thermonuclear reaction rates. *Nucl. Phys. A*, 656:3–183, 1999.
- [2] W. Aoki, H. Ando, S. Honda, M. Iye, H. Izumiura, T. Kajino, E. Kambe, S. Kawanomoto, K. Noguchi, K. Okita, K. Sadakane, B. Sato, I. Shelton, M. Takada-Hidai, Y. Takeda, E. Watanabe, and M. Yoshida. Chemical Composition of Carbon-Rich, Very Metal-Poor Subgiant LP 625-44 Observed with the Subaru/HDS. *PASJ*, 54:427–449, 2002.
- [3] D. Argast, M. Samland, F.-K. Thielemann, and O. E. Gerhard. Implications of O and Mg abundances in metal-poor halo stars for stellar iron yields. *A&A*, 388:842–860, 2002.
- [4] D. Argast, M. Samland, F.-K. Thielemann, and Y.-Z. Qian. Neutron star mergers versus core-collapse supernovae as dominant r-process sites in the early Galaxy. *A&A*, 416:997–1011, 2004.
- [5] W. D. Arnett. Mass Dependence in Gravitational Collapse of Stellar Cores. *Canadian Journal of Physics*, 45:1621–+, 1967.
- [6] M. Arnould and S. Goriely. The p-process of stellar nucleosynthesis: astrophysics and nuclear physics status. *Phys. Rep.*, 384:1–84, 2003.
- [7] M. B. Aufderheide, E. Baron, and F.-K. Thielemann. Shock waves and nucleosynthesis in type II supernovae. *ApJ*, 370:630–642, 1991.
- [8] A. B. Balantekin and G. M. Fuller. Supernova neutrino nucleus astrophysics. *J. Phys. G Nucl. Phys.*, 29:2513–2522, 2003.
- [9] Z. Y. Bao, H. Beer, F. Käppeler, F. Voss, K. Wisshak, and T. Rauscher. Neutron Cross Sections for Nucleosynthesis Studies. *At. Data Nucl. Data Tables*, 76:70–154, 2000.
- [10] Z. Y. Bao and F. Käppeler. Neutron Capture Cross Sections for s-Process Studies. *At. Data Nucl. Data Tables*, 36:411–+, 1987.
- [11] A. M. Beloborodov. Nuclear Composition of Gamma-Ray Burst Fireballs. *ApJ*, 588:931–944, 2003.
- [12] H. A. Bethe. Supernova mechanisms. *Rev. Mod. Phys.*, 62:801–866, 1990.
- [13] H. A. Bethe and J. R. Wilson. *ApJ*, 295:14, 1985.
- [14] J.M. Blatt and V.F. Weisskopf. *Theoretical Nuclear Physics*. John Wiley & Sons, Inc., New York, 1952.
- [15] F. Brachitz. *Neutron-Rich Nucleosynthesis in Chandrasekhar Mass Models of Type Ia Supernovae*. PhD thesis, University of Basel, 2003.

- [16] F. Brachwitz, D. J. Dean, W. R. Hix, K. Iwamoto, K. Langanke, G. Martínez-Pinedo, K. Nomoto, M. R. Strayer, F. Thielemann, and H. Umeda. The role of electron captures in Chandrasekhar-mass models for type Ia supernovae. *ApJ*, 536:934–947, 2000.
- [17] E. Bravo, I. Dominguez, J. Isern, R. Canal, P. Hoefflich, and J. Labay. On the photometric homogeneity of Type Ia supernovae. *A&A*, 269:187–194, 1993.
- [18] S. W. Bruenn. Stellar core collapse: Numerical model and infall epoch. *ApJS*, 58:771–841, 1985.
- [19] S. W. Bruenn. The prompt-shock supernova mechanism. I - The effect of the free-p neutron mass fraction and the neutrino transport algorithm. *ApJ*, 340:955–965, 1989.
- [20] S. W. Bruenn, E. A. Raley, and A. Mezzacappa. Fluid Stability Below the Neutrinospheres of Supernova Progenitors and the Dominant Role of Lepto-Entropy Fingers. *astro-ph/0404099*, 2004.
- [21] R. Buras, M. Rampp, H.-T. Janka, and K. Kifonidis. Improved Models of Stellar Core Collapse and Still No Explosions: What Is Missing? *Phys. Rev. Lett.*, 90(24):241101–+, 2003.
- [22] R. Buras, M. Rampp, H.-T. Janka, and K. Kifonidis. Two-dimensional hydrodynamic core-collapse supernova simulations with spectral neutrino transport. I. Numerical method and results for a 15  $M_{\odot}$  star. *A&A*, 447:1049–1092, 2006.
- [23] E. M. Burbidge, G. R. Burbidge, W. A. Fowler, and F. Hoyle. Synthesis of the Elements in Stars. *Rev. Mod. Phys.*, 29:547, 1957.
- [24] A. Burrows. Neutrinos From Supernova Explosions. *Ann. Rev. Nucl. Part. Sci.*, 40:181, 1990.
- [25] A. Burrows. Neutrino-matter interactions in the context of core-collapse supernovae. *Prog. Part. Nucl. Phys.*, 46:59–71, 2001.
- [26] A. Burrows, J. Hayes, and B. A. Fryxell. On the Nature of Core-Collapse Supernova Explosions. *ApJ*, 450:830, 1995.
- [27] A. G. W. Cameron. Stellar evolution, nuclear astrophysics, and nucleogenesis. Report CRL-41, Chalk River, 1957.
- [28] G. R. Caughlan and W. A. Fowler. Thermonuclear Reaction Rates V. *At. Data Nucl. Data Tables*, 40:283–+, 1988.
- [29] R. Cayrel, E. Depagne, M. Spite, V. Hill, F. Spite, P. François, B. Plez, T. Beers, F. Primas, J. Andersen, B. Barbuy, P. Bonifacio, P. Molaro, and B. Nordström. First stars v - abundance patterns from c to zn and supernova yields in the early galaxy. *A&A*, 416:1117–1138, 2004.
- [30] A. Chieffi and M. Limongi. The explosive yields produced by the first generation of core collapse supernovae and the chemical composition of extremely metal poor stars. *ApJ*, 577:281–294, 2002.
- [31] A. Chieffi and M. Limongi. Explosive Yields of Massive Stars from  $Z = 0$  to  $Z = Z_{\text{solar}}$ . *ApJ*, 608:405–410, 2004.
- [32] N. Christlieb, M. S. Bessel, T. C. Beers, B. Gustafsson, A. Korn, P. S. Barklem, T. Karlsson, M. Mizuno-Wiedner, and S. Rossi. A stellar relic from the early milky way. *Nature*, 419:904–906, 2002.
- [33] D. D. Clayton. *Principles of Stellar Evolution and Nucleosynthesis*. McGraw-Hill, New York, 1968.
- [34] S. A. Colgate and R. H. White. Theoretical behavior of the initial supernova light emission. *AJ*, 69:537, 1964.
- [35] S. A. Colgate and R. H. White. The hydrodynamic behavior of supernovae explosions. *ApJ*, 143:626, 1966.
- [36] J. Cooperstein. Neutrinos in supernovae. *Phys. Rep.*, 163:95–126, 1988.
- [37] V. Costa, M. Rayet, R. A. Zappalà, and M. Arnould. The synthesis of the light Mo and Ru isotopes: how now, no need for an exotic solution? *A&A*, 358:L67–L70, 2000.

- [38] J. Cowan, F.-K. Thielemann, and J. Truran. *Nuclear Evolution of the Universe*. in preparation.
- [39] J. J. Cowan, C. Sneden, T. C. Beers, J. E. Lawler, J. Simmerer, J. W. Truran, F. Primas, J. Collier, and S. Burles. Hubble Space Telescope Observations of Heavy Elements in Metal-Poor Galactic Halo Stars. *ApJ*, 627:238–250, 2005.
- [40] J. J. Cowan, F.-K. Thielemann, and J. W. Truran. *Phys. Repts.*, 208:267, 1991.
- [41] N. Dauphas, T. Rauscher, B. Marty, and L. Reisberg. Short-lived  $p$ -nuclides in the early solar system and implications on the nucleosynthetic role of X-ray binaries. *Nucl. Phys. A*, 719:287c–295c, 2003.
- [42] G. V. Domogatskii, R. A. Eramzhian, and D. K. Nadezhin. Production of the light elements due to neutrinos emitted by collapsing stellar cores. *Ap. Space Sci.*, 58:273–299, 1978.
- [43] G. V. Domogatskii and D. K. Nadyozhin. Neutrino induced production of bypassed elements. *Mon. Not. R. Astron. Soc.*, 178:33P–36P, 1977.
- [44] B.T. Fischer. . PhD thesis, University of Basel, 2009. in preparation.
- [45] W. A. Fowler, G. R. Caughlan, and B. A. Zimmerman. Thermonuclear Reaction Rates. *ARA&A*, 5:525–+, 1967.
- [46] P. François, F. Matteucci, R. Cayrel, M. Spite, F. Spite, and C. Chiappini. The evolution of the Milky Way from its earliest phases: Constraints on stellar nucleosynthesis. *A&A*, 421:613–621, 2004.
- [47] A. Frebel, W. Aoki, N. Christlieb, H. Ando, M. Asplund, P. S. Barklem, T. C. Beers, K. Eriksson, C. Fechner, M. Y. Fujimoto, S. Honda, T. Kajino, T. Minezaki, K. Nomoto, J. E. Norris, S. G. Ryan, M. Takada-Hidai, S. Tsangarides, and Y. Yoshii. Nucleosynthetic signatures of the first stars. *Nature*, 434:871–873, 2005.
- [48] C. Fröhlich, P. Hauser, M. Liebendörfer, G. Martínez-Pinedo, E. Bravo, W. R. Hix, N. T. Zinner, and F.-K. Thielemann. The Innermost Ejecta of Core Collapse Supernovae. *Nucl. Phys. A*, 758:27, 2005.
- [49] C. Fröhlich, P. Hauser, M. Liebendörfer, G. Martínez-Pinedo, F.-K. Thielemann, E. Bravo, N. T. Zinner, W. R. Hix, K. Langanke, A. Mezzacappa, and K. Nomoto. Composition of the Innermost Supernova Ejecta. *ApJ*, 637:415–426, 2006.
- [50] C. Fröhlich, G. Martínez-Pinedo, M. Liebendörfer, F.-K. Thielemann, E. Bravo, W. R. Hix, K. Langanke, and N. T. Zinner. Neutrino-Induced Nucleosynthesis of  $A > 64$  Nuclei: The  $\nu p$  Process. *Phys. Rev. Lett.*, 96(14):142502–+, 2006.
- [51] C. L. Fryer and M. S. Warren. The Collapse of Rotating Massive Stars in Three Dimensions. *ApJ*, 601:391–404, 2004.
- [52] S.-i. Fujimoto, M.-a. Hashimoto, K. Arai, and R. Matsuba. Nucleosynthesis inside an Accretion Disk and Disk Winds Related to Gamma-Ray Bursts. *ApJ*, 614:847–857, 2004.
- [53] G. M. Fuller, W. A. Fowler, and M. J. Newman. Stellar weak interaction rates for intermediate-mass nuclei. ii -  $a = 21$  to  $a = 60$ . *ApJ*, 252:715, 1982.
- [54] G. M. Fuller, W. A. Fowler, and M. J. Newman. Stellar weak interaction rates for intermediate mass nuclei. iii - rate tables for the free nucleons and nuclei with  $a = 21$  to  $a = 60$ . *ApJS*, 48:279, 1982.
- [55] G. M. Fuller, W. A. Fowler, and M. J. Newman. Stellar weak interaction rates for intermediate-mass nuclei. iv - interpolation procedures for rapidly varying lepton capture rates using effective  $\log(ft)$ -values. *ApJ*, 293:1, 1985.
- [56] G. M. Fuller and B. S. Meyer. Neutrino Capture and Supernova Nucleosynthesis. *ApJ*, 453:792–+, 1995.
- [57] R. G. Gratton and C. Sneden. Abundances of elements of the Fe-group in metal-poor stars. *A&A*, 241:501–525, 1991.

- [58] D. A. Green and F. R. Stephenson. Historical Supernovae. In K. Weiler, editor, *LNP Vol. 598: Supernovae and Gamma-Ray Bursters*, pages 7–19, 2003.
- [59] W. C. Haxton, K. Langanke, Y. Z. Qian, and P. Vogel. Neutrino-induced nucleosynthesis and the site of the r- process. *Phys. Rev. Lett.*, 78:2694–2697, 1997.
- [60] T. Hayakawa, N. Iwamoto, T. Shizuma, T. Kajino, H. Umeda, and K. Nomoto. Evidence for Nucleosynthesis in the Supernova  $\gamma$  Process: Universal Scaling for  $p$  Nuclei. *Phys. Rev. Lett.*, 93, 2004.
- [61] A. Heger, C. L. Fryer, S. E. Woosley, N. Langer, and D. H. Hartmann. How Massive Single Stars End Their Life. *ApJ*, 591:288–300, 2003.
- [62] M. Herant, W. Benz, W. R. Hix, C. L. Fryer, and S. A. Colgate. Inside the supernova: A powerful convective engine. *ApJ*, 435:339–361, 1994.
- [63] R. Hirschi, G. Meynet, and A. Maeder. GRB progenitors at low metallicities. *ArXiv Astrophysics e-prints*, 2006.
- [64] W. R. Hix, O. E. B. Messer, A. Mezzacappa, M. Liebendörfer, J. Sampaio, K. Langanke, D. J. Dean, and G. Martínez-Pinedo. The consequences of nuclear electron capture in core collapse supernovae. *Phys. Rev. Lett.*, 91, 2003.
- [65] W. R. Hix and B. S. Meyer. Thermonuclear kinetics in astrophysics. *Nucl. Phys. A*, 777:188–207, 2006.
- [66] R. D. Hoffman, S. E. Woosley, G. M. Fuller, and B. S. Meyer. Production of the Light p-Process Nuclei in Neutrino-driven Winds. *ApJ*, 460:478–+, 1996.
- [67] P. Höflich. Physics of type Ia supernovae. *Nuclear Physics A*, 777:579–600, 2006.
- [68] S. Honda, W. Aoki, H. Ando, H. Izumiura, T. Kajino, E. Kambe, S. Kawanomoto, K. Noguchi, K. Okita, K. Sadakane, B. Sato, M. Takada-Hidai, Y. Takeda, E. Watanabe, T. C. Beers, J. E. Norris, and S. G. Ryan. Spectroscopic Studies of Extremely Metal-Poor Stars with the Subaru High Dispersion Spectrograph. I. Observational Data. *ApJS*, 152:113–128, 2004.
- [69] C. J. Horowitz. Weak magnetism for antineutrinos in supernovae. *Phys. Rev. D*, 65, 2002.
- [70] I. J. Iben. Single and binary star evolution. *ApJS*, 76:55–114, 1991.
- [71] N. Itoh, H. Totsuji, S. Ichimaru, and H. E. Dewitt. Enhancement of thermonuclear reaction rate due to strong screening. II - Ionic mixtures. *ApJ*, 234:1079–1084, 1979.
- [72] K. Iwamoto, F. Brachwitz, K. Nomoto, N. Kishimoto, H. Umeda, W. R. Hix, and F. Thielemann. Nucleosynthesis in Chandrasekhar Mass Models for Type IA Supernovae and Constraints on Progenitor Systems and Burning-Front Propagation. *ApJS*, 125:439–462, 1999.
- [73] N. Iwamoto, H. Umeda, N. Tominaga, K. Nomoto, and K. Maeda. The First Chemical Enrichment in the Universe and the Formation of Hyper Metal-Poor Stars. *Science*, 309(5733):451, 2005.
- [74] H.-T. Janka, R. Buras, F.S. Kitaura Joyanes, A. Marek, M. Rampp, and L. Scheek. Neutrino-driven supernovae: An accretion instability in a nuclear physics controlled environment. *Nucl. Phys. A*, 758:19c–26c, 2005.
- [75] H.-T. Janka, R. Buras, and M. Rampp. The mechanism of core-collapse supernovae and the ejection of heavy elements. *Nucl. Phys. A*, 718:269–276, 2003.
- [76] H.-Th. Janka and W. Hillebrandt. *A&A*, 224:49, 1989.
- [77] H.-Th. Janka and E. Müller. Neutrino heating, convection, and the mechanism of Type-II supernova explosions. *A&A*, 306:167, 1996.
- [78] G. C. Jordan IV and B. S. Meyer. Nucleosynthesis in fast expansion of high-entropy, proton-rich matter. *ApJ*, 617:L131–L134, 2004.

- [79] W. Keil, H.-Th. Janka, and E. Müller. Ledoux Convection in Protoneutron Stars—A Clue to Supernova Nucleosynthesis? *ApJ*, 473:L111+, 1996.
- [80] K. Kifonidis, T. Plewa, H.-T. Janka, and E. Müller. Non-spherical core collapse supernovae. I. Neutrino-driven convection, Rayleigh-Taylor instabilities, and the formation and propagation of metal clumps. *A&A*, 408:621–649, 2003.
- [81] H. V. Klapdor, J. Metzinger, and T. Oda. Beta-Decay Half-Lives of Neutron-Rich Nuclei. *At. Data Nucl. Data Tables*, 31:81–+, 1984.
- [82] M. Koshiba. Observational neutrino astrophysics. *Phys. Rep.*, 220:229–381, 1992.
- [83] K. Langanke and E. Kolbe. Neutrino-induced charged-current reaction rates for r-process nuclei. *At. Data Nucl. Data Tables*, 79:293–315, 2001.
- [84] K. Langanke and E. Kolbe. Neutrino-induced neutral-current reaction rates for r-process nuclei. *At. Data Nucl. Data Tables*, 82:191–209, 2002.
- [85] K. Langanke and G. Martínez-Pinedo. Rate Tables for the Weak Processes of pf-SHELL Nuclei in Stellar Environments. *At. Data Nucl. Data Tables*, 79:1–46, 2001.
- [86] K. Langanke, G. Martínez-Pinedo, O. E. B. Messer, J. M. Sampaio, D. J. Dean, W. R. Hix, A. Mezzacappa, M. Liebendörfer, H.-Th. Janka, and M. Rampp. Electron capture rates on nuclei and implications for stellar core collapse. *Phys. Rev. Lett.*, 90, 2003.
- [87] J. M. Lattimer and F. D. Swesty. A generalized equation of state for hot, dense matter. *Nucl. Phys. A*, 535:331–376, 1991.
- [88] M. Liebendörfer, O. E. B. Messer, A. Mezzacappa, S. W. Bruenn, C. Y. Cardall, and F.-K. Thielemann. A Finite Difference Representation of Neutrino Radiation Hydrodynamics in Spherically Symmetric General Relativistic Spacetime. *ApJS*, 150:263–316, 2004.
- [89] M. Liebendörfer, A. Mezzacappa, and F.-K. Thielemann. Conservative general relativistic radiation hydrodynamics in spherical symmetry and comoving coordinates. *Phys. Rev. D*, 63(10):104003–+, 2001.
- [90] M. Liebendörfer, S. Rosswog, and F.-K. Thielemann. An Adaptive Grid, Implicit Code for Spherically Symmetric, General Relativistic Hydrodynamics in Comoving Coordinates. *ApJS*, 141:229–246, 2002.
- [91] M. Liebendörfer. Fifty-Nine Reasons for a Supernova to not Explode. *astro-ph/0405029*, 2004.
- [92] M. Liebendörfer, A. Mezzacappa, O. E. B. Messer, G. Martínez-Pinedo, W. R. Hix, and F.-K. Thielemann. The neutrino signal in stellar core collapse and postbounce evolution. *Nuclear Physics A*, 719:144–+, 2003.
- [93] M. Liebendörfer, A. Mezzacappa, F.-K. Thielemann, O. E. B. Messer, W. R. Hix, and S. W. Bruenn. Probing the gravitational well: No supernova explosion in spherical symmetry with general relativistic boltzmann neutrino transport. *Phys. Rev. D*, 63:103004–+, 2001.
- [94] K. Lodders. Solar System Abundances and Condensation Temperatures of the Elements. *ApJ*, 591:1220–1247, 2003.
- [95] R. Mayle and J. R. Wilson. Supernovae from collapse of oxygen-magnesium-neon cores. *ApJ*, 334:909–926, 1988.
- [96] O. E. B. Messer, A. Mezzacappa, S. W. Bruenn, and M. W. Guidry. A Comparison of Boltzmann and Multigroup Flux-limited Diffusion Neutrino Transport during the Postbounce Shock Reheating Phase in Core-Collapse Supernovae. *ApJ*, 507:353–360, 1998.
- [97] B. S. Meyer. r-Process Nucleosynthesis without Excess Neutrons. *Phys. Rev. Lett.*, 89(23):231101–+, 2002.
- [98] B. S. Meyer, G. C. McLaughlin, and G. M. Fuller. Neutrino capture and r-process nucleosynthesis. *Phys. Rev. C*, 58:3696–3710, 1998.

- [99] G. Meynet and A. Maeder. Stellar evolution with rotation. XI. Wolf-Rayet star populations at different metallicities. *A&A*, 429:581–598, 2005.
- [100] A. Mezzacappa and S. W. Bruenn. A numerical method for solving the neutrino boltzmann equation coupled to spherically symmetric stellar core collapse. *ApJ*, 405:637, 1993.
- [101] A. Mezzacappa and S. W. Bruenn. Stellar core collapse - a boltzmann treatment of neutrino-electron scattering. *ApJ*, 410:740, 1993.
- [102] A. Mezzacappa, A. C. Calder, S. W. Bruenn, J. M. Blondin, M. W. Guidry, M. R. Strayer, and A. S. Umar. An Investigation of Neutrino-driven Convection and the Core Collapse Supernova Mechanism Using Multi-group Neutrino Transport. *ApJ*, 495:911, 1998.
- [103] A. Mezzacappa, M. Liebendörfer, O. E. B. Messer, W. R. Hix, F.-K. Thielemann, and S. W. Bruenn. Simulation of the spherically symmetric stellar core collapse, bounce, and postbounce evolution of a star of 13 solar masses with boltzmann neutrino transport, and its implications for the supernova mechanism. *Phys. Rev. Lett.*, 86:1935–1938, 2001.
- [104] A. Mezzacappa and O. E. B. Messer. Neutrino transport in core collapse supernovae. *J. Comp. Appl. Math.*, 109:281–319, 1999.
- [105] E. S. Myra and S. A. Bludman. Neutrino transport and the prompt mechanism for type II supernovae. *ApJ*, 340:384–395, 1989.
- [106] E. S. Myra and A. Burrows. Neutrinos from type II supernovae - The first 100 milliseconds. *ApJ*, 364:222–231, 1990.
- [107] T. Nakamura, H. Umeda, K. Iwamoto, K. Nomoto, M. Hashimoto, W. R. Hix, and F. Thielemann. Explosive Nucleosynthesis in Hypernovae. *ApJ*, 555:880–899, 2001.
- [108] T. Nakamura, H. Umeda, K. Nomoto, F. Thielemann, and A. Burrows. Nucleosynthesis in Type II Supernovae and the Abundances in Metal-poor Stars. *ApJ*, 517:193–208, 1999.
- [109] K. Nomoto and M. Hashimoto. Presupernova evolution of massive stars. *Phys. Rep.*, 163:13, 1988.
- [110] K. Nomoto, M. Hashimoto, T. Tsujimoto, F.-K. Thielemann, N. Kishimoto, Y. Kubo, and N. Nakasato. Nucleosynthesis in type II supernovae. *Nucl. Phys. A*, 616:79–90, 1997.
- [111] K. Nomoto, F.-K. Thielemann, and K. Yokoi. *ApJ*, 286:644, 1984.
- [112] K. Nomoto, N. Tominaga, H. Umeda, C. Kobayashi, and K. Maeda. Nucleosynthesis yields of core-collapse supernovae and hypernovae, and galactic chemical evolution. *Nuclear Physics A*, 777:424–458, 2006.
- [113] B. Paczynski. Are Gamma-Ray Bursts in Star-Forming Regions? *ApJ*, 494:L45+, 1998.
- [114] M. M. Phillips. The absolute magnitudes of Type IA supernovae. *ApJ*, 413:L105–L108, August 1993.
- [115] N. Prantzos. The early phases of Milky Way’s chemical evolution. *Nuclear Physics A*, 758:249–258, 2005.
- [116] J. Pruet, R. D. Hoffman, S. E. Woosley, H.-T. Janka, and R. Buras. Nucleosynthesis in Early Supernova Winds. II. The Role of Neutrinos. *ApJ*, 644:1028–1039, 2006.
- [117] J. Pruet, T. A. Thompson, and R. D. Hoffman. Nucleosynthesis in Outflows from the Inner Regions of Collapsars. *ApJ*, 606:1006–1018, 2004.
- [118] J. Pruet, S. E. Woosley, R. Buras, H.-T. Janka, and R. D. Hoffman. Nucleosynthesis in the hot convective bubble in core-collapse supernovae. *ApJ*, 623:325, 2005.
- [119] Y. Z. Qian, W. C. Haxton, K. Langanke, and P. Vogel. Neutrino-induced neutron spallation and supernova r-process nucleosynthesis. *Phys. Rev. C*, 55:1532–1544, 1997.
- [120] Y.-Z. Qian and S. E. Woosley. Nucleosynthesis in Neutrino-driven Winds. I. The Physical Conditions. *ApJ*, 471:331, 1996.

- [121] M. Rampp and H.-Th. Janka. Spherically symmetric simulation with boltzmann neutrino transport of core collapse and post-bounce evolution of a 15 Msolar star. *ApJ*, 539:L33–L36, 2000.
- [122] T. Rauscher, A. Heger, R. D. Hoffman, and S. E. Woosley. Nucleosynthesis in massive stars with improved nuclear and stellar physics. *ApJ*, 576:323–348, 2002.
- [123] T. Rauscher and F.-K. Thielemann. Astrophysical reaction rates from statistical model calculations. *At. Data Nucl. Data Tables*, 75:1–352, 2000.
- [124] H. Schatz, A. Aprahamian, V. Barnard, L. Bildsten, A. Cumming, M. Ouellette, T. Rauscher, F.-K. Thielemann, and M. Wiescher. End point of the rp process on accreting neutron stars. *Phys. Rev. Lett.*, 86:3471, 2001.
- [125] H. Shen, H. Toki, K. Oyamatsu, and K. Sumiyoshi. Relativistic equation of state of nuclear matter for supernova and neutron star. *Nucl. Phys. A*, 637:435–450, 1998.
- [126] H. Shen, H. Toki, K. Oyamatsu, and K. Sumiyoshi. Relativistic Equation of State of Nuclear Matter for Supernova Explosion. *Prog. Theor. Phys.*, 100:1013–1031, 1998.
- [127] C. Sneden and J. J. Cowan. Genesis of the Heaviest Elements in the Milky Way Galaxy. *Science*, 299(5603):70–75, 2003.
- [128] C. Sneden, J. J. Cowan, J. E. Lawler, I. I. Ivans, S. Burles, T. C. Beers, F. Primas, V. Hill, J. W. Truran, G. M. Fuller, B. Pfeiffer, and K. Kratz. The Extremely Metal-poor, Neutron Capture-rich Star CS 22892-052: A Comprehensive Abundance Analysis. *ApJ*, 591:936–953, 2003.
- [129] R. Surman, G. C. McLaughlin, and W. R. Hix. Nucleosynthesis in the Outflow from Gamma-Ray Burst Accretion Disks. *ApJ*, 643:1057–1064, 2006.
- [130] K. Takahashi, J. Witt, and H.-T. Janka. Nucleosynthesis in neutrino-driven winds from protoneutron stars II. The r-process. *A&A*, 286:857–869, 1994.
- [131] K. Takahashi, M. Yamada, and T. Kondoh. Beta-Decay Half-Lives Calculated on the Gross Theory. *At. Data Nucl. Data Tables*, 12:101–+, 1973.
- [132] M. Terasawa, K. Sumiyoshi, S. Yamada, H. Suzuki, and T. Kajino. r-Process Nucleosynthesis in Neutrino-driven Winds from a Typical Neutron Star with M=1.4 Msolar. *ApJ*, 578:L137–L140, 2002.
- [133] F.-K. Thielemann, M. Hashimoto, and K. Nomoto. Explosive nucleosynthesis in SN 1987A. II - Composition, radioactivities, and the neutron star mass. *ApJ*, 349:222–240, 1990.
- [134] F.-K. Thielemann, K. Nomoto, and M. Hashimoto. Core-Collapse Supernovae and Their Ejecta. *ApJ*, 460:408–436, 1996. (TNH96).
- [135] F.-K. Thielemann, K. Nomoto, and K. Yokoi. *Astr. A.*, 158:17, 1986.
- [136] C. Thompson. Accretional Heating of Asymmetric Supernova Cores. *ApJ*, 534:915–933, 2000.
- [137] T. A. Thompson, E. Quataert, and A. Burrows. Viscosity and Rotation in Core-Collapse Supernovae. *ApJ*, 620:861–877, 2005.
- [138] T[odd] A. Thompson, A[dam] Burrows, and B[radley] S. Meyer. The physics of proto-neutron star winds: Implications for r-process nucleosynthesis. *ApJ*, 562:887–908, 2001.
- [139] Todd A. Thompson, Adam Burrows, and Philip A. Pinto. Shock breakout in core-collapse supernovae and its neutrino signature. *ApJ*, 592:434–456, 2003.
- [140] F. X. Timmes, S. E. Woosley, and T. A. Weaver. Galactic chemical evolution: Hydrogen through zinc. *ApJS*, 98:617, 1995.
- [141] C. Travaglio, R. Gallino, E. Arnone, J. Cowan, F. Jordan, and C. Sneden. Galactic Evolution of Sr, Y, And Zr: A Multiplicity of Nucleosynthetic Processes. *ApJ*, 601:864–884, 2004.

- [142] H. Umeda and K. Nomoto. Nucleosynthesis of Zinc and Iron Peak Elements in Population III Type II Supernovae: Comparison with Abundances of Very Metal Poor Halo Stars. *ApJ*, 565:385–404, 2002.
- [143] H. Umeda and K. Nomoto. Variations in the Abundance Pattern of Extremely Metal-Poor Stars and Nucleosynthesis in Population III Supernovae. *ApJ*, 619:427–445, 2005.
- [144] H. Umeda, K. Nomoto, and T. Nakamura. Evolution and Nucleosynthesis of Metal-Free Massive Stars. In A. Weiss, T. G. Abel, and V. Hill, editors, *The First Stars: Proceedings of the MPA/ESO Workshop Held at Garching, Germany, 4-6 August 1999, ESO ASTROPHYSICS SYMPOSIA. ISBN 3-540-67222-2. Edited by A. Weiss, T.G. Abel, and V. Hill. Springer-Verlag, 2000, p. 150*–+, 2000.
- [145] S. van den Bergh and R. D. McClure. Redis-cussion of extragalactic supernova rates derived from Evans’s 1980-1988 observations. *ApJ*, 425:205–209, 1994.
- [146] G. Wallerstein, I. Iben, P. Parker, A. M. Boesgaard, G. M. Hale, A. E. Champagne, C. A. Barnes, F. Käppeler, V. V. Smith, R. D. Hoffman, F. X. Timmes, C. Sneden, R. N. Boyd, B. S. Meyer, and D. L. Lambert. Synthesis of the elements in stars: forty years of progress. *Rev. Mod. Phys.*, 69:995–1084, 1997.
- [147] S. Wanajo, T. Kajino, G. J. Mathews, and K. Otsuki. The r-Process in Neutrino-driven Winds from Nascent, “Compact” Neutron Stars of Core-Collapse Supernovae. *ApJ*, 554:578–586, 2001.
- [148] T. A. Weaver and S. E. Woosley. *Ann. NY Acad. Sci.*, 366:355, 1980.
- [149] J. R. Wilson and R. W. Mayle. Report on the progress of supernova research by the livermore group. *Phys. Rep.*, 227:97–111, 1993.
- [150] S. E. Woosley. Gamma-ray bursts from stellar mass accretion disks around black holes. *ApJ*, 405:273–277, 1993.
- [151] S. E. Woosley, W. D. Arnett, and D. D. Clayton. The Explosive Burning of Oxygen and Silicon. *ApJS*, 26:231–+, 1973.
- [152] S. E. Woosley, D. H. Hartmann, R. D. Hoffman, and W. C. Haxton. The nu-process. *ApJ*, 356:272–301, 1990.
- [153] S. E. Woosley, A. Heger, and T. A. Weaver. The evolution and explosion of massive stars. *Rev. Mod. Phys.*, 74:1015–1071, 2002.
- [154] S. E. Woosley and R. D. Hoffman. *ApJ*, 395:202, 1992.
- [155] S. E. Woosley and T. A. Weaver. The physics of supernova explosions. *ARA&A*, 24:205–253, 1986.
- [156] S. E. Woosley and T. A. Weaver. Massive stars, supernovae, and nucleosynthesis. In S. A. Bludman, R. Mochkovitch, and J. Zinn-Justin, editors, *Supernovae*, pages 63–+, 1994.
- [157] S. E. Woosley and T. A. Weaver. The evolution and explosion of massive stars. ii. explosion hydrodynamics and nucleosynthesis. *ApJS*, 101:181, 1995.
- [158] S. E. Woosley, J. R. Wilson, G. J. Mathews, R. D. Hoffman, and B. S. Meyer. The r-process and neutrino-heated supernova ejecta. *ApJ*, 433:229–246, 1994.
- [159] T. N. Zinner and K. Langanke, 2004. private communication.



---

## Acknowledgments

I would like to thank everybody who contributed to this thesis.

- First of all I would like to thank my advisor Friedel Thielemann. Thanks to him I could carry out an interesting research project. His profound knowledge and his enthusiasm for physics were a constant motivation.
- I also would like to thank Karlheinz Langanke who agreed to be on my dissertation committee and who provided — together with his student Nikolaž Zinner — the cross sections for neutrino and antineutrino captures on nuclei.
- I am grateful to Matthias Liebendörfer who provided the explosion models and who was always available to discuss whatever questions I came up with. I also acknowledge a stay at CITA in 2004.
- I am indebted to Gabriel Martínez Pinedo. Without his great interest in my work and especially in the  $\nu p$ -process many things would not have been possible. I wish to thank him for great (extended) stays at IEEC in 2003 and 2005.
- Eduardo Bravo provided the explicit hydrodynamics code. I acknowledge his continuous support with the code.
- I am grateful to Stuart Whitehouse for his excellent maintenance of the computer cluster and for his support during the final phase of finishing this thesis.
- I acknowledge the kind and supportive atmosphere in the astrophysics group.
- I would like to thank my friends and fellow students Ute Dreyer and Sabine Maier for the many good discussions and the great fun we had together.
- The author acknowledges support from the Swiss National Science Foundation (SNF).
- I am indebted to my fellow players at the women's Unihockey Team of Basel Magic for their understanding and support which made it possible for me to pursue this thesis and at the same time be captain of this team during several seasons.
- Last, but not least, I wish to thank my family, and especially my parents, for their continuous support during my studies and especially during the final (hectic) phase of finishing this thesis and preparing the future.



---

## Curriculum Vitae

Name: Carla Fröhlich  
Adresse: Institut für Physik, Universität Basel  
Klingelbergstr. 82, CH-4056 Basel  
1989 – 1997 Gymnasium am Gymnasium Bäumilhof Basel  
1997 Matura Typus A  
1997 – 2003 Physikstudium an der Universität Basel (Schweiz) und  
Simon Fraser University (Kanada)  
2003 Diplom in theroetischer Physik  
Diplomarbeit bei Dr. T. Rauscher  
Titel: Global Alpha-Nucleus Potentials Close to the Coulomb Barrier  
2003 – 2007 Dissertation bei Prof. Dr. F.-K. Thielemann  
Titel: The Role of Neutrinos in Explosive Nucleosynthesis  
in Core Collapse Models with Neutrino Transport

### Ausbildung

Meine Ausbildung an der Universität Basel verdanke ich den folgenden Dozenten:  
M. Liebendörfer  
F.-K. Thielemann  
Dozenten des Internationalen Graduiertenkollegs Basel – Graz – Tübingen



---

## List of Publications

### Refereed Journals

F.-K. Thielemann, **C. Fröhlich**, et al.; *Production of Intermediate-Mass and Heavy Nuclei*. Progress in Part. and Nucl. Phys., in press.

**C. Fröhlich**, G. Martínez-Pinedo, M. Liebendörfer, F.-K. Thielemann, E. Bravo, W.R. Hix, K. Langanke, N.T. Zinner; *Neutrino-Induced Nucleosynthesis of  $A > 64$  Nuclei: The  $\nu p$ -process*. PRL 96, 142502 (2006).

**C. Fröhlich**, M. Liebendörfer, F.-K. Thielemann, K. Langanke, G. Martínez-Pinedo, N.T. Zinner, E. Bravo; *Explosive Nucleosynthesis in Supernovae*. Acta Physica Polonica B, in press.

**C. Fröhlich**, W.R. Hix, G. Martínez-Pinedo, M. Liebendörfer, F.-K. Thielemann; *Nucleosynthesis in Neutrino-Driven Supernovae*. New Astronomy Reviews 50, 496 (2006).

**C. Fröhlich**, P. Hauser, M. Liebendörfer, G. Martínez-Pinedo, F.-K. Thielemann, E. Bravo, N.T. Zinner, W.R. Hix, K. Langanke, A. Mezzacappa, K. Nomoto; *Composition of the Innermost Supernova Ejecta*. Ap.J. 637, 415 (2006).

**C. Fröhlich**, P. Hauser, M. Liebendörfer, G. Martínez-Pinedo, E. Bravo, N.T. Zinner, F.-K. Thielemann; *The Innermost Ejecta of Core Collapse Supernovae*. Nucl. Phys. A 758c, 27 (2005).

F.-K. Thielemann, D. Argast, F. Brachwitz, J.L. Fisker, **C. Fröhlich**, R. Hirschi, E. Kolbe, D. Mocerlj, T. Rauscher; *Nuclear Physics: A Key Ingredient in Astrophysical Modeling*. Nucl. Phys. A751 (2005) 301c.

P. E. Koehler, Yu. M. Gledenov, T. Rauscher, **C. Fröhlich**; *Resonance Analysis of  $^{147}\text{Sm}(n, \alpha)$  cross sections: Comparison to optical model calculations and indications of non-statistical effects*. Phys. Rev. C69 (2004) 015803.

### Conference Proceedings

**C. Fröhlich**, R. Hirschi, M. Liebendörfer, F.-K. Thielemann, G. Martínez-Pinedo, E. Bravo; *Core Collapse Supernovae: The Explosion Mechanism And Primary and Secondary Nucleosynthesis Processes*. in "The Metal Rich Universe", eds. G. Israelian & G. Meynet (Cambridge University Press 2006), in press.

**C. Fröhlich**, M. Liebendörfer, F.-K. Thielemann, G. Martínez-Pinedo, K. Langanke, N.T. Zinner, W.R. Hix, E. Bravo; *The Role of Neutrinos in Explosive Nucleosynthesis*. in "Proceedings of Nuclei in the Cosmos NIC-IX", eds. A. Mengoni *et al.* (SISSA Proceedings of Science 2006), in press.

G. Martínez-Pinedo, A. Kelic, K. Langanke, K.-H. Schmidt, D. Mocerlj, **C. Fröhlich**, F.-K. Thielemann,

I. Panov, T. Rauscher, M. Liebendörfer, N.T. Zinner, B. Pfeiffer, R. Buras, H.-T. Janka; *Nucleosynthesis in neutrino heated matter: The  $\nu p$ -process and the  $r$ -process*. in "Proceedings of Nuclei in the Cosmos NIC-IX", eds. A. Mengoni *et al.* (SISSA Proceedings of Science 2006), in press.

**C. Fröhlich**, M. Liebendörfer, G. Martínez-Pinedo, F.-K. Thielemann, E. Bravo, N.T. Zinner, W.R. Hix, K. Langanke, A. Mezzacappa, K. Nomoto; *Composition of the Innermost Core Collapse Supernova Ejecta and the  $\nu p$ -Process*. in "Origin of Matter and Evolution of Galaxies: New Horizon of Nuclear Astrophysics and Cosmology (International Symposium 2005)" eds. S. Kubono, W. Aoki, T. Kajino, T. Motobayashi & K. Nomoto (AIP Conference Proceedings 2006, Vol. 847), p. 333.

W.R. Hix, **C. Fröhlich**, G. Martínez-Pinedo, M. Liebendörfer and F.-K. Thielemann; *Influence of the Explosion Mechanism on the Ejecta of Core Collapse Supernovae*. *Meteoritics & Planetary Science* 40, 5340 (2005).

R. Hirschi, **C. Fröhlich**, M. Liebendörfer and F.-K. Thielemann; *Stellar Evolution of Massive Stars at Very Low Metallicity*. in "The Many Facets of the Universe — Revelations by New Instruments" (Reviews of Modern Astronomy Vol. 19, Wiley Verlag 2006), p. 101.

**C. Fröhlich**, F.-K. Thielemann, G. Martínez-Pinedo, M. Liebendörfer; *The Influence of the Explosion Mechanism on the Fe-Group Ejecta of Core Collapse Supernovae*. in "From Lithium to Uranium", eds. V. Hill, P. Francois, and F. Primas (Cambridge University Press 2005), p. 309.

W. R. Hix, S. Parete-Koon, **C. Fröhlich**, F.-K. Thielemann, G. Martínez-Pinedo; *The Challenges of Coupling Supernova Nucleosynthesis to the Central Engine*. in "Open Issues in Core Collapse Supernova Theory" eds. A. Mezzacappa and G. M. Fuller (Proceedings from the Institute for Nuclear Theory Vol. 14, World Scientific 2005), p. 369.

**C. Fröhlich**, P. Hauser, F.-K. Thielemann, M. Liebendörfer, G. Martínez-Pinedo; *The Innermost Zones of Core Collapse Supernovae*. in "1604 – 2004: Supernovae as Cosmological Lighthouses", eds. M. Turatto, W.R.J. Shea, S. Benetti, and L. Zampieri (ASP Conference Series 2005, Vol. 342), p. 199.

T. Rauscher, **C. Fröhlich**, K. H. Guber; *Reaction Rates and Nuclear Properties Relevant for Nucleosynthesis in Massive Stars and Far from Stability*. in "Capture Gamma Ray Spectroscopy and Related Topics" (World Scientific, Singapore 2003), p. 336.